Berkeley Seismological Laboratory

Bay Area Seismicity 01/01/2000 - 07/20/2007

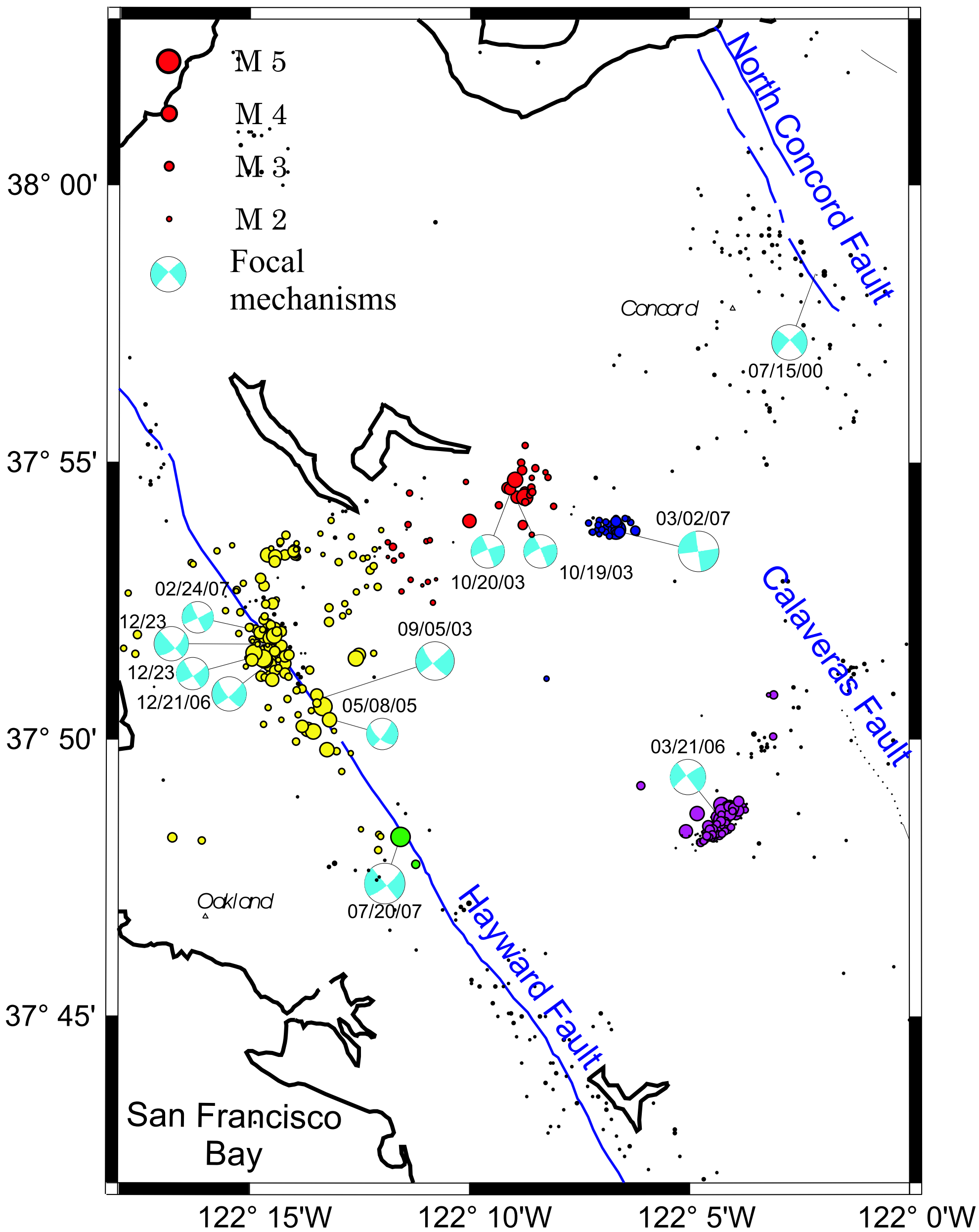

Annual Report
July 2006 - June 2007

Berkeley Seismological Laboratory

Annual Report

July 2006 - June 2007

Cover Picture

Earthquakes along and near the Hayward Fault from 2000 to the present. The July 20, 2007 event is indicated in green, and black dots indicate background seismicity. Other recent clusters along and near the Hayward Fault are marked in color, with the earthquakes from December 2006 in yellow. The Lafayette event, which occurred on the evening of March 1, 2007, and its aftershocks are denoted in dark blue. The earthquake on the morning of July 20, 2007 occurred farther southeast along the Hayward Fault than the events in the sequence which occurred around Christmas, 2006. It was felt widely throughout the Bay Area and jolted many residents awake. Its mechanism is typical for strike-slip along the Hayward Fault. Although there have been many small events along the Hayward Fault over the past few years, in 1868 the Hayward Fault hosted the first good-sized earthquake to occur in the Bay Area in a relatively heavily populated area.

Contents

Chapter 1

Director's Report

As I was working on the introduction to this Annual Report, in the evening of October 30th, 2007, the San Francisco Bay Area - including my desk at home - was shaken by the strongest temblor since the M 6.9 1989 Loma Prieta earthquake. It felt exactly as John Mitchell described in his impressions from the great Lisbon earthquake of 1755: "a tremulous vibration followed by a wave-like undulation", but was generally a mild experience. Promptly, our real-time earthquake notification system indicated that it had occurred east of Alum Rock in the South Bay, and that its moment magnitude was M_w 5.4. The shaking was felt widely, from Carson City in Nevada and Yosemite in the East, to Thousand Oaks near Los Angeles in the South and to Eureka in the North. Fortunately, nobody was hurt in this quake and the damage was very minor, surprisingly so. Owing to our real time estimation of rupture directivity, it quickly became apparent that the rupture propagated to the south-west, concentrating the strongest shaking in a sparsely populated area. This was in contrast to what was experienced last July, when an earthquake smaller by an order of magnitude, the M_w 4.2, July 20th, 2007 Oakland earthquake, sent objects flying off shelves in Berkeley and San Francisco. The latter earthquake occurred in the heart of the urban area, and the rupture propagated to the north. These recent examples illustrate the complexity of earthquake ruptures, and how important it is to provide rapid and accurate information not only on the hypocentral location and the magnitude, but also on rupture directivity, which can significantly influence the distribution of the shaking. The near surface three-dimensional geometry of basins and the basement topography also play a role in amplifying or reducing local shaking, and the larger the earthquake, the more important this becomes. The ability to provide this kind of information in quasi-real time is the result of efforts that have been pursued at BSL for the last 15 years, progressively translating research developments into the operational environment. The Alum Rock earthquake was a perfect "dry run" test for our northern California real time system, operated jointly with the US Geological Survey at Menlo Park, and helped identify a few small issues with telemetry and hard-wired parameters in a real life, yet benign situation.

This earthquake also served to assess the performance of the Earthquake Early Warning system currently being developed (see section 2.17.), which successfully detected the earthquake and determined its magnitude to within 0.3 magnitude units.

During the night and days following the earthquake, members of our staff also spent considerable time providing information to the media - another regular activity which sets the BSL apart from most other Organized Research Units on the Berkeley Campus.

1.1. Background and Facilities

The Berkeley Seismological Laboratory (BSL), formerly the Berkeley Seismographic Station (BSS), is the oldest Organized Research Unit (ORU) on the UC Berkeley campus. Its mission is unique in that, in addition to research and education in seismology and earthquake-related science, it is responsible for providing timely information on earthquakes (particularly those that occur in northern and central California) to the UC Berkeley constituency, the general public, and various local and state government and private organizations. The BSL is therefore both a research center and a facility/data resource, which sets it apart from most other ORUs. A major component of our activities is focused on developing and maintaining several regional observational networks, and participating, along with other agencies, in various aspects of the collection, analysis, archival, and distribution of data pertaining to earthquakes, while maintaining a vigorous research program on earthquake processes and Earth structure. In addition, the BSL staff spends considerable time on public relations activities, including tours, talks to public groups, responding to public inquiries about earthquakes, and, more recently, World-Wide-Web presence (`http://seismo.berkeley.edu/`).

UC Berkeley installed the first seismograph in the Western Hemisphere at Mount Hamilton (MHC) in 1887. Since then, it has played a leading role in the operation of state-of-the-art seismic instruments and in the development of advanced methods for seismic data analysis and interpretation. Notably, the installation, starting in 1927, of Wood-Anderson seismographs at 4 locations in northern California (BKS, ARC, MIN and MHC) allowed the accurate determination of local earthquake magnitude (M_L) from which a unique historical catalog of regional earthquakes has been maintained to this day, providing crucial input to earthquake probabilities studies.

Over the years, the BSS continued to keep apace of technological improvements. The first centrally telemetered network using phone lines in an active seismic region was installed by BSS in 1960. The BSS was the first institution in California to operate a 3-component "broadband" system (1963). Notably, the BSS played a major role in the early characterization of earthquake sources using "moment tensors" and source-time functions, and made important contributions to the early definitions of detection/discrimination of underground nuclear tests and to earthquake hazards work, jointly with UCB Engineering. Starting in 1986, the BSS acquired 4 state-of-the-art broadband instruments (STS-1), while simultaneously developing PC-based digital telemetry, albeit with limited resources. As the telecommunication and computer technology made rapid progress, in parallel with broadband instrument development, paper record reading could be completely abandoned in favor of largely automated digital data analysis.

The current modern facilities of BSL have been progressively built over the last 16 years, initiated by significant "upgrade" funding from UC Berkeley in 1991-1995. The BSL currently operates and acquires data, continuously and in real-time, from over 60 regional observatories, housing a combination of broadband and strong motion seismic instrumentation installed in vaults, borehole seismic instrumentation, permanent GPS stations of the Bay Area Regional Deformation (BARD) network, and electromagnetic sensors. The seismic data are fed into the BSL real-time processing and analysis system and are used in conjunction with data from the USGS NCSN network in the joint earthquake notification program for northern California, started in 1996. This program capitalizes on the complementary capabilities of the networks operated by each institution to provide rapid and reliable information on the location, size and other relevant source parameters of regional earthquakes. In recent years, a major emphasis in BSL instrumentation has been in densifying the state-of-the-art seismic and geodetic networks, while a major ongoing emphasis in research has been the development of robust methods for quasi-real time automatic determination of earthquake source parameters and predicted strong ground motion, using a sparse network combining broadband and strong motion seismic sensors, as well as permanent geodetic GPS receivers. A recent emphasis has been the development of "earthquake early warning" capabilities.

The backbone of the BSL operations is a regional network of now close to 30 digital broadband and strong motion seismic stations, the Berkeley Digital Seismic Network (BDSN), with continuous telemetry to UC Berkeley. This network provides the basic regional data for the real-time estimation of location, size and rupture parameters for earthquakes of M 3 and larger in central and northern California, within our Rapid Earthquake Data Integration (REDI) program and is the Berkeley contribution to the California Integrated Seismic Network (CISN). It also provides a fundamental database for the investigation of three-dimensional crustal structure and its effects on regional seismic wave propagation, which is ultimately crucial for estimating ground shaking for future earthquakes. Most stations also record auxiliary temperature/pressure channels, valuable in particular for background noise quality control. Complementing this network is a ~ 25 station "high-resolution" network of borehole seismic sensors located along the Hayward Fault (HFN) and under the Bay Area bridges, operated jointly with the USGS/Menlo Park and linked to the Bridge Safety Project of the California Department of Transportation (Caltrans). The latter has facilitated the installation of sensor packages at 15 bedrock boreholes along 5 east bay bridges in collaboration with Lawrence Livermore National Laboratory (LLNL). A major science goal of this network is to collect high signal-to-noise data for micro-earthquakes along the Hayward Fault to gain insight into the physics that govern fault rupture and its nucleation. The BSL is also involved in the operation and maintenance of the 13 element Parkfield borehole seismic array (HRSN), which is providing high quality data on micro-earthquakes, clusters and most recently tremors, and provides an important reference for the San Andreas Fault Observatory at Depth (SAFOD). Since April 2002, the BSL is also involved in the operation of a permanent broadband ocean bottom station, MOBB, in collaboration with MBARI (Monterey Bay Aquarium Research Institute).

In addition to the seismic networks, the BSL is involved in data archival and distribution for the permanent geodetic BARD Network as well as the operation, maintenance, and data processing of 22 out of its 70+ sites. Whenever possible, BARD sites are collocated with BDSN sites in order to minimize telemetry costs. In particular, the development of analysis methods combining the seismic and geodetic data for the rapid estimation of source parameters of significant earthquakes has been one focus of BSL research.

Finally, two of the BDSN stations (PKD, SAO) also share data acquisition and telemetry with 5-component electromagnetic sensors installed with the goal of investigating the possibility of detection of tectonic signals. In 2002-2003, automated quality control software was implemented to monitor the electromagnetic data.

Archival and distribution of data from these and other regional networks is performed at the Northern California Earthquake Data Center (NCEDC), operated at the BSL in collaboration with USGS/Menlo Park. The data reside on a mass-storage device (current holdings ~ 10 TerraBytes), and are accessible "on-line" over the Internet (`http://www.ncedc.org`). Among others, data from the USGS Northern California Seismic Network (NCSN), are archived and distributed through the NCEDC. The NCEDC also maintains, archives and distributes the ANSS/CNSS earthquake catalog.

Core University funding to our ORU currently provides salary support for 2 field engineers, one computer expert, 2 data analysts, 1 staff scientist and 2 administrative staff. This supports a diminishing portion of the operations of the BDSN and provides seed funding for our other activities. All other infrastructure programs are supported through extra-mural grants primarily from the USGS, NSF, and the State of California, through its Office of Emergency Services (OES). We acknowledge valuable recent contributions from other sources such as Caltrans and PEER, as well as our Earthquake Research Affiliates.

1.2. Highlights of 2006-2007

1.2.1 Research Accomplishments

Chapter 2 documents the main research contributions of the past year. Research at the BSL spans a broad range of topics, from the study of microseismicity at the local scale to global deep earth structure, and includes the use of seismological, geodetic, and remote sensing (InSAR) techniques. Productivity continues to be high: forty three papers in refereed journals, including two in Nature, have been published by BSL researchers in the last year, originating from 4 faculty members and their students, and one senior researcher.

The analysis of borehole microseismic data from the HRSN (Parkfield) network is continuing to provide exciting results. A highlight of this past year's research has been a study by Doug Dreger and collaborators (2.1.), in which they have reconciled the difference in reported stress drop estimates for small earthquakes, by applying Doug's finite source inversion method to microseism borehole observations. Bob Nadeau and collaborators (2.3., 2.6.) continue to analyze repeating earthquakes and tremor activity near Parkfield, finding intriguing patterns of changes in strain release associated with the M6 2004 Parkfield earthquake, and in particular a correlation between deep tremor activity and microseismicity in seismogenic zone above. On the other hand, Karl Kappler and collaborators (2.18.) show no clear precursory signal in electromagnetic data preceding or during the Parkfield earthquake.

Work on non-volcanic tremor in subduction zones has led Richard Allen to propose a relationship betweeen the recurrence period of these tremors and properties of the overriding plate, in particular topography (2.4.).

Richard Allen and his students have also continued to develop a methodology for earthquake early warning (2.17.), testing it in the framework of our real-time system. While the debate continues as to whether an earthquake knows when it starts how big it will become, an important by-product of this development is the ability to significantly speed-up the production of reliable "shake maps".

Doug Dreger and his students and collaborators have also worked on a variety of regional source and structure topics. In particular, they have finalized a methodology using moment tensor inversion to characterize different seismic sources, and in particular distinguish those with a significant non-double couple component, such as would be the case for nuclear tests and mine collapses (2.12.). In particular, this methodology has proven very useful in assessing the nature of the Utah mine collapse of Aug 6, 2007 (e.g. `http://www.seismo.berkeley.edu/~peggy/Utah20070806.htm`). Concurrently, they have been testing crustal and basin models in the San Francisco Bay Area, and in particular the Santa Clara valley, using different approaches: microseismic noise (2.8.), 3D broadband waveform modeling using finite differences (2.9.), and inversion of teleseismic observations (2.10.). Finally, various approaches to determining the Lg attenuation structure in the San Francisco Bay Area have been compared, towards the determination of a robust model for this region (2.7.).

A number of studies focus on the seismicity and deformation in northern California. Peggy Hellweg 2.14. describes the unusual microearthquake sequence of October 2003 near Orinda, CA, while a recently begun study aims at characterizing moment tensors and spectra of slow events in the Mendocino region (2.16.). Using InSar data, Roland Bürgmann and his group have been characterizing creep along the Rodgers Creek Fault (2.19.) and the San Andreas Fault (2.21.). Earthquake and ground shaking potential has been analyzed in different fashions. Using continuous GPS data accumulated over the last 10-15 years on the BARD network, Nicolas Houlié and I (2.20.) point out to the consequences of asymmetric rheology across the Bay Area faults. The performance capabilities of the northern California seismic networks have been assessed through simulations of a repeat of the 1906 earthquake (2.15.). A recently begun study is searching for evidence of accelerating seismic moment release in northern and southern California by modelling the evolution of stress and seismicity in the region (2.2.). A new method based on coda spectral amplitude ratios shows promise in distinguishing earthquake sources, with consequences on earthquake scaling (2.5.). Finally, magnitude accuracy within CISN will soon be improved with the implementation of a California-wide consistent set of local magnitude (M_L) station corrections (2.13.).

Moving away from California, continuous and campaign style GPS data have been used to constrain the motion and deformation of the Indian Plate (2.22.), while Nicolas Houlié and Jean-Paul Montagner (IPG paris, France) 2.23. propose a method to track the long term deformation response of a volcano to changes in pressure inside the magma chamber.

BSL researchers have also contributed to larger scale regional and global structure studies. Mei Xue and Richard Allen 2.24. used teleseismic body wave travel time tomography to investigate the fate of the subducted Juan de Fuca plate and its interaction with the Yellowstone plume head. Barbara Romanowicz and her group have been investigating new approaches to waveform tomography. With post-doc Aimin Cao, we have been testing a promising method combining the advantages of the path average approximation and those of 3D Born scattering on the case of radially anisotropic upper mantle structure in southeast Asia (2.25.). We are making progress towards a global upper mantle model using the spectral element method in the forward computation of 3D synthetics (2.28.). We have further documented the presence of strong lateral variations at the base of the mantle using diffracted waves (2.29.). Using an array stacking method, Aimin Cao has been able to localize scatterers most likely associated with remnant slabs in the lowermost mantle under North America (2.30.). With post-doc Fabio Cammarano, we have been working towards understanding the respective contributions of variations in temperature and composition in the upper mantle using seismic waveforms and mineral physics data as constraints (2.27., 2.26.). Finally, we continue to study the earth's inner core, and, this year, have assembled a high quality dataset of near antipodal PKP travel time data to test for the existence of an innermost inner core (2.31.).

1.2.2 Infrastructure and Earthquake Notification

A highlight of the past year has been the successful completion of the NSF funded project in collaboration with Tom VanZandt of Metrozet for the design and testing of new electronics for the STS-1 very broadband seismometer. This exceptional seismometer, installed at several hundred seismic stations around the world, and in particular at 10 of the BDSN sites, was developed in the 1970's but is no longer produced, raising concerns about its longevity and the need for a high quality replacement. The BSL developed a test-best and participated in the testing of successive iterations of electronics developed by Metrozet. The new electronics present several attractive features, in particular capabilities for remote calibration. After testing at UC Berkeley's Byerly vault, they were installed for further testing at Hopland (HOPS). They are now ready for production.

The prototype earthquake early warning system developed by Prof. Richard Allen has been implemented in our real time system and is being tested and improved in this framework. It is already providing useful by-products, such as the ability to obtain reliable shake maps in just over a minute, compared to 4+ minutes in the operational system used by CISN.

As in previous years, BSL's infrastructure development efforts have centered around several major projects:

- operation and enhancement of the joint earthquake notification system with USGS/Menlo Park.
- the continuing development of the California Integrated Seismic Network
- participation, at various levels, in three components of the national Earthscope program: the deployment in northern California of the *BigFoot* component of USArray, archival of borehole strainmeter data in the framework of the Plate Boundary Observatory (PBO), and the preparation for archival of the data from the San Andreas Fault Observatory at Depth (SAFOD).
- development of borehole networks at Parkfield and along the Hayward Fault
- operation and further enhancements of the BARD network of continuous GPS
- operation of the Northern California Earthquake Data Center

The main goal of the CISN (see Section 3.2.) is to ensure a more uniform system for earthquake monitoring and reporting in California. The highest priority, from the point of view of emergency responders in California, is to improve the robustness of statewide real-time notification and to achieve a uniform interface across the State to the California OES and other emergency responders. This represents a major challenge, as the CISN started as a heterogeneous collection of networks with disparate instrumentation, software systems and cultures. Much effort has gone over the past few years to develop coordinated software between southern and northern California and in northern California, between Berkeley and USGS/Menlo Park. These two institutions are joined together in the Northern California Earthquake Management Center(NCEMC). A highlight of the past year has been the long awaited retirement of the CUSP real-time earthquake timing system in Menlo Park. BSL staff continue to spend considerable efforts in organizational activities for CISN, notably by participating in the CISN Project Management Group (Neuhauser and Hellweg), which includes weekly 2 hour phone conferences, and the

Standards Committee (Neuhauser-chair, Hellweg, Lombard), which strives to define and coordinate software development tasks. Romanowicz and Hellweg serve on the CISN Steering Committee. Doug Neuhauser has also been serving on the CISN Steering Committee in the transition period following Lind Gee's departure in summer 2005. The CISN also represents California as a designated region of ANSS (Advanced National Seismic System) and the BSL is actively involved in planning activities for the ANSS.

The BSL concluded an agreement in June 2004 with IRIS to contribute 19 stations of the BDSN to USArray, while the experiment is deployed in California. This includes 17 existing stations and the two recently installed sites: GASB and MCCM. In the past year, BSL has continued to acquire telemetered data from these and other northern California USArray stations and to pay particular attention to the maintenance of those permanent sites which are part of USArray. As USArray moves out of California starting in Fall 2007, BSL has been preparing to take over 7 of the USArray sites. This involves transfer of site permits, preparation of BSL equipment (seismometers and dataloggers funded through FEMA and OSN grants) and securing new telemetry paths where needed.

The Parkfield borehole network (HRSN, see Section 3.4.) continues to play a key role in support of the Earthscope SAFOD (San Andreas Fault Observatory at Depth) drilling project, by providing low noise waveforms for events in the vicinity of the target drilling zone. In the past year, integration of the HRSN data streams into the NCSN triggering scheme has been completed, in support of researchers working on repeating micro-earthquakes. Also, the upgrade of the telemetry system has been completed. HRSN data are now telemetered over the USGS T1 line to Menlo Park and then on to Berkeley over the joint T1 line between the two institutions.

In the past year, the Northern Hayward Fault Network (NHFN, see Section 3.3.) has continued to expand. St. Mary's College station (SM2B) has been completed and four additional sites have been drilled, have downhole packages, and are awaiting connection to dataloggers. This will bring the total number of borehole NHFN sites to 18. On-going network maintenance involves regular inspection of the collected seismic waveform data and spectra for nearby seismic events, and for noise samples, in order to assure that the instruments operate at maximum performance to capture the source spectrum of micro-earthquakes down to negative magnitudes.

The BARD continuous GPS (C-GPS) network (see Section 3.5.) has focused its efforts to convert three additional sites to acquire data at 1Hz sampling rate (up from the standard 15-30 sec rate), bringing to 15 the total number of stations upgraded, with the goal of using these data in complement to seismic data for real-time earthquake notification. We have been working with our colleagues at the US Geological Survey in Menlo Park to establish a joint GPS real time data acquisition system and integrate it with our existing seismic earthquake notification system. We have been working with EB Parks, EBMUD and the Plate Boundary Observatory (PBO) of Earthscope, to acquire data from their GPS stations in real time. In exchange for real time data feeds from East Bay agencies, we can provide RTK (Real-Time Kinematic) data for land surveys that they perform.

The NCEDC (see Section 3.6.) continues archival and on-line distribution of data from expanding BDSN, NHFN, HRSN, BARD, Mini-PBO, and other networks and data collections in northern California and Nevada, including telemetered continuous data from USArray stations in northern California and vicinity. We are continuing to receive data from the SAFOD pilot hole and main hole and data from 15 SCSN (southern California) broadband sites as part of the CISN robust "backbone". In late 2006, we begun to archive and distribute a single unified northern California earthquake catalog, obtained in real-time from the NCEMC through database replication from the NCEMC's real-time systems. In the past year, the NCEDC has supported the NCEMC earthquake analysis by providing real-time access to earthquake parameters and waveforms for the CISN Jiggle earthquake review software, and has implemented software and procedures to read and archive continuous NCSN seismograms from tapes for the period 2001-2005, beginning the processing of these tapes.

1.3. BSL staff news

Changes in BSL staff in 2006-07 are as follows.

Cynthia Bresloff left BSL in June 2007 to pursue a career in GIS support at the Nature Conservancy and was replaced in August 2007 by Jennifer Taggart, who received her BS in geophysics from California Institute of Technology.

Kate Conner went on maternity leave in May 2007 and gave birth to baby boy Elliott Koenig Lewis on May 24, 2007. Eileen Evans worked as a student employee in the business office while Kate was on maternity leave.

Two graduate students associated with BSL completed their PhD's in the past year: Dennise Templeton and Akiko To. Akiko is now a post-doc at JAMSTEC and Dennise accepted a position at Lawrence Livermore National Lab. Junkee Rhie, who graduated in 2005 and stayed on as a post-doc for a year, joined the faculty of the University of Seoul, Korea, in July 2007. Postdoc Gareth Funning joined the faculty at the University of California, Riverside. Federica Marone completed her posdoc appointment at the end of November 06 and joined the research staff at the Paul Scherrer Institute (Switzerland). Chris Fuller worked as a postdoc with

Roland Büurgmann between July and December 06.

New arrivals have continued through the summer and early Fall of 2007. Huaiyu Yuan joined the global seismology group as a post-doc in early August. Chander Shaker Daula Vishwanath arrived in late June on a one year BOYSCAST postdoctoral fellowship. Isabelle Ryder was hired in January as a postdoc working in Roland Burgmann's group. New graduate students Shan Dou, Robert Porritt, Holly Brown Moore, and Amanda Thomas arrived in the summer of 2007. Angela Chung received her BS from EPS and is now working for the Lab as a Staff Research Associate.

Rich Clymer retired at the end of June and has come back to work part time as a retiree appointee to work on the HRSN maintenance and upgrade.

Student employee Tomasz Matlak graduated and left the BSL engineering lab to pursue his PhD in the Department of Mechanical Engineering. His brother Jozef is a freshman this year and has replaced his brother in the lab. Student employee Eric Winchell began working with the global seismology group in November 2006.

1.4. Acknowledgements

I wish to thank our technical and administrative staff, scientists and students for their efforts throughout the year and their contributions to this Annual Report. Individual contributions to activities and report preparation are mentioned in the corresponding sections, except for the Appendix section, prepared by Kate Conner, Kristen Jensen and Jennifer Taggart.

I also wish to specially thank the individuals who have regularly contributed to the smooth operation of the BSL facilities: Mario Aranha, Rich Clymer, Doug Dreger, John Friday, Jarrett Gardner, Peggy Hellweg, Nicolas Houlié, Bill Karavas, Alexei Kireev, Rick Lellinger, Pete Lombard, Rick McKenzie, Bob Nadeau, Doug Neuhauser, Charley Paffenbarger, Bob Uhrhammer, and Stephane Zuzlewski, and in the administrative office, Kristen Jensen, Kate Conner, Tina Barber-Riggins and Yolanda Andrade. I also wish to thank our undergraduate assistants, Angela Morrish Chung, Eileen Evans, Tomasz Matlak, Jozef Matlak, and Eric Winchell for their contributions to our research and operational activities.

I am particularly thankful to Jennifer Taggart and Peggy Hellweg, for their help in putting together this Annual Report.

The Annual Report of the Berkeley Seismological Laboratory is available on the WWW at `http://seismo.berkeley.edu/annual_report`.

Chapter 2

Research Studies

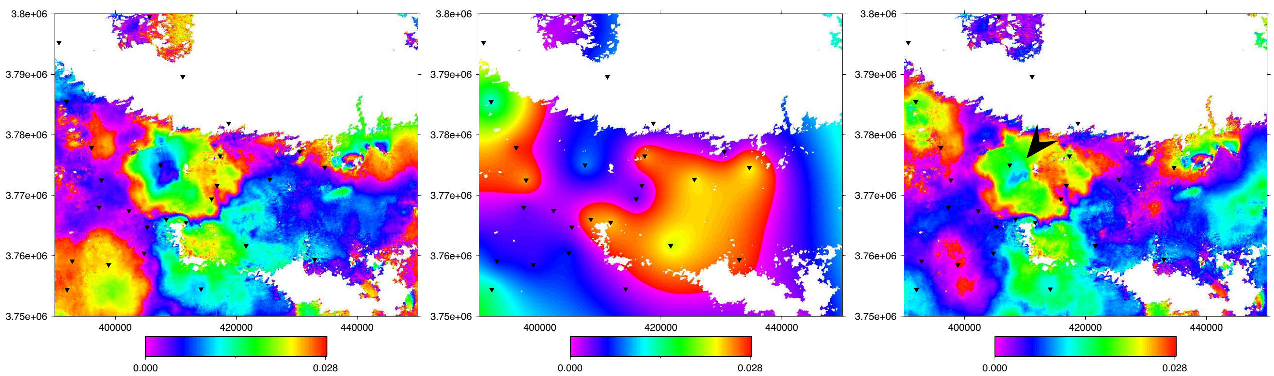

Figure 2.1: InSAR measurement (left), troposphere model inferred from GPS observations (center) and corrected InSAR scene (right). Thirty percent of the uplift detected (20 mm) in the San Gabriel Valley was constituted by a troposphere contribution located above the maximal uplift location. The methology applied here has been automated on the BARD network. From *Houlié, Funning and Burgmann, in prep.*

2.1. Kinematic Models of Repeating Earthquakes

Douglas Dreger, Robert Nadeau, and Angela Chung

2.1.1 Introduction

On the Parkfield segment of the San Andreas Fault, repeating earthquake seismicity is observed with highly similar waveforms, suggesting that the events occur on the same patch of fault repeatedly (*Nadeau et al.*, 1995). Surrounding these repeating clusters are areas inferred to creep. A shallow cluster of such repeating events is the drilling target of the NSF EarthScope San Andreas Fault Observatory at Depth (SAFOD) experiment. *Imanishi et al.* (2004) studied waveforms and spectra for one of the SAFOD target events using data obtained from the SAFOD Pilot Hole, and determined a Mw 2.1 and a depth of 2.1 km. From their corner frequency measurements they find a static stress drop of 8.9MPa. On the other hand, *Nadeau and Johnson* (1998) proposed an asperity-loading model to infer that slip in each event was on the order of 6.6cm, and a stress drop of 240MPa. If a rigidity of 12 GPa, more appropriate for the shallow depth of the event is used, a stress drop of 100MPa is obtained with their method. The difference between 8.9 and 100 MPa bears directly on the nature of the faulting mechanics, whether frictional sliding or rock fracture processes are operating in these events. In this study we reconcile the difference in the reported stress drop estimates using a finite-source inverse method to determine the rupture area, slip distribution, spatially variable stress drop, and rupture velocity of the small repeating earthquakes.

2.1.2 Data and Methods

We use three-component 100Hz velocity records from the High Resolution borehole Seismic Network (HRSN) to determine the seismic moment rate functions at each station for a Mw2.1 event in the repeating cluster being targeted by the NSF SAFOD experiment. Figure 2.2 shows the location of the target events with respect to the HRSN, and Figure 2.2b shows the relative locations of the Mw2.1 repeating earthquakes, and a nearby Mw0.68 event used as an empirical Green's function (eGf). The relative event locations are based on sub-sample precision waveform cross-correlation measurements and the double-difference relocation method, giving centroid locations within about 2m of each other. The smaller eGf is located about 10m away and is even within the very small radius inferred for a stress drop of 240MPa after *Nadeau and Johnson* (2004).

In Figure 2.3, the vertical component waveforms at station VCAB are compared for the Mw2.1 target and the Mw0.68 eGf, illustrating an extremely high degree of waveform similarity. This level of waveform similarity is observed for all three components at all stations, and attests to the nearly collocated nature of the events as well as the similarity in their respective focal mechanisms. Together with the exceptional SNR, these events represent an ideal case for the empirical Green's function method.

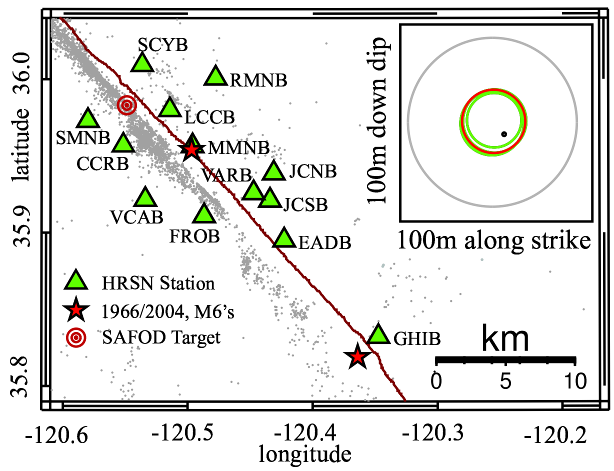

Figure 2.2: Map showing the locations of HRSN stations (inverted triangles), the SAFOD repeating target events (concentric circles), the locations of the 1966 and 2006 mainshock epicentres (stars), and background seismicity (gray dots). The inset shows a cross-sectional view of the relative locations of the repeating events (larger circles), and the Mw0.68 empirical Green's function event (small circle). The size of the circles shows the respective areas of a 240MPa event. For comparison the large gray circle shows the inferred area for a 9MPa event.

To obtain the seismic moment rate functions at each station we employed a commonly used spectral domain deconvolution approach in which the complex spectrum of the eGf is divided out of the complex spectrum of the main event. *Hough and Dreger* (1994) and references therein give an overview of the method. The basic concept is that if the smaller eGf event is collocated and has the same radiation pattern as the larger event, then the common instrument response, propagation, attenuation and site effects are removed by the deconvolution process, resulting in the unfettered source spectrum. The inverse Fourier transform yields the pulse-like seismic moment rate function (Figure 2.3).

We performed deconvolutions separately on each of the three components at 8 or 9 of the HRSN stations depending on availability and SNR. Stations EADB and GHIB

(Figure 2.2) were omitted in all cases due to noisy channels. The remaining stations provide excellent azimuthal coverage of the repeating sequence (Figure 2.2). The moment rate functions may then be inverted for the spatial distribution of fault slip (*Dreger*, 1994).

In our application we used a 31 by 31 fault with dimensions of 150 x 150 m^2, with a corresponding subfault size of 4.8 x 4.8 m^2. The fault is assumed to have a strike of 137 and dip of 90. The size of the subfault was chosen to produce a temporally smooth kinematic process with respect to the sample rate of the data. A slip positivity constraint, and a smoothing operator minimizing the spatial derivative of slip were applied. The weight of the smoothing constraint was determined by trial and error by finding the smallest value that produced a smoothed model with close to the maximum fit to the data measured by the variance reduction.

In each inversion it is assumed that the rupture velocity is constant, and that the boxcar slip velocity function has a constant rise time. Using a grid search we tested rupture velocities of 0.2 to 2.3 km/s (8-100%), and rise times from 0.004 to 0.052 sec to find optimal values and to assess the resolution of the parameters.

Results

In Figure 2.4 we show the slip model. This model has a rise time of 0.008 seconds, and a rupture velocity of 1.8 km/s (78% of the local shear wave velocity), the median from models within 2% of the peak fit. The allowable range in the kinematic parameters given this level of fit is 1.2-2.3 km/s (52-100% of the shear wave velocity) in rupture velocity, and 0.004 to 0.012 seconds for rise time. Within this population of solutions there is a tradeoff in the rise time and rupture velocity where long rise times are associated with fast rupture velocities (or short rupture times), and vice versa. It is notable that the obtained rise time is more consistent with a slip pulse rather than crack-like rupture, and the slip velocity inferred from the ratio of slip to rise time is 167 cm/s, consistent with values obtained for larger events. There is a dominant asperity in which the slip is found to be extremely concentrated, roughly circular with a diameter of about 40 m with a peak (8.6 cm) at the center, which is similar to the 6.6 cm inferred by *Nadeau and Johnson* (1998).

Because the slip distribution is non-uniform, we use the method of *Ripperger and Mai* (2004), shown to be consistent with static or dynamic elastic dislocation models, to determine the coseismic stress change (stress drop). This method maps the spatially variable slip on the fault to the spatially variable stress change, or stress drop. Results applied to the SAFOD target event are shown in Figure 2.4B. In regions of high slip, the stress change is positive indicating a stress drop during rupture. The method also determines the degree of stress increase (negative stress change) on the region surrounding the rupture. The model has a peak stress drop of 80 MPa, and averages ranging from 3.7-19.7MPa depending on how the average is calculated.

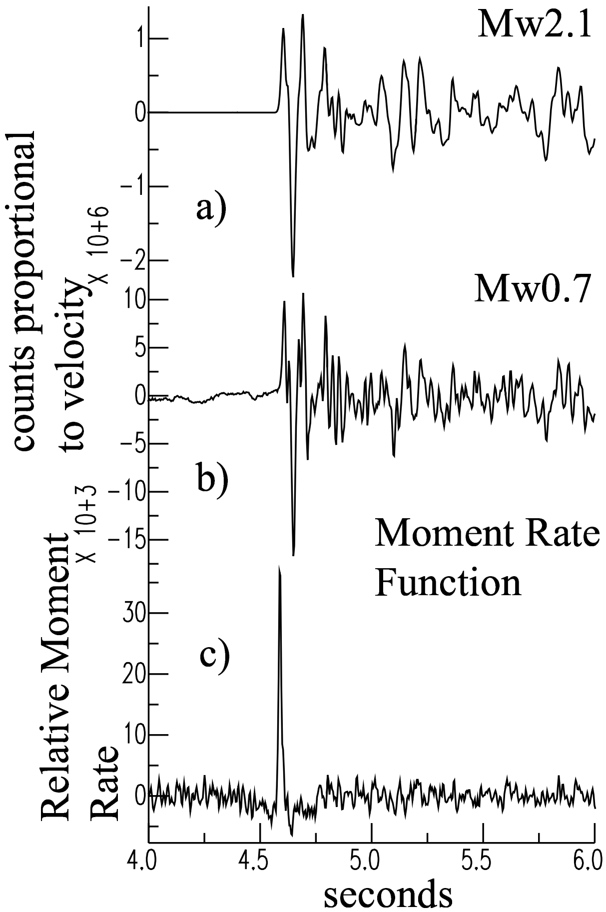

Figure 2.3: a) Vertical component waveform for the Mw2.1 event recorded at station VCAB. b) Vertical component waveform for the Mw0.68 eGf event recorded at station VCAB. c) The moment rate function obtained by deconvolving (b) from (a).

The very high stress drop we obtain for much of the rupture area of the SAFOD repeaters (Figure 2.4B) is at odds with more traditional spectrally-based estimates (*e.g. Imanishi et al.*, 2004). However, the stress drop averaged from Figure 2.4B over areas with positive stress drop is only 11.6 MPa, which is close to the *Imanishi et al.* (2004) result. On the other hand, the spatially variable high stress drop we obtain is required to fit the shape of the moment rate functions, and the peak is closer to the estimate obtained using the method of *Nadeau and Johnson* (1998). Thus, the finite-source results reconcile these disparate estimates of stress drop, illustrating that the two methods are apparently sensitive to different aspects of the rupture.

Assuming an average density of 2000 kg/m^3, hydro-

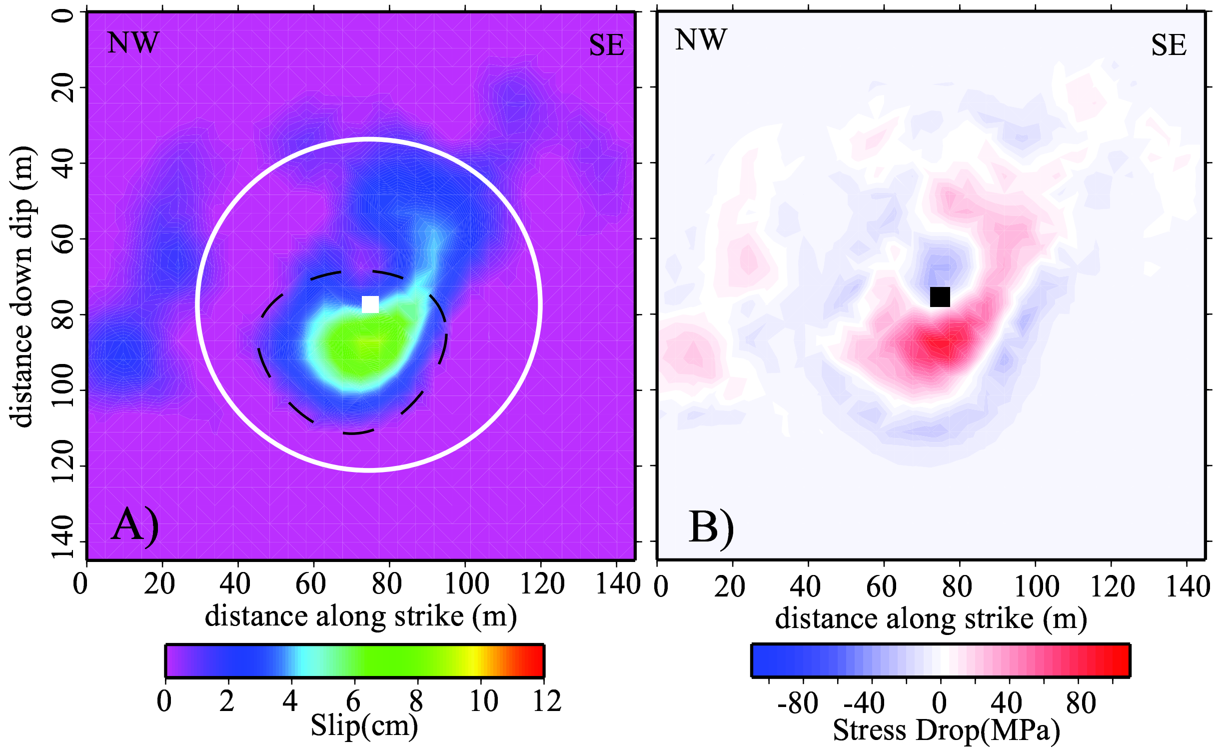

Figure 2.4: A) Slip distribution obtained by inverting moment rate functions from 9 HRSN stations. The hypocenter (white square) is in the center of the assumed rupture plane. The white circle shows the area of a 10MPa event. B) Stress drop obtained by applying the method of Ripperger and Mai (2004)

static pore pressure and a coefficient of friction of 0.4 gives a maximum frictional strength of only 7.8MPa at the depth of the events. On the other hand, it has been proposed that small dimension asperities with strength approaching that of intact rock can concentrate substantial stress levels (*Nadeau and Johnson*, 1998). High stress drop repeating earthquakes may represent those relatively isolated, small-scale, contact points where large stress concentrations can develop and be released on a fairly regular basis. The much larger fault areas of bigger earthquakes may be frictionally weak, but studded with sparsely distributed high strength asperities producing relatively low average stress-drops during large earthquake rupture.

2.1.3 Acknowledgements

This research was upported by the National Science Foundation (EAR-0510108 & EAR-0537641).

2.1.4 References

Dreger, D., Empirical Green's Function Study of the January 17, 1994 Northridge, California Earthquake, *Geophys. Res. Lett.*, 21, 2633-2636, 1994.

Hough, S. E., D. S. Dreger, Source Parameters of the 4/22/92 M6.1 Joshua Tree, California Earthquake and its Aftershocks: Empirical Green's Function Analysis of GEOS and TERRAscope Data, *Bull. Seism. Soc. Am.*, 85, 1576-1590, 1995.

Imanishi, K., W.L. Ellsworth and S.G. Prejean, Earthquake source parameters determined by the SAFOD Pilot Hole seismic array, *Geophys. Res. Lett.*, 31, L12S09, doi:10.1029/2004GL019420, 2004.

Nadeau, R. M., W. Foxall and T. V. McEvilly, Clustering and periodic recurrence of microearthquakes on the San Andreas Fault at Parkfield, California, *Science*, 267, 503-507, 1995.

Nadeau, R. M., and L. R. Johnson, Seismological studies at Parkfield VI: moment release rates and estimates of source parameters for small repeating earthquakes, *Bull. Seism. Soc. Am.*, 88, 790-814, 1998.

Nadeau, R. M., A. Michelini, R. A. Uhrhammer, D. Dolenc, and T. V. McEvilly, Detailed kinematics, structure and recurrence of micro-seismicity in the SAFOD target region, *Geophys. Res. Lett.*, 31, L12S08, doi:10.1029/2003GL019409, 2004.

Ripperger, J. and P. M. Mai (2004). Fast computation of static stress changes on 2D faults from final slip distributions, *Geophys. Res. Lett.*, Vol. 31, No. 18, L18610 10.1029/2004GL020594.

2.2. Accelerating Moment Release in Areas of High Stress? Preliminary Results

Aurélie Guilhem, Roland Bürgmann, Andrew M. Freed (Purdue University), and Tabrez Ali (Purdue University)

2.2.1 Introduction

Several retrospective analyses have proposed that significant increases in moment release occurred prior to many large earthquakes of recent times. However, the finding of Accelerating Moment Release (AMR) strongly depends on the choice of several parameters (magnitude range, area being considered surrounding the events, time period prior to the large earthquake) and the AMR analysis may appear as a data-fitting exercise with no new predictive power. As AMR may relate to a state of high stress around the eventual next epicenter, it is interesting to compare the AMR results to models of stress accumulation in California. Instead of assuming a complete stress drop on all surrounding fault segments implied by the back-slip stress lobe method (*Bowman and King*, 2001), we consider that stress evolves dynamically, punctuated by the occurrence of earthquakes and governed by the elastic and viscous properties of the lithosphere (*Freed et al.*, 2007). We generate several sensitivity tests of the method, as well as a first grid-search analysis for a few large events in Southern California. We also present here a comparison of a more general AMR analysis from 1965 to today with maps of Coulomb stress changes due to all M≥7.0 since 1812, subsequent postseismic relaxation and interseismic strain accumulation.

2.2.2 The AMR concept and data

It has been found that an increase in the number of intermediate earthquakes occurs before a large event which produces a regional increase in the cumulative Benioff strain. This cumulative Benioff strain can be fit by a power law time-to-failure relation (*Bowman et al.*, 1998) which has the following form: $\epsilon(t) = A + B(tc - t)^m$

and

$\epsilon(t) = \sum_{i=1}^{N(t)} \sqrt{E_i(t)}$

where $\epsilon(t)$ is the Benioff strain, N is the number of earthquakes considered, E is the energy of individual earthquakes, tc is the time of the large earthquake and A is the value of the Benioff strain when t=tc. The energy of each particular seismic event is defined as: log(E)=4.8+1.5Ms

To quantify the AMR, we examine the ratio called c-value between the root-mean-square of a power-law time-to-failure function versus a linear fit to the cumulative energy of events. When the c-value is smaller than 0.7, we may consider a case of AMR. The cumulative Benioff strain is then better fit by a power law than by a linear trend.

In the case of using a circular search area for AMR, several parameters (magnitude range, area surrounding the events, time period prior to large earthquake) are required according to the choice of the mainshock studied and the AMR results depends on them.

We study the seismicity of southern California obtained from the ANSS catalog between 32N and 40N latitude since 1910 with a minimum magnitude 3.5. We extract events for AMR calculations following the systematic approach employed in previous studies. We use Nutcracker, a stress and seismicity analysis software to perform all the AMR calculations.

2.2.3 Grid search of AMR for three California earthquakes

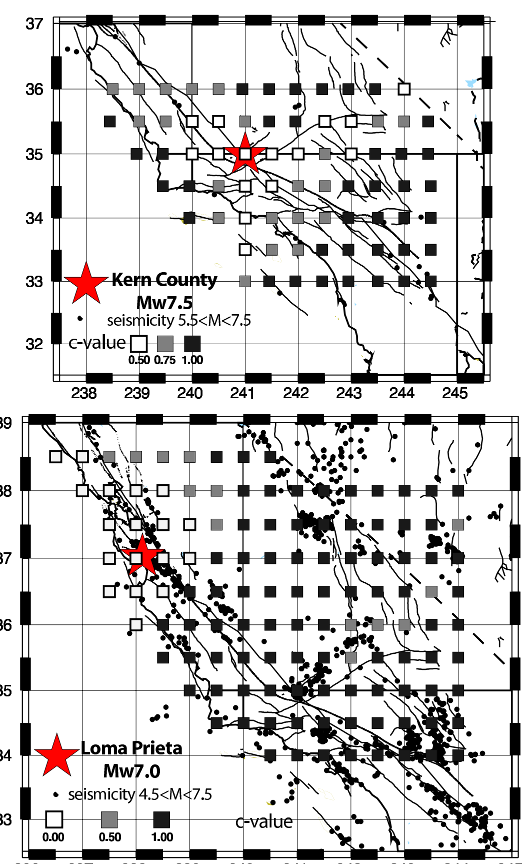

Figure 2.5: Grid search analysis of AMR for Kern County and Loma Prieta

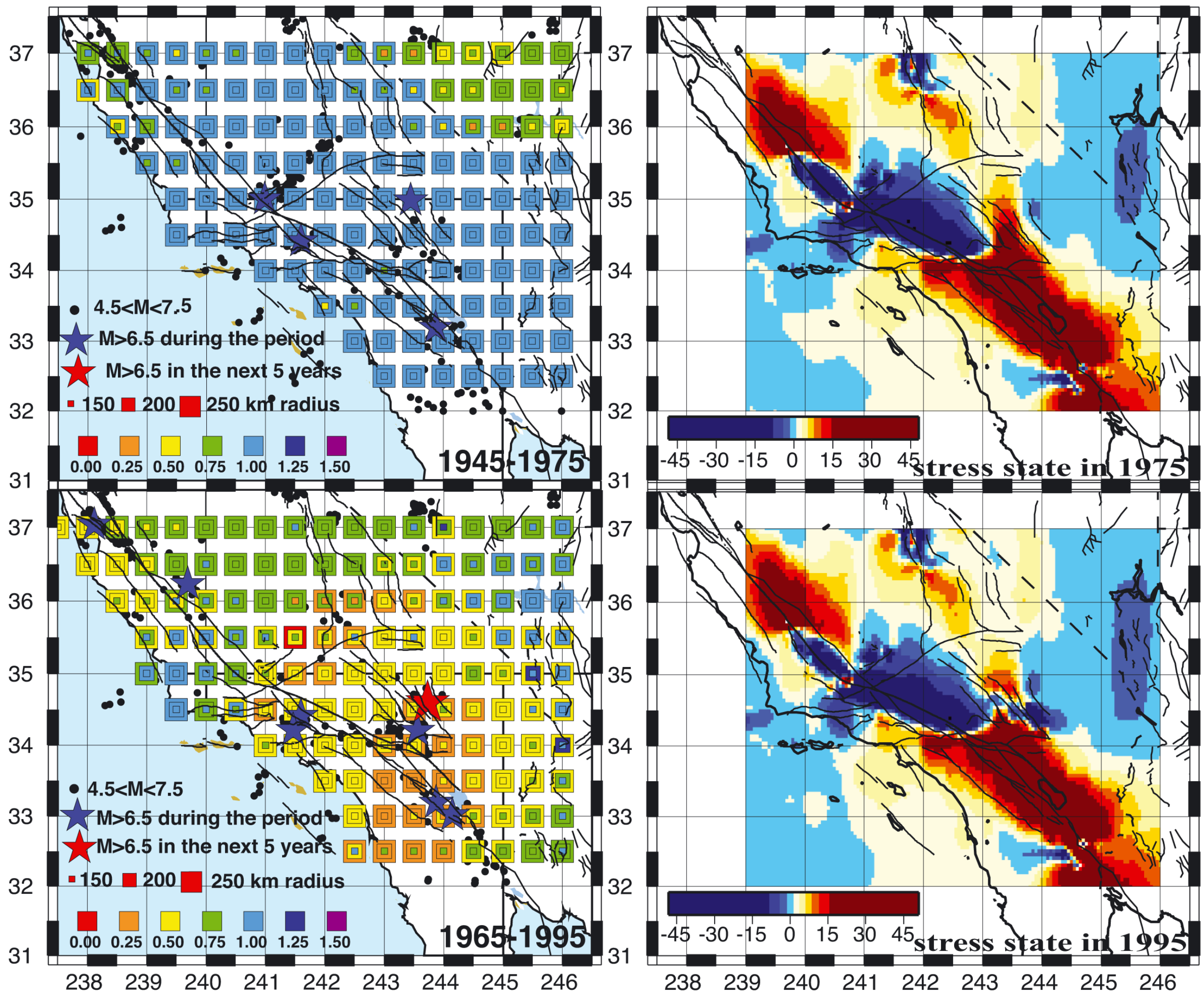

Figure 2.6: Examples of comparison of maps of c-values from AMR circular grid search and of state of stress (bars) for 1975 and 1995.

Figure 2.5 presents two different maps for two large earthquakes of California: Kern County in 1952 and Loma Prieta in 1989. Each map shows the c-values obtained by a grid search analysis over southern California using the same parameters used by *Bowman et al.* (1998): radius of the circular search, period of time and magnitude range. The location of the mainshock is indicated by the star; the seismicity used in the search is represented by black dots.

The first grid search analysis was done with the goal of testing the concept of AMR and to answer the question: Can one find other regions of small c-values with the same parameters outside of the mainshock area?

On the contrary, the two mainshocks are located in the main areas of small c-values at the time of the respective main shocks. The choice of AMR parameters made by Bowman does not result in other potential regions of apparent AMR. However we still have to adjust the three parameters according to the mainshock we study.

2.2.4 AMR grid search maps versus stress change maps

The AMR concept can be interpreted as a data-fitting exercise since there is no general relationship between the radius of the search, the magnitude range and the period of time before the mainshock according to its magnitude. However, based on the results of *Bowman et al.* (1998), the AMR circular search seems to be optimal between 150km and 250km around a magnitude 6.5-7.5 event. Figure 2.6 presents maps of c-values for a possible M7 event in southern California, using a 30-year period of time and three radii: 150km, 200km and 250km. The occurrence of large earthquakes during the tested period increases the c-value, meaning that there is no significant AMR at that time and location. Once the seismicity associated with this event is no longer included in the data set, the results are in better agreement with the seismicity. This is particularly the case for Loma Prieta in 1989 and for Hector Mine in 1999.

Figure 2.6 also presents a comparison between the AMR grid search results and models of stress change over southern California in order to evaluate if areas inferred to be highly stressed also exhibit significant evidence of accelerating seismicity. Rather than assuming a complete stress drop on all surrounding fault segments implied by the back-slip stress lobe (*Bowman and King*, 2001), we consider that stress evolves with time from contributions of coseismic, postseismic and interseismic processes, governed by the elastic and viscous properties of the lithosphere. This emphasizes the importance of postseismic relaxation processes in time-dependent stress transfer and resulting earthquake hazard. Except for the contributions from the largest earthquakes, there is no large variation in the stress pattern with time. The AMR and stress change maps do not look similar when there are many large earthquakes in the periods of the AMR calculations. However, they present similar features in 1985 and 1995.

2.2.5 Discussion and future work

The present work shows the first grid search analysis done for AMR. Adjusting three major parameters of the AMR circular search (radius of the circular region, magnitude range of background seismicity and time period considered), the results of the AMR are positive for large earthquakes in southern California. The comparison of a more general AMR grid search over southern California and stress maps from 1965 to 2005 shows more variable results. The AMR is sensitive to the time and location of larger events during the period of time considered. If a large shock occurs near the beginning of the tested period, the c-value will be larger at the end of the period than if the major earthquake occurs later. More research has to be done especially in the direct comparison of the stress state with seismicity patterns. It would be interesting to remove all the aftershock sequences and test again the similarity between AMR and stress change in southern California. Also, the work should evolve from an AMR circular search to a direct evaluation of a correlation between areas of high stress and AMR.

2.2.6 References

Bowman, D.D., G. Ouillon, C.G. Sammis, A. Sornette, and D. Sornette (1998), An observational test of the critical earthquake concept, *Journ. of Geophys. Res., 103, B10*, 24,349-24,372.

Bowman, D.D. , and G.C.P. King (2001), Accelerating seismicity and stress accumulation before large earthquakes, *Geophys. Res. Lett., 28*, 4039-4042.

Freed, A.M., S.T. Ali, and R. Bürgmann (2007), Evolution of stress in Southern California for the past 200 years from coseismic, postseismic and interseismic stress changes, *Geophys. Journ. Intern., 169*, doi: 10.1111/j.1365-1246X.2007.03391.x.

Hardebeck, J.L., K.R. Felzer, and A.J. Michael (2007), Rigorous observational tests contradict the Accelerating Moment Release hypothesis, unpublished manuscript.

Nutcracker v.X.1.5, geology/fullerton.edu/dBowman/Site/Downloads.html

2.3. Do repeating earthquakes talk to each other?

Kate Huihsuan Chen, Roland Bürgmann, and Robert M. Nadeau

2.3.1 Introduction

What determines the timing of earthquake recurrences and their regularity is of fundamental importance in understanding the earthquake cycle and has important implications for earthquake probability and risk estimates. This question cannot be answered without statistically significant observations of recurrence properties in natural earthquake populations. Historical or paleoseismic data of recurring large earthquakes have thus provided limited information about the degree to which stress interactions between earthquakes may produce some of the variability in earthquake recurrence intervals. A detailed record of micro-earthquake data from the borehole High Resolution Seismic Network (HRSN) and surface Northern California Seismic Network (NCSN) network sites at Parkfield provides a unique opportunity to examine how fault interaction acts on the observed timing and aperiodicity of the repeating events. Taking advantage of a large number of repeating micro-earthquakes with precisely determined relative locations, we analyze the repeating-event catalog for empirical evidence of asperity interaction and then offer a conceptual model for the mechanics of such interaction. We consider 217 repeating-earthquake sequences (REQSs) ranging from M = -0.4 to M = 3 to study their recurrence behaviors in space and time. In this effort, we separate the effect of changes in recurrence intervals that stem from documented coherent accelerations of fault slip, such as have been observed in the mid-1990s and following the 2004 Parkfield earthquake, from those caused by local interactions.

2.3.2 Repeating earthquake sequences from NCSN and HRSN data

The NCSN has reliably located earthquakes to less than M 1 level since 1984, and most sites consist of short-period seismometers. During the period 1984-2004 ending before the Parkfield M6 mainshock, 30 M 1.3 - 3.0 NCSN-derived repeating sequences were identified with a total event number of 178 (*Nadeau and McEvilly*, 2004). With the higher level of detection of micro-earthquakes, the borehole High Resolution Seismic Network (HRSN) has revealed a larger number of repeating earthquakes ranging in magnitude from -0.4 to +1.7. Recording of the HRSN deep borehole sensors began in early 1987, but the original data acquisition system failed in 1998. In August 2001, the HRSN network was upgraded and three new borehole stations were installed to improve resolution of the structure, kinematics and monitoring capabilities in the SAFOD drill-path and target zone. During the period 1987-1998, 187 HRSN repeating sequences were identified with a total event number of 1123. With more sequences that repeat more frequently due to their smaller event size, the HRSN catalog significantly increases the amount of repeating data available for analysis and provides a better opportunity to examine recurrence properties.

2.3.3 Variation in recurrence intervals

The variability of recurrence intervals is represented by the coefficient of variation, COV, the standard deviation divided by the mean of recurrence intervals, and is determined using the events that occurred before the 2004 M6 Parkfield earthquake (filled circles in Figure 2.7). A COV of 0 implies perfect periodicity, while COV=1 implies Poissonian recurrence and COV of greater than 1 indicates temporal clustering. The locations and COVs of repeating earthquake sequences are shown by circles in Figure 2.7, where large circles indicate the REQSs from NCSN data. We find that 50% of the NCSN REQSs are characterized by a COV of less than 0.3, and 67% of these small COV REQSs correspond to zones of low background seismicity, suggesting that these quasi-periodic repeaters are more isolated in space. The aperiodicities of REQSs do not reveal a systematic dependence on depth or magnitude. Following the 29 September 2004, M6.0 Parkfield, California earthquake, a large number of postseismic repeats are observed in many of the 25 updated repeating sequences (1987 - Sept. 15, 2006, which are shown by crosses in Figure 2.7, *Nadeau*, 2007, unpublished data). The event chronologies and time evolution of inter-event time spans (recurrence intervals) for two clusters of REQS are shown in Figure 2.8a and 2.8b, respectively. The events in the cluster in the upper panel (see location in Figure 2.7) reveal a similar pattern, whereas the events in the cluster in the lower panel appear more randomly distributed. We note that the range of separation distances among the REQSs in these two clusters are similar, but the magnitude differences in the upper cluster in Figure 2.8a range from M 0.24 - 0.95 (dM = 0.71), whereas the lower cluster includes events from M 0.58 - 1.70 (dM = 1.12). The larger size difference may play a role in the temporal interaction between the sequence events and requires further examination. We next evaluate how the appearance of temporal interaction correlates with separation distance and magnitude difference among all REQS pairs.

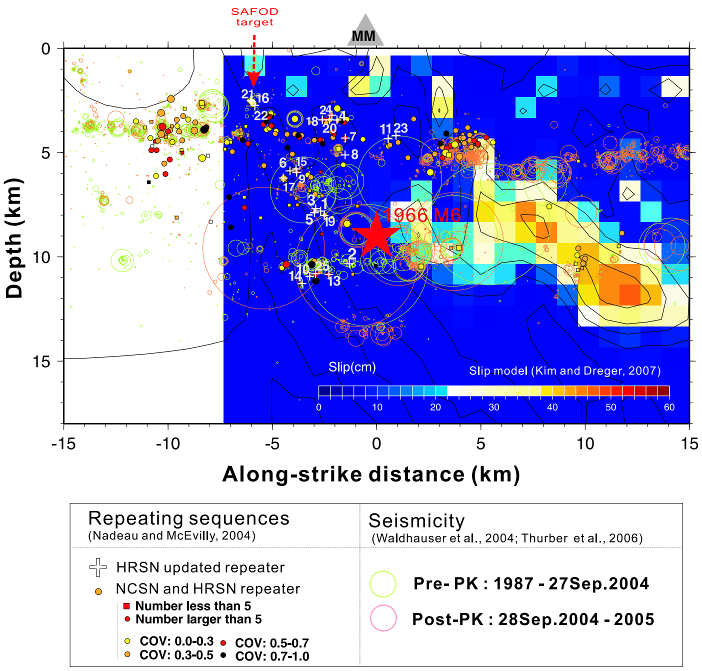

Figure 2.7: Along fault depth section showing the distribution of HRSN (1987 - 1998) and NCSN (1984 - 2004) repeating sequences (filled circles), background seismicity (1987-2005, open circles color coded for pre- and post-2004 earthquake), 1966 M6 hypocenter (red star), and their relationship to the slip distribution of the 2004 Parkfield mainshock (*Kim and Dreger*, 2007). Fill color/shades are keyed to the COV in recurrence interval. White crosses and numbers indicate the updated 25 HRSN repeating sequences.

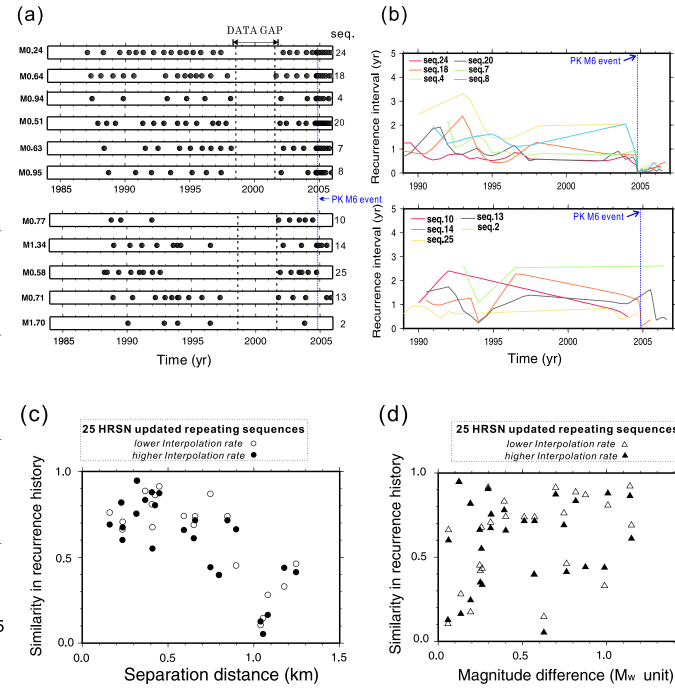

Figure 2.8: (a) Event chronology for two of the updated HRSN REQSs clusters (see white crosses with numbers in Figure 1 for locations). Note that in the upper panel, events rapidly recurred after the 2004 September Parkfield earthquake, which suggests a characteristically decaying afterslip pattern, whereas in the lower panel, the afterslip pattern is not clear. (b) Inter-event time spans (recurrence interval) as a function of time for each REQS in the two clusters. (c) Similarity in recurrence history (cross-correlation coefficient between the curves in (b)) between the 25 updated HRSN REQSs as a function of separation distance using different interpolation intervals. (d) Similarity in recurrence history curve as a function of magnitude difference (in Mw unit) by different interpolation rates. Filled symbols indicate the cross-correlation coefficients calculated by 0.5-yr and 0.1-yr interpolation intervals before and after the 2004 Parkfield earthquake respectively. Open symbols indicate the cross-correlation coefficients from 1-yr and 0.1-yr interpolation intervals before and after the 2004 Parkfield earthquake respectively.

2.3.4 Asperities interacting in time

To illustrate the temporal association between the neighboring REQSs, we have selected the 25 updated HRSN REQSs with more event repeats to calculate the similarity of recurrence interval curves (example shown in Figure 2.8b). We group the REQSs into pairs when the separation distance is less than 1.5 km and then calculate the cross-correlation coefficient between their recurrence curves by different interpolation intervals. Note that the different number of repeats of the REQSs lead to a different sampling rate of recurrence interval curves in Figure 2.8b, which requires interpolation into the same number of data points. High cross-correlation coefficient indicates a similar recurrence-interval history and implies stronger interaction in time and/or correlated slip-rate changes. Taking account of all 25 REQSs, in Figure 2.8c we show that when the separation distance is small, their recurrence histories appear to be similar. The relationship between recurrence history and magnitude difference, however, is unlikely to follow a linear pattern. Following the 29 September 2004, M6.0 Parkfield, California earthquake, a large number of postseismic event repeats occurred, where the sequences show extremely shortened recurrence intervals that gradually increase with time (upper panels in Figure 2.8a and 2.8b). This behavior is consistent with rapid afterslip adjacent to the coseismic rupture that is also evident in geodetic measurements (*Johanson et al., 2006*; *Johnson et al.*, 2006; *Murray and Langbein*, 2006). However, this accelerated recurrence behavior is not obvious for some of the deeper repeating sequences we analyzed (e.g., seqs. 25, 10, 13, 2). Note that events in the seqs. 10 and 2 have not recurred since 2004 (lower panel in Figure 2.8a and 2.8b), suggesting that the Parkfield rupture somehow shut off these REQSs near the NW end of the rupture front, at least for the time being. A less pronounced, but widespread acceleration was also associated with a series of earthquakes with M greater than 4 and accelerated fault creep in the mid-1990s(also evident in the upper panels in Figure 2.8a and 2.8b).

2.3.5 Conclusions

The large population of characteristically repeating earthquakes at Parkfield provides a unique opportunity to study how these asperity ruptures interact with each other. Here we analyze M -0.4 $\sim$ 3.0 repeating earthquake sequences to examine the variation of recurrence properties in space and time. We find that 67% of quasi-periodic repeating sequences (i.e., coefficient of variation in recurrence interval less than 0.3) correspond to zones of low seismicity, suggesting that these more regular repeating events are more isolated in space and from perturbing stress changes. We find that closely spaced repeating sequences show evidence of strong interaction in time, reflected in temporally clustered event recurrences. The temporal correspondence appears to be a function of separation distance from nearby earthquakes rather than the relative size of the events. The response of the repeating events to the occurrence of larger earthquakes provides the clearest documentation of the interaction process. Accelerations of repeating sequences are associated with M 4 - 5 events that occurred in the mid-1990s and following the Parkfield earthquake when a large number of sequences exhibit accelerated recurrence behavior consistent with rapid afterslip following the mainshock. However, the characteristically decaying afterslip pattern is not obvious for some of the repeating sequences located close to the co-seismic slip area, suggesting either that the stress changes are very heterogeneous, or that the rupture erased or shut off some of the sequence source areas. Building on the above observations, we will be able to develop mechanical models that test the extent to which fault interaction in the form of static stress changes and transient postseismic fault creep produces the observed aperiodicity in the occurrence of these events, and furthermore, attempt to improve predictions of the times of future event repeats.

2.3.6 References

Johanson, I. A., E. J. Fielding, F. Rolandone, and R. Bÿgmann, Coseismic and postseismic slip of the 2004 Parkfield earthquake from space-geodetic data, in *Bull. Seism. Soc. Am., 96*, 269-282, 2006.

Johnson, K. M., R. Bürgmann, and K. Larson, Frictional properties on the San Andreas fault near Parkfield, California, inferred from models of afterslip following the 2004 earthquake, in *Bull. Seism. Soc. Am., 96*, 321-338, 2006.

Kim, A., and D. S. Dreger, Rupture process of the 2004 Parkfield earthquake from near-fault seismic waveform and geodetic records, in *Geophys. Res. Lett.*, submitted, 2007.

Murray, J., and J. Langbein, Slip on the San Andreas Fault at Parkfield, California, over Two Earthquake Cycles, and the Implications for Seismic Hazard, in *Bull. Seis. Soc. Am.*, 96, S283 - S303, 2006.

Nadeau, R.M. and T.V. McEvilly, Periodic Pulsing of Characteristic Microearthquakes on the San Andreas Fault, in *Science, 303*, 220-222, 2004.

(Kate Chen has been a visiting scholar in BSL from March 2006 to May 2007) * Department of Earth Sciences, National Cheng Kung University, Tainan, Taiwan

2.4. Segmentation in Episodic Tremor and Slip All Along Cascadia

Richard M Allen and Michael Brudzinski (Miami University)

2.4.1 Introduction

As oceanic plates subduct down into the mantle, friction on the interface with the overriding plate causes stick-slip behavior in the megathrust zone, pulling the upper plate down until it pops back up during a potentially devastating earthquake. Recent observations have also revealed slow slip episodes (SSE) that occur regularly on parts of the deeper plate interface with motion indicating release of accumulated strain (*Dragert et al.*, 2001; *Lowry et al.*, 2001). Their frequency and amount of slip (M_w ~6.5-7.5) (*Melbourne et al.*, 2005) imply they are a substantial portion of the interplate deformation budget. The duration of these episodes is much greater than earthquakes, yet they are accompanied by weeks of non-volcanic tremor (NVT) (*Obara*, 2002; *Rogers and Dragert*, 2003; *Szeliga et al.*, 2004). As such, they represent another section of the strain rate continuum between earthquake and geologic time scales. Processes that govern ETS or potential relationships to major earthquakes and local geology remain unknown, although ETS has been proposed to impact the likelihood of megathrust earthquakes (*Mazzotti and Adams*, 2004).

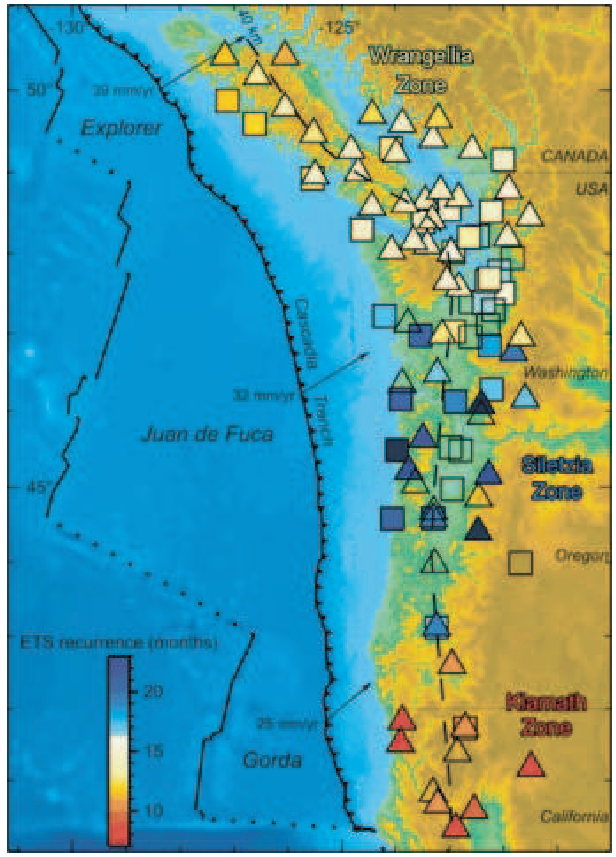

Figure 2.9: Map illustrating patterns in ETS along the entire Cascadia subduction zone. Colored basemap shows topography and bathymetry. Dashed line onshore marks 40 km depth contour of the subduction interface. Arrows and associated annotations show directions and speeds of subduction relative to North America. Locations of continuous GPS stations (squares) and broadband seismometers (triangles) which exhibit ETS are shown, with colors indicating the recurrence interval when multiple ETS events were observed. Recurrence intervals establish 3 zones that are labeled based on the continental terrane block they associate with.

2.4.2 ETS Observations

We utilize a new set of ETS information generated by automated identification of NVT and SSE at individual GPS and seismic stations that circumvents the need for dense networks (*Brudzinski and Allen*, 2007). We find NVT that correlate with SSE in several new locations along the subduction zone, particularly along central Cascadia. Corresponding seismic and GPS data availability ranges from 1 to 8 years, with 30 stations reporting SSE and 55 stations reporting NVT (Figure 2.9) of the over 300 stations that have been investigated with our automated techniques. It is clear that ETS occurs along the entire subduction zone, meaning that localized geological conditions special to a particular site are not controlling factors that prohibit ETS.

2.4.3 ETS Recurrence Intervals

While ETS is observed throughout the Cascadian subduction zone, the characteristics vary coherently along-strike revealing clear segmentation in the recurrence interval and relative timing of ETS events. First, there are 3 broad geographic zones with different recurrence intervals of ETS (Figure 2.9). The average interval across the Siletzia Zone (19±4) is longer than those observed on Vancouver Island to the north (14±2) and is nearly twice as long as that from California to the south (10±2). The broader geographic extent of our ETS measurements relative to previous studies allows us to identify that a coherent Wrangellia Zone extends from northern Vancouver Island down to ~47.5° N, and that a Klamath Zone extends up from the southern end of the subduction zone to ~42.8° N (Figure 2.9).

This pattern of recurrence intervals is not tied to the overall rate of subduction which drives the earthquake cycle as a whole. Overall convergence velocities decrease slowly from the north to the south (Figure 2.9), while the longest recurrence interval occurs in the middle of the subduction zone. We also find the 3 zones of relatively uniform recurrence intervals cannot be explained by age of the subducting plate, implying along strike variations in ETS are not due to temperature changes.

We suggest that the recurrence interval of ETS is related to properties of the overriding continental plate instead of the subducting oceanic plate. The age and temperature of the subducting plate likely has some impact on generating ETS, because initial work has shown SSE and/or NVT are prominent in other young, warm subduction zones like southwest Japan and Mexico (*Hirose and Obara*, 2006; *Larson et al.*, 2004; *Lowry et al.*, 2001; *Obara*, 2002). Yet the oceanic plates subducting beneath Cascadia are relatively uniform compared to the heterogeneity of the continental plate they dive beneath. In fact, the central Siletzia Zone with an ∼18 month recurrence interval corresponds to the relatively low lying and young Coastal Range Block of central and northern Oregon and southern Washington (mostly thick Siletzia terrane). The shorter-recurrence interval zones to the north (Wrangellia) and south (Klamath) correspond to older Pre-Tertiary blocks with higher topography consisting of a melange of old oceanic material with later silicic intrusion in a continental environment. Figure 2.10A shows how ETS recurrence intervals are inversely proportional to onshore fore-arc topography. Correlation of these continental blocks with along-strike patterns of ETS is also consistent with the observation that NVT appears to occur throughout the continental crust at depths above the interface with the subducting oceanic crust.

2.4.4 ETS Segments

The zones of spatially coherent recurrence intervals (Figure 2.9) are further divided into segments where individual events recur over roughly the same location. While the average recurrence intervals of ETS are similar within a given zone, the relative timing between ETS events shows variation with location, a phenomenon that is particularly clear when comparing northern and southern Vancouver Island (*Dragert et al.*, 2004). The extent of these segments is now emerging from the increased number of ETS observations. Figure 2.10B illustrates the phase shift in time between different segments by displaying the timing of ETS observations all along Cascadia, with horizontal lines estimating the along-strike extent of a given episode. Since these are station locations instead of source locations, we would expect the grey lines to extend on the order of 50 km beyond the actual source locations. Dashed vertical lines are approximate boundaries defined by events on either side that are

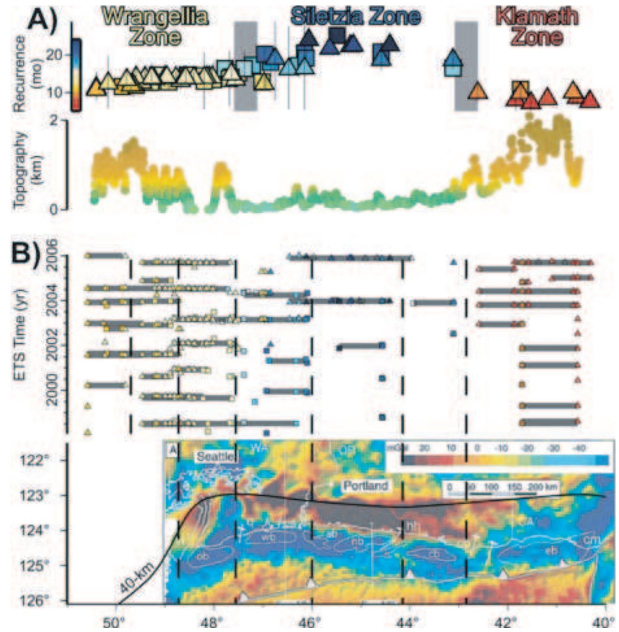

Figure 2.10: Plot of along strike patterns of ETS and upper plate features. (A) Top panel shows distinct variations in ETS recurrence with symbols as in Figure 2.9 and vertical bars show boundaries of observed intervals. Bottom panel shows topography above the 40 km depth contour of the subduction interface, in the middle of ETS observations. Topography is inversely correlated with ETS recurrence, roughly matching the primary continental terranes of different age and composition (Wrangellia, Siletzia, Klamath). (B) Top panel shows "phase" of ETS for 7 different segments along the subduction zone from ETS timing at individual stations. Horizontal grey lines connect stations that record ETS within a month of one another. Bottom panel shows color shaded gravity anomalies and locations of offshore fore-arc sedimentary basins (white lines), features which have been correlated with megathrust asperities on the subduction interface in recent global studies (*Wells et al.*, 2003). Vertical dashed lines show apparent edges of ETS segmentation from currently available data that seem to correlate with megathrust segmentation from the 5 largest sedimentary basins. To deal with trench curvature, station latitudes are those when projected on to 40-km contour (black curve).

separated in time by over a month for greater than 50% of the episodes. We find 7 large segments with along-strike widths of 100-200 km (Figure 2.10B).

The largest segments of ETS occur immediately landward from the proposed locations of asperities on the Cascadia megathrust (*Wells et al.*, 2003). The asperity locations are based on large, low gravity, sedimentary basins in the forearc that have been interpreted to indicate potential seismogenic segmentation at depth. Figure

2.10B shows the along-strike pattern of prominent fore-arc basins for comparison with the spatial extent of ETS segments. The apparent correlation between segmentation of the seismogenic zone and segmentation of the ETS zone suggests that effects of locking (or lack thereof) on the megathrust are transmitted to greater depths where slow slip is believed to occur (*Dragert et al.*, 2001). This spatially links megathrust structure and anticipated seismogenic behavior with ETS characteristics.

2.4.5 Discussion

A remaining question is whether upper plate structure controls plate interface behavior or vice versa. Both models have been proposed for fore-arc basins, with either basins developing in response to locking on the subduction interface (*Song and Simons*, 2003; *Wells et al.*, 2003) or thickness of the upper plate critical wedge controlling the frictional behavior on the plate interface (*Fuller et al.*, 2006). For ETS recurrence, the accreted terranes comprising the upper plate above ETS generate inherently sizable along-strike variations in structure, composition and age that are presumably more significant than long-term effects of ETS on upper plate structure. This supports an interpretation where variations in the Wrangellia, Siletzia, and Klamath blocks control behavior of the ETS source zone. A clue to how continental blocks could be responsible for differences in ETS recurrence is geochemical evidence that the different terranes have different fluid content (*Schmidt and Grunder*, 2006), which could trigger ETS via high pore fluid pressures (*Kodaira et al.*, 2004; *Obara*, 2002). An intriguing hypothesis is that different terrane composition affects rheology of the upper plate and hence the plate interface. For example, the Siletzia terrane would represent denser, stronger, more oceanic-like crust, while the Klamath terrane represents lighter, weaker, more continental-like crust. Such a scenario would suggest that the low-lying Siletzia region has a longer recurrence interval because the upper plate has the strength to accumulate strain for longer periods between SSE.

2.4.6 Acknowledgements

We relied heavily on data from PANGA, IRIS, USGS, CNSN, PNSN, BDSN, and EarthScope. R. Blakely, W.-P. Chen, B. Currie, K. Creager, C. DeMets, H. Deshon, W. Hart, S. Holtkamp, H. Kao, A. Lowry, W. McCausland, T. Melbourne, T. Niemi, W. Szeliga, B. Tikoff, C. Thurber, R. Wells, and an anonymous reviewer provided beneficial feedback. NSF provided support for MB (EAR-0642765, EAR-0510810) and RA (EAR-0643077, EAR-0539987). UW-Madison also provided support for MB and deployment of the OATS array.

2.4.7 References

Brudzinski, M. and R.M. Allen, Segmentation in episodic tremor and slip all along cascadia, *Geology, 35,* 907-910, doi: 10.1130/G23740A.1, 2007.

Dragert, H., G.C. Rogers, J. Cassidy, H. H. Kao, and K. Wang, Episodic tremor and slip in northern Cascadia, *USGS Progress Report, 04HQGR0047,* 1-6, 2004.

Dragert, H., Wang, K. L., and James, T. S., A silent slip event on the deeper Cascadia subduction interface, *Science, 292,* 1525-1528, 2001.

Fuller, C. W., Willett, S. D., and Brandon, M. T., Formation of forearc basins and their influence on subduction zone earthquakes, *Geology, 34,* 65-68, 2006.

Hirose, H., and Obara, K., Short-term slow slip and correlated tremor episodes in the Tokai region, central Japan, *Geophysical Research Letters, 33,* 5, 2006.

Kodaira, S., Iidaka, T., Kato, A., Park, J. O., Iwasaki, T., and Kaneda, Y., High pore fluid pressure may cause silent slip in the Nankai Trough, *Science, 304,* 1295-1298, 2004.

Larson, K. M., Lowry, A. R., Kostoglodov, V., Hutton, W., Sanchez, O., Hudnut, K., and Suarez, G., Crustal deformation measurements in Guerrero, Mexico, *Journal of Geophysical Research-Solid Earth, 109,* B04409, 2004.

Mazzotti, S., and Adams, J., Variability of near-term probability for the next great earthquake on the Cascadia subduction zone, *Bulletin of the Seismological Society of America, 94,* 1954-1959, 2004.

Melbourne, T., Szeliga, W. M., Miller, M. M., and Santillan, V. M., Extent and duration of the 2003 Cascadia slow earthquake, *Geophysical Research Letters, 32,* L04301, 2005.

Obara, K., Nonvolcanic deep tremor associated with subduction in southwest Japan, *Science, 296,* 1679-1681, 2002.

Rogers, G., and Dragert, H., Episodic tremor and slip on the Cascadia subduction zone: The chatter of silent slip, *Science, 300,* 1942-1943, 2003.

Schmidt, M. E., and Grunder, A. L., Segmentation of the Cascade Arc Based on Compositional and Sr and Nd Isotopic Variations in Primitive Volcanic Rocks, *EOS Trans. Am. Geophys. Union, 87,* T53G-02, 2006.

Song, T. R. A., and Simons, M., Large trench-parallel gravity variations predict seismogenic behavior in subduction zones, *Science, 301,* 630-633, 2003.

Szeliga, W., Melbourne, T. I., Miller, M. M., and Santillan, V. M., Southern Cascadia episodic slow earthquakes, *Geophysical Research Letters, 31,* L16602, 2004.

Wells, R. E., Blakely, R. J., Sugiyama, Y., Scholl, D. W., and Dinterman, P. A., Basin-centered asperities in great subduction zone earthquakes: A link between slip, subsidence, and subduction erosion?, *Journal of Geophysical Research-Solid Earth, 108,* 2507, 2003.

2.5. A New Spectral Ratio Method Using Narrow Band Coda Envelopes: Evidence for non-Self-Similarity in the Hector Mine Sequence

Kevin Mayeda, Luca Malagnini (Istituto Nazionale di Geofisica e Vulcanolgia, Roma), William R. Walter (Lawrence Livermore National Laboratory)

2.5.1 Introduction

The use of local and regional S-wave coda is shown to provide stable amplitude ratios that better constrain source differences between event pairs. We first compared amplitude ratio performance between local and near-regional S and coda waves in the San Francisco Bay region for moderate-sized events, then applied the coda spectral ratio method to the 1999 Hector Mine mainshock and its larger aftershocks. We find: (1) Average amplitude ratio standard deviations using coda are 0.05 to 0.12, roughly a factor of 3 smaller than direct S-waves for $0.2 < f < 15.0$ Hz; (2) Coda spectral ratios for the M_w 7.0 Hector Mine earthquake and its aftershocks show a clear departure from self-similarity, consistent with other studies using the same datasets; (3) Event-pairs (Greens function and target events) can be separated by 25 km for coda amplitudes without any appreciable degradation, in sharp contrast to direct waves.

2.5.2 Amplitude Ratios

Do earthquakes scale self-similarly or are large earthquakes dynamically different than small ones? This question is important from a seismic hazard prediction point of view, as well as for understanding basic rupture dynamics for earthquakes. We test the extent to which narrowband coda envelopes can improve upon the traditional spectral ratio using direct phases, allowing a better comparison with theoretical models to investigate similarity. The motivation for using the coda is its stability relative to direct waves and its unique property of spatially homogenizing its energy (*Mayeda et al.*, 2003). Based on prior work on local and regional coda, we hypothesize that amplitude ratios of the same event-pair will be much more stable for coda than for direct S-waves. We tested this hypothesis by forming narrowband amplitude ratios for both wave types and compared their standard deviations for many event pairs. In practice, direct wave empirical Greens function studies have limited their data to co-located events with the same source mechanism. This, however, severely limits the useable amount of data, and if proven feasible, the coda's stability and minimal move-out will allow inclusion of more events that are separated in distance and not necessarily of the same focal mechanism. For both the coda and direct S-waves, we formed amplitude ratios for event pairs by simply subtracting the log10 amplitudes for each sta-

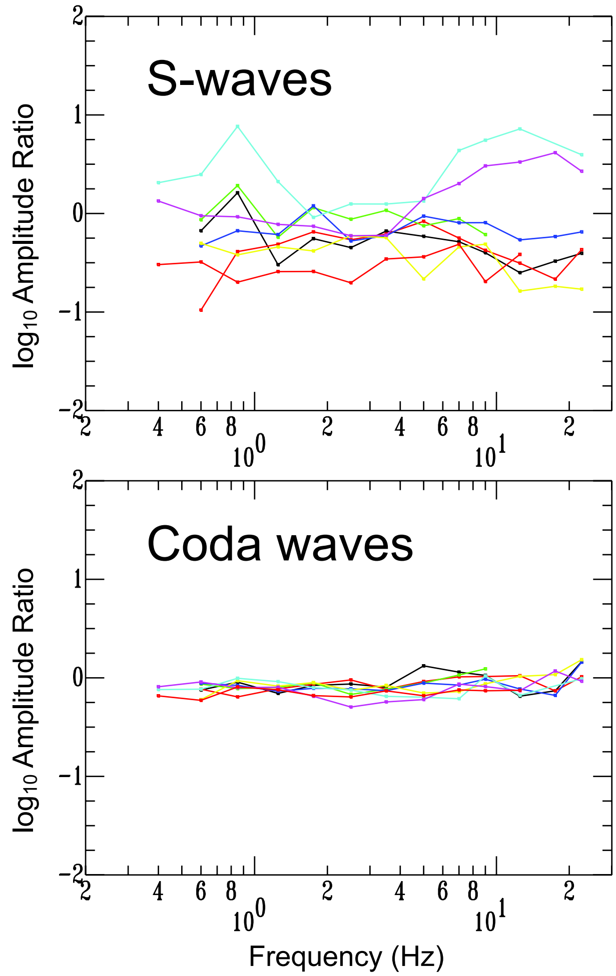

Figure 2.11: An example of amplitude ratios for a pair of events (M_w 3.63 and 3.74) separated by 15.7 km in epicentral distance and identical depths of 7 km. Direct S-wave ratios (top) for 8 color-coded stations show significant scatter over the entire frequency range, whereas the coda wave amplitude ratios (bottom) are very stable from station to station.

tion that recorded the event pair. Since the site and path are the same for both events, the ratio should reflect the source differences in the frequency band. Figure 2.11 shows an example of direct wave amplitude ratios and coda wave ratios. Both events are roughly the same size and, as expected, the log10 average of the ratios is close to 0; however, the direct wave results are significantly more scattered. Using all available ratios, such as the example shown in Figure 2.11, we plot the amplitude ratio standard deviation versus event-pair offset for each frequency band (2.12). The coda amplitude ratios are roughly a factor of 3 smaller and do not show any appreciable increase with event separation, in contrast to the direct waves. This means that the use of the coda will allow for the inclusion of many more events in spectral ratios studies, whereas in direct wave studies, only those events that are virtually co-located are used. Equally important, the coda spectral ratios are significantly less scattered and thus source parameters, such as corner frequency, will be better constrained when we fit the observed data with theoretical source models, such as the commonly used omega-square model (*Aki*, 1967; *Brune*, 1970).

2.5.3 Application to the M_w 7.0 Hector Mine sequence

Next, we turn our attention to local and regional recordings of the M_w 7.0 1999 Hector Mine mainshock and 6 aftershocks ranging between M_w 3.7 and 5.4. In this case we consider 6 broadband stations ranging between 60 and 700 km: GSC, PFO, MNV, CMB, TUC, and ELK. All the events have independent regional seismic moment estimates from full waveform inversion by *G. Ichinose* (pers. comm., 2006). As observed for San Francisco Bay Area events, the coda spectral ratios for Hector Mine events were very stable, with average standard deviations of less than 0.1 for all frequencies. Figure 2.13 shows all 6 ratios, assuming both simultaneous source model fits and individual ratio fits. In all cases the high frequency asymptote is significantly above the theoretically predicted value. This is consistent with a break in self-similarity and is inconsistent with a standard self-similar *Brune* (1970) style omega-square model. Our preferred interpretation is that the apparent stresses are systematically lower for the aftershocks than the mainshock. If all events have Brune-style spectra with an f-2 fall-off at high frequencies, this implies the corner frequency scaling is steeper than f-3 for self-similar, constant apparent stress scaling. More in-depth results of this study can be found in (*Mayeda et al.*, 2007).

2.5.4 Acknowledgements

K. Mayeda was supported under Weston Geophysical subcontract No. GC19762NGD and AFRL contract No. FA8718-06-C-0024. Work by L. Malagnini

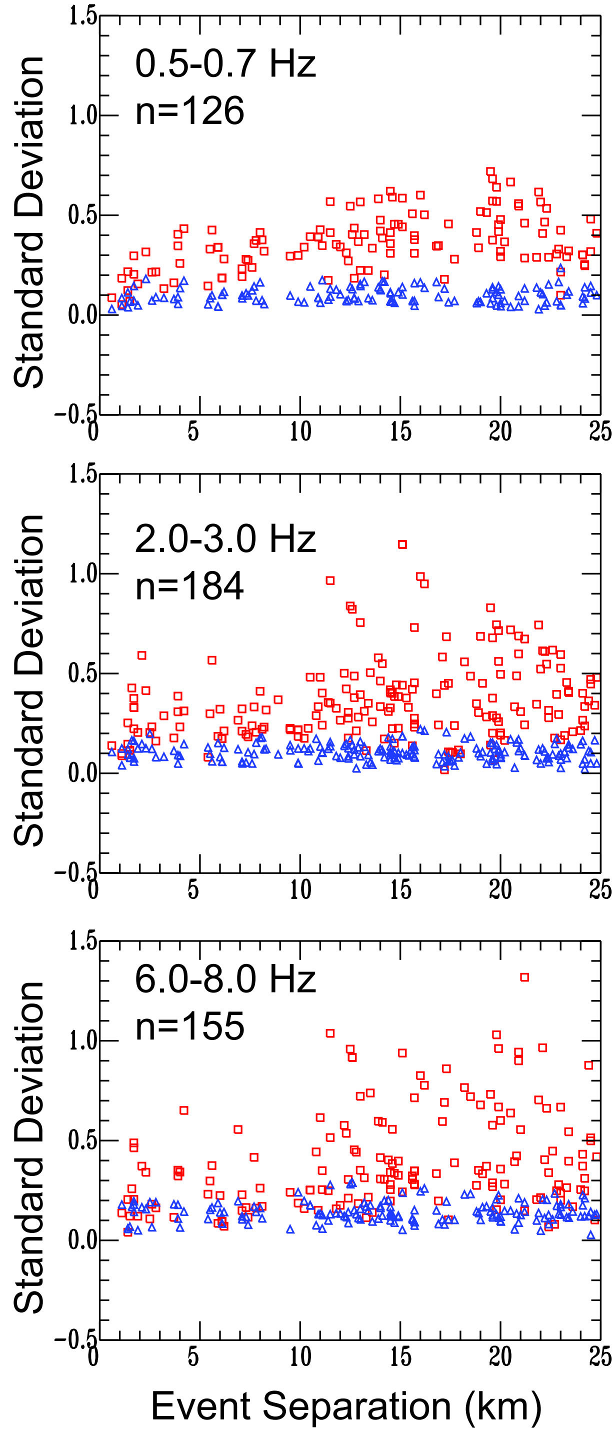

Figure 2.12: For event ratios that had at least 5 stations recording, we plot the amplitude ratio standard deviation versus event separation for coda (triangles) and direct waves (squares) for three frequency bands, 0.5-0.7 Hz (top), 2.0-3.0 Hz (middle), and 6.0-8.0 Hz (bottom). Note that the coda scatter shows almost no dependence upon distance, in sharp contrast with the direct waves and is roughly a factor of 3 smaller.

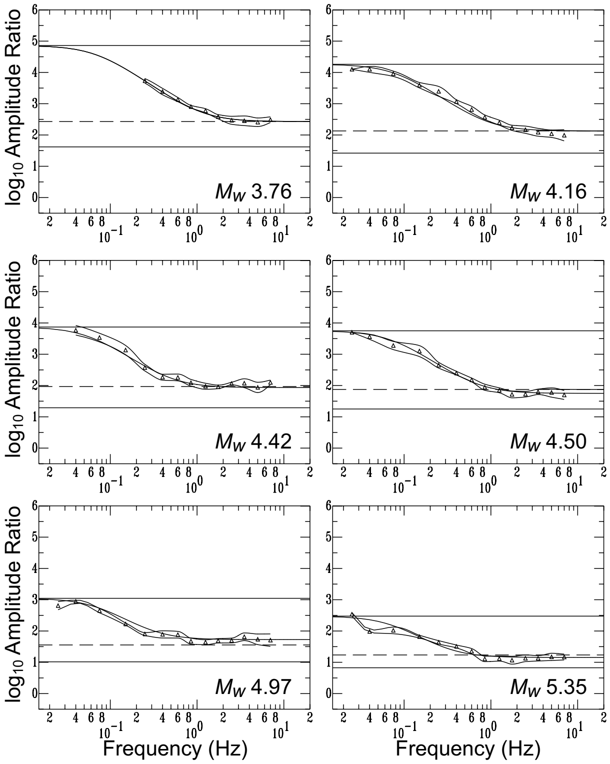

Figure 2.13: Spectral ratios for the Hector Mine mainshock relative to 6 aftershocks. In each figure, we show the low and high frequency asymptotes assuming constant apparent stress scaling as solid lines. Dashed lines show the case if the spectral fall-off were 1.5 rather than 2.0. However, observations worldwide are inconsistent with a fall-off of 1.5 and we are left to assume that the apparent stresses are systematically lower for the aftershocks than the mainshock, breaking similarity.

was performed under the auspices of the Dipartimento della Protezione Civile, under contract S4, ProCiv-INGV (2004-06), project: "Stima dello scuotimento in tempo reale e quasi-reale per terremoti significativi in territorio nazionale". Work by W.R. Walter was performed under the auspices of the U.S. Department of Energy by the University of California, LLNL under contract No. W-7405-Eng-48. This is LLNL contribution UCRL-JRNL-229275.

2.5.5 References

Aki, K. (1967), Scaling law of seismic spectrum. *J. Geophys. Res. 72*, 1217-1231.

Brune, J. N. (1970), Tectonic stress and spectra of seismic shear waves from earthquakes, *J. Geophys. Res. 75*, 4997-5009.

Mayeda, K., A. Hofstetter, J.L. O'Boyle, W.R. Walter (2003), Stable and transportable regional magnitudes based on coda-derived moment-rate spectra, *Bull. Seismol. Soc. Am., 93*, 224-239.

Mayeda, K., L. Malagnini, W.R. Walter (2007), A new spectral ratio method using narrow band coda envelopes: Evidence for non-self-similarity in the Hector Mine sequence, *Geophys. Res. Lett.*, doi:10.1029/2007GL030041.

2.6. Evolution of Tremor Activity at Cholame, CA

Robert M. Nadeau

2.6.1 Introduction

Nonvolcanic tremor (NVT) activity (i.e., long-duration seismic signals with no clear P or S waves) may provide important clues to the rheology and processes responsible for the nucleation and seismic cycles of large earthquakes. Nonvolcanic tremors were first observed in subduction zones (i.e., thrust fault plate boundaries) (e.g., *Obara*, 2002; *Rogers and Dragert*, 2003), where fluids from subduction processes were believed to play an important role in generating these tremors. However, more recently, we have discovered NVT along the San Andreas Fault (SAF) (a transform plate boundary) near Cholame, CA, where subduction related fluids are not present (*Nadeau and Dolenc*, 2005).

2.6.2 SAF Tremors

Our discovery of NVTs beneath Cholame, CA is important for three reasons: 1) they occur along a transform rather than a subduction plate boundary zone, 2) no obvious source for fluid re-charge exists in the Cholame area to aid in tremor genesis, and 3) the highest level of tremor activity in the region occurs beneath the inferred epicentral region of the moment magnitude (M) $\sim$ 7.8 1857 Fort Tejon earthquake, whose rupture zone is currently locked.

2.6.3 Ongoing Activity

Nadeau and Dolenc (2005) found that changes in tremor and micro-earthquake rates at Cholame appeared to correlate. This suggests that deep deformation associated with the Cholame tremors (i.e., ETS) may also be stressing the shallower seismogenic zone in this area. Subsequent monitoring of the Cholame tremors has revealed further evidence for such stress-coupling. Of particular note have been the rate changes associated with the 22 December 2003, M6.5 San Simeon, CA and the 28 September 2004, M6 Parkfield, CA earthquakes (epicenters $\sim$ 50 km west and $\sim$ 10 km NW of Cholame, respectively) that have now been observed (Fig. 2.14).

Between 1 and 3 months before the Parkfield earthquake, tremor activity was relatively low, near pre-San Simeon levels. The activity then spiked between 20 and 22 days prior to the Parkfield mainshock. The relationship of this fore-tremor (FT) to the Parkfield mainshock is suggestive of coupling between deep stress changes associated with the tremors and stress changes in the shallower seismogenic zone leading to the Parkfield M6.0 mainshock.

More profound, however, has been the large and long lasting increase in overall tremor rates following the Parkfield event. Immediately following the the mainshock, tremor rates increased to unprecedented levels that persisted for several days. For several weeks following this period tremor rates remained extremely high but decayed rapidly (similar to the decay of aftershocks in the region). Then, $\sim$ 80 days after the mainshock, tremor rates appear to have entered into a new state where overall rates decay much more slowly and where the dominant pattern of activity exhibits a pattern of multi-scale quasi-periodic variation (i.e., with periodicities of $\sim$ 75 and 330 days). This pattern has persisted up to the time of this report, and it is not yet clear whether the rate behavior reflects solely the response of the tremor source region to stress from the Parkfield mainshock or if mainshock stresses have activated other tremor related processes (e.g., fluid migration or transient deformation).

In any case, the pattern of tremor rate behavior relative to the San Simeon and Parkfield events supports the argument that nearby moderate magnitude earthquakes can stimulate deep NVT activity and that such events may have a significant impact on the long-term evolution of NVT activity. In addition, because the Cholame segment of the SAF has an estimated earthquake recurrence time of 140 years (+93, -69) (*WGCEP*, 1995), and it is now over 140 years since the Fort Tejon event, future increases in SAF tremor activity may signal periods of more rapid stress change and an increased probability for the next large earthquake on the Cholame segment.

2.6.4 Acknowledgments

This research was supported by U.S. Geological Survey award nos. 06HQGR0167 and 07HQAG0014.

2.6.5 References

Nadeau, R.M. and D. Dolenc, Nonvolcanic Tremors Deep Beneath the San Andreas Fault, *Science, 307,* 389, 2005.

Obara, K., Nonvolcanic Deep Tremor Associated with Subduction in Southwest Japan, *Science, 296,* 1679-1681, 2002.

Rogers, G. and H. Dragert, Episodic Tremor and Slip on the Cascadia Subduction Zone: The Chatter of Silent Slip, *Science, 300,* 1942-1943, 2003.

Working Group on California Earthquake Probabilities (WGCEP), Seismic hazards in southern California: probable earthquakes, 1994 to 2024, *Bull. Seism. Soc. Am., 85,* 379-439, 1995.

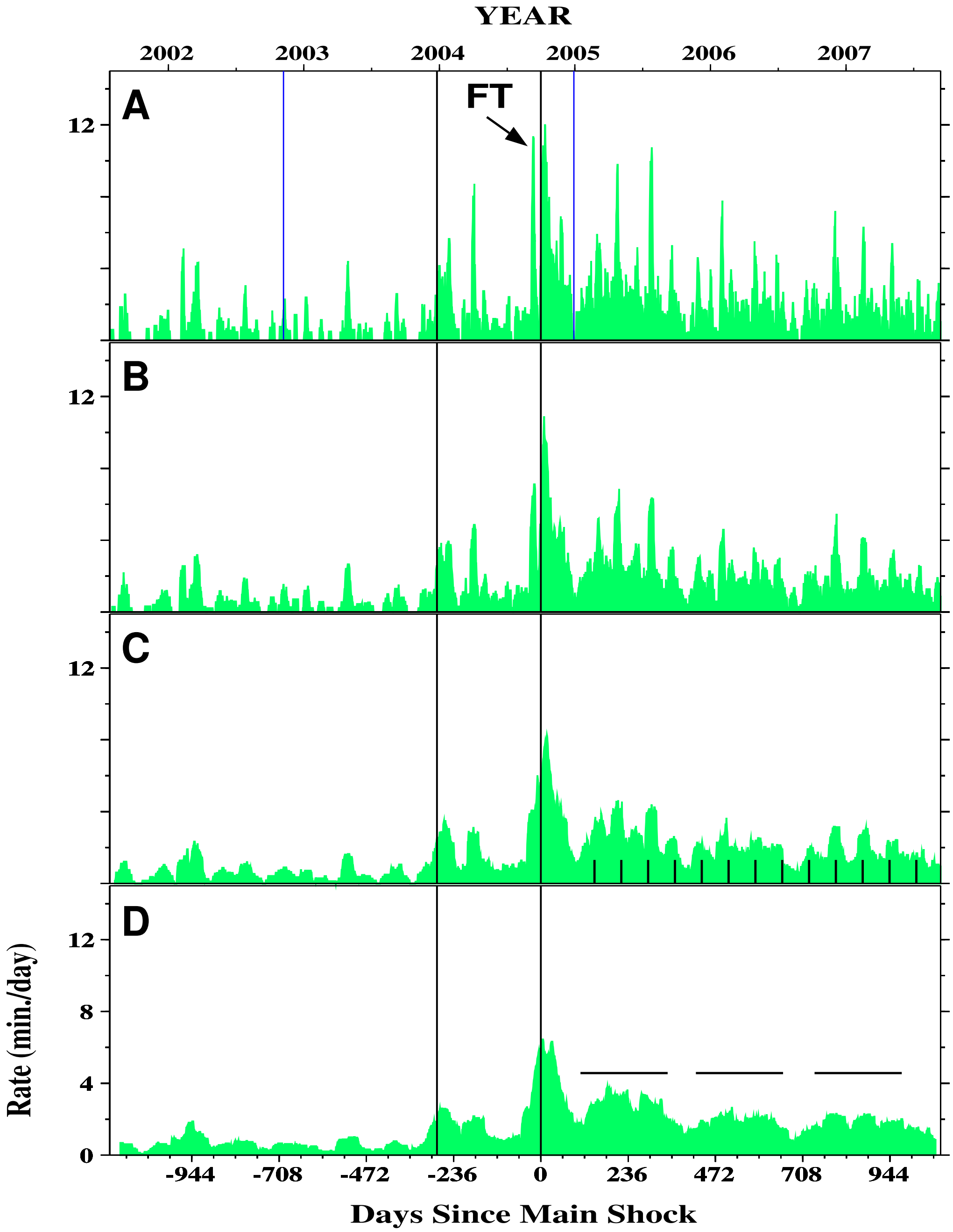

Figure 2.14: Activity rate history of nonvolcanic tremors detected by the borehole High Resolution Seismic Network (HRSN) at Parkfield (PF), CA. Histories span 2240 days (3 years 65 days prior to the PF mainshock to 2 years 349 days after the event). The number of minutes of tremor activity for each day is computed, yielding a time series of activity rates with sampling interval of 1 day. The time series is then smoothed with boxcars of 4 different window lengths (panel A, 7.5 days; B, 15 days; C, 30 days and D, 60 days) stepped at daily intervals with values plotted at the center of each window. This is done to help illustrate the multi-scale periodicity of the data. Black lines spanning all four panels are times of the 2003 and 2004 San Simeon and PF earthquakes. Black lines in panel 1 are times of the 2002 Denali M8.1 and 2004 Sumatra M9.3 earthquakes. Triggering of tremor activity from these global events appears to be relatively insignificant compared to triggering related to the San Simeon and PF events. FT refers to apparent fore-tremor event preceding the PF mainshock. Small vertical dashes (Panel C) are 75 day intervals approximating periodicity on this scale following the PF mainshock. Short horizontal lines (panel D) show the approximate 330 day rate pulses.

2.7. Regional Analysis of *Lg* Attenuation: Comparison of 1D Methods in Northern California

Sean R. Ford, Douglas S. Dreger, Kevin Mayeda, William R. Walter (Lawrence Livermore National Laboratory), Luca Malagnini (Istituto Nazionale di Geofisica e Vulcanologia), William S. Phillips (Los Alamos National Laboratory)

2.7.1 Introduction

Understanding of regional attenuation Q^{-1} can help with structure and tectonic interpretation (*Aleqabi and Wysession*, 2006; *Benz et al.*, 1997; *Frankel*, 1990), and correcting for the effects of attenuation can lead to better discrimination of small nuclear tests (e.g. *Baker et al.*, 2004; *Mayeda et al.*, 2003; *Taylor et al.*, 2002). Present threshold algorithms for event identification rely on Q models that are derived differently, and the models can vary greatly for the same region. In a recent submission to the Bulletin of the Seismological Society of America (*Ford et al., 2007*) we characterize the difference between popular 1-D Q methods, and the difference within each method based on parameterization choice.

2.7.2 Data & Methods

The dataset consists of 158 earthquakes recorded at 16 broadband (20 sps) three-component stations of the BDSN between 1992 and 2004. The wide distribution of data parameters allows for sensitivity testing. We calculate Q_{Lg} by fitting the power-law model, $Q_0 f^\eta$ using five different methods. The first two methods use the seismic coda to correct for the source effect. The last three methods use a spectral ratio technique to correct for source, and possibly site effects.

The coda normalization (CN) method uses the local shear-wave coda as a proxy for the source and site effects, thus amplitude ratios remove these two effects from the S-wave spectrum (*Aki*, 1980; *Yoshimoto et al.*, 1993). The coda-source normalization (CS) method uses the stable, coda-derived source spectra to isolate the path attenuation component of the Lg spectrum (*Walter et al.*, 2007). The two-station (TS) method takes the ratio of Lg recorded at two different stations along the same narrow path from the same event in order to remove the common source term (e.g., *Chavez and Priestley*, 1986; *Xie and Mitchell*, 1990). The reverse two-station (RTS) method uses two TS setups, where a source is on either side of the station pair in a narrow azimuthal window (*Chun et al.*, 1987). The two ratios are combined to remove the common source and site terms. The source-pair/receiver-pair (SPRP) method is the RTS method with a relaxation on the narrow azimuthal window requirement (*Shih et al.*, 1994).

2.7.3 Method Comparison

Since each method has a different data requirement it is improper to compare the methods with the full dataset. For example, the CN method will sample geology at all back-azimuths relative to a station, whereas the RTS method is restricted to a narrow azimuthal window aligned roughly along a pair of stations and events. In an attempt to normalize the dataset used for each method, we restrict the data to lie in a small region along the Franciscan block (Figure 2.15a). We implement all five methods to calculate $Q_0 f^\eta$ in the region (Figure 2.15b). The populations are then smoothed with a two-dimensional gaussian kernel (*Venables and Ripley*, 2002) to produce an empirical distribution so that the 95% confidence region can be estimated. The grey region in Figure 2.15 represents a parameter space that fits all studies.

2.7.4 Acknowledgements

Figures were made with Generic Mapping Tools (*Wessel and Smith*, 1998).

2.7.5 References

Aki, K. (1980). Attenuation of shear-waves in the lithosphere for frequencies from 0.05 to 25 Hz, *Phys. Earth Planet. Inter. 21*, 50-60.

Aleqabi, G. I., and M. E. Wysession (2006). Q(Lg) distribution in the basin and range province of the western United States, *Bull. Seism. Soc. Amer. 96*, 348-354.

Baker, G. E., J. Stevens, and H. M. Xu (2004). Lg group velocity: A depth discriminant revisited, *Bull. Seism. Soc. Amer. 94*, 722-739.

Benz, H. M., A. Frankel, and D. M. Boore (1997). Regional Lg attenuation for the continental United States, *Bull. Seism. Soc. Amer. 87*, 606-619.

Chavez, D. E., and K. F. Priestley (1986). Measurement of frequency dependent Lg attenuation in the Great Basin, *Geophys. Res. Lett. 13*, 551-554.

Chun, K., G. F. West, R. J. Kokoski, and C. Samson (1987). A novel technique for measuring Lg attenuation; results from Eastern Canada between 1 to 10 Hz, *Bull. Seism. Soc. Amer. 77*, 398-419.

Ford, Sean R., Dreger, D.S., Mayeda, K., Walter, W.R., and Luca Malagnini (2007). Regional Analysis of *Lg* Attenuation: Comparison of 1D Methods in Northern California, submitted to *Bull. Seism. Soc. Amer.*

Frankel, A. (1990). Attenuation of high-frequency shear waves in the crust: measurements from New York

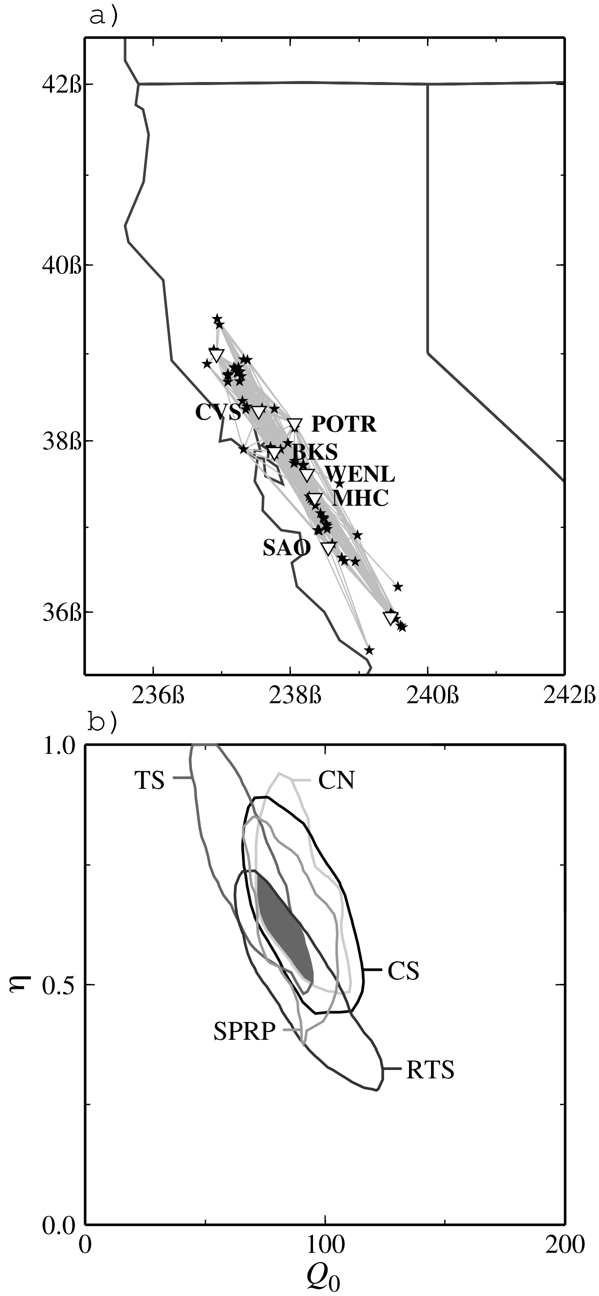

Figure 2.15: Method comparison. a) Map of the subset used in the comparison analysis. Data are in a small region near the San Francisco Bay Area, primarily along the Franciscan block. b) Power-law parameters and their empirical 95% confidence regions are given. The intersecting region is shaded grey.

State, South Africa, and Southern California, *J. Geophys. Res. 95*, 17441-17457.

Mayeda, K., A. Hofstetter, J. L. O'Boyle, and W. R. Walter (2003). Stable and transportable regional magnitudes based on coda-derived moment-rate spectra, *Bull. Seis. Soc. Amer. 93*, 224-239.

Shih, X. R., K. Y. Chun, and T. Zhu (1994). Attenuation of 1-6 s Lg waves in Eurasia, *J. Geophys. Res. 99*, 23-23,875.

Taylor, S., A. Velasco, H. Hartse, W. S. Philips, W. R. Walter, and A. Rodgers, (2002). Amplitude corrections for regional discrimination, *Pure. App. Geophys. 159*, 623-650.

Venables, W. N., and B. D. Ripley (2002). Modern Applied Statistics with S, Springer, New York.

Walter, W. R., K. Mayeda, L. Malagnini, and L. Scognamiglio (2007). Regional body-wave attenuation using a coda source normalization method: Application to MEDNET records of earthquakes in Italy, *Geophys. Res. Lett. 34*, L10308.

Wessel, P., and W. H. F. Smith (1998). New, improved version of generic mapping tools released, in American Geophysical Union, San Francisco, Vol. 79, 579.

Xie, J., and B. J. Mitchell (1990). Attenuation of multiphase surface waves in the Basin and Range Province; Part I, Lg and Lg coda, *Geophys. J. Int. 102*, 121-137.

Yoshimoto, K., H. Sato, and M. Ohtake (1993). Frequency-dependent attenuation of P and S waves in the Kanto area, Japan, based on the coda-normalization method, *Geophys. J. Int. 114*, 165-174.

2.8. A simple method for simulating microseism H/V spectral ratio in 3D structure

Junkee Rhie and Douglas Dreger

2.8.1 Introduction

The understanding of 3D basin structure is very important in the estimation of damaging strong shaking. Since *Nakamura* (1989) first used ambient noise to estimate the site amplification, several techniques to delineate 3D basin structure using background noise have been developed. The advantage of the background noise approach is that ambient seismic noise is ubiquitous and continuous. It means that we don't need to wait for earthquakes or detonate expensive explosions for studying structure. *Dolenc and Dreger* (2005) showed that the frequency of the dominant H/V spectral peak (hereafter referred to as FDP) due to microseisms correlates with the thickness of the Santa Clara Valley (SCV). However, the synthetic FDPs for one dimensional models could not explain the observed shifts of the FDP. This result indicates that 2D and 3D wave propagation effects should be considered for the deep basins when their thickness is comparable to their size. In this study, we developed a simple method to compute FDP due to microseisms for 3D basin models and applied the new method to predict observed FDPs during Santa Clara Valley Seismic Experiment (SCVSE)(*Lindh et al.*, 1999).

2.8.2 Method

Microseisms are dominant seismic noise in the frequency range from 0.1 to 5 Hz and they are generated by pressure changes on the ocean bottom. Since understanding of the coupling mechanism between the ocean and sea floor is limited, the reliable simulation of the microseism wavefield is quite difficult. Fortunately, *Dolenc and Dreger* (2005) found that FDP is independent of the level of microseism excitations. This observation indicates that the H/V ratio is not dependent on the detailed source process of the microseisms because taking the H/V ratio inherently cancels the source effects and enhances the propagation effects. We have developed a simple method to simulate FDP due to microseisms or any continuous sources for given 3D velocity models. Our new method is tested by comparing the synthetic FDPs to observations from SCVSE (Figure 2.16). The method is very straightforward and consists of 5 steps. First, we compute Green's functions using a 3D finite-difference code (E3D; Larsen and Schulz, 1995). Here we assume a shallow (500m depth) vertical CLVD source as the source of the microseisms in the continental margin, and a simple Gaussian source time function is applied. Second, the Gaussian source time function is deconvolved from the synthetics. Third, in order to reduce grid-dispersion effects (e.g. Levander, 1988) a low pass filter with a corner frequency of 0.8 Hz is applied to synthetics. Fourth, continuous monochromatic sine waves for discrete frequencies over the range from 0.025 to 0.8 Hz, with an interval of 0.025 Hz, are convolved with the low-pass filtered synthetic waveforms for each station. Finally, maximum amplitudes of convolved waveforms of three components for each frequency are taken in the time window after amplitudes become stable. The final horizontal maximum is determined by taking the geometric mean of two maximum horizontal amplitudes. In this study, the definition of the H/V spectral ratio is just the ratio of maximum vertical and horizontal amplitudes as a function of frequency. Since synthetic vertical and horizontal amplitudes are not stably varying with frequency, and sometimes abnormally small vertical amplitudes cause unrealistic peaks in the H/V ratio, the moving average over 5 adjacent data points is applied to the horizontal and vertical amplitudes before taking the H/V ratio.

2.8.3 Results and Discussion

We computed three FDPs for three different 3D Santa Clara Valley velocity models. The first model is the San Francisco Bay Area model from USGS (USGS Bay Area Velocity Model 05.1.0). The second model is the UC Berkeley (UCB) 3D model (*Stidham et al.*, 1999). The third model is a modified USGS model. In this modified velocity model, in order to enhance the effect due to the basin structure, we kept the velocity structure inside the basin, but assumed only 1D reference velocity structure for the regions outside of the basin. The comparison between synthetic and observed FDPs shows that FDPs for USGS and modified USGS models follow a similar depth dependent trend as observed FDPs, and their absolute values are in agreement as well (Figure 2.17). The synthetic FDPs for the UCB model show that FDP correlates with basin depth up to 2 km, but the correlation coefficient is not high and individual values are more scattered than in the case of the other models, especially for shallow depths. We also cannot match the observed shift of the trend in the observed FDP curve at around 2 to 3 km depth because the maximum thickness of the basin obtained in the UCB model is only 2 km.

The observation and synthetic results show that the variations in FDP are sensitive to the thickness of the basin up to a certain depth and then becomes stable. The simulation of the P-wave time delays from teleseis-

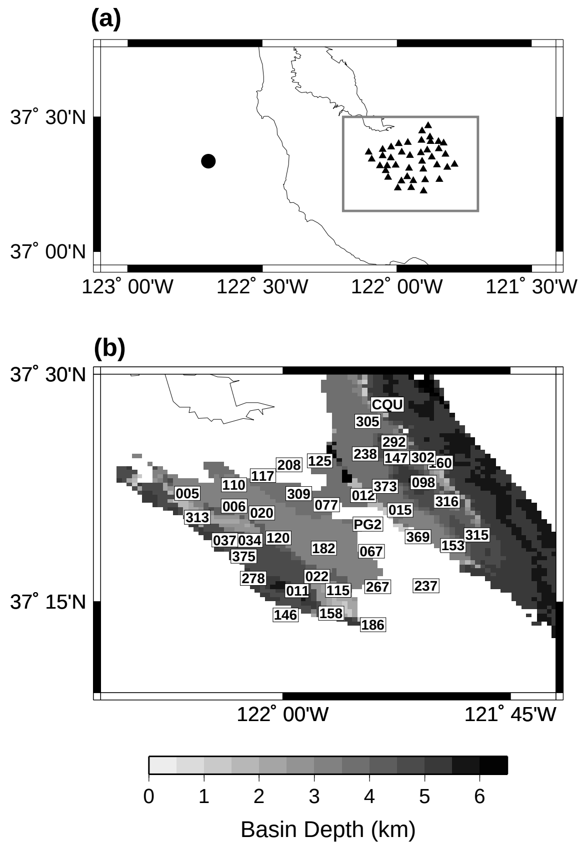

Figure 2.16: (a)The range of 3D models used for synthetic Green's function computation. Small triangles indicate the stations deployed during Santa Clara Valley Seismic Experiment (SCVSE). Solid circle represents assumed location of the microseism source. (b) The background shading indicates the depth of the Santa Clara Valley obtained from the 3D USGS velocity model

mic events for the USGS 3D velocity model at SCVSE stations shows a similar saturating trend as the FDPs for the USGS model (Dolenc et al., 2005). Synthetic time delay increases with increasing basin thickness up to a certain depth and then stabilizes. Since the P-wave time delay depends entirely on the mean velocity and thickness of the basin, this indicates that velocity contrast between the basin and the background medium is negligible at deeper depth, which is true for USGS 3D velocity model. In the case of the Santa Clara Valley model, FDP is only sensitive to the shallow structure, and the apparent thickness of the deeper part of the basin is much shallower than the model. It is likely due to the negligible velocity contrast in Santa Clara Valley model. But we still need more experiments to confirm which factor really controls the depth of the change in the depth-dependent trend of the FDP.

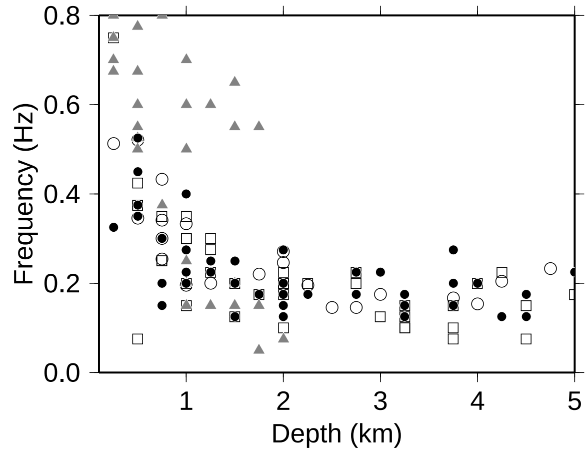

Figure 2.17: A comparison among observed (open circles)) and three synthetic FDPs for USGS (Open squares), modified USGS (Solid circles) and UCB (Gray triangles), as a function of depth.

2.8.4 Acknowledgements

We thank the USGS and IRIS for providing the velocity model and seismic data. We also thank David Dolenc for providing his observed FDPs.

2.8.5 References

Dolecn, D., D. Dreger, and S. Larsen, Basin Structure Influences on the Propagation of Teleseismic Waves in the Santa Clara Valley, California, *Bull. Seism. Soc. Am. 95*, 1120-1136, 2005.

Dolenc, D., and D. Dreger, Microseisms observations in the Santa Clara Valley, California, *Bull. Seism. Soc. Am. 95*, 1137-1149, 2005

Larsen, S., and C. A. Schultz, ELAS3D: 2D/3D elastic finite difference wave propagation code, Technical Report No. UCRL-MA-121702, 19 pp, 1995.

Levander, A. R., Fourth-order finite-difference P-SV seismograms, *Geophysics 53*, 1425-1436, 1988.

Lindh, A. G., J. P. Eaton, M. O. Allen, J. H. Healy, S. W. Stewart, and L. Damerell, Calibration formulae and values for velocity seismometers used in the 1998 Santa Clara Valley, California seismic experiment, *U.S. Geol. Surv. Open-File Rept.* 99-434, 1999.

Nakamura, Y., A method for dynamic characteristics estimation of subsurface using microtremor on the ground surface, *QR Railway Tech. Res. Inst. 30*, 1, 1989.

Stidham, C., M. Antolik, D. Dreger, S. Larsen, and B. Romanowicz, Three-dimensional structure influences on the strong-motion wavefield of the 1989 Loma Prieta earthquake, *Bull. Seism. Soc. Am. 89*, 1184-1202, 1999.

2.9. Broadband Modeling of 3D velocity structure in the San Francisco Bay Area

Ahyi Kim, Douglas Dreger, and Shawn Larsen

2.9.1 Introduction

We performed 3D ground motion simulations for 9 recent moderate earthquakes in the San Francisco Bay Area to evaluate the USGS SF06 3D velocity model (Brocher et al., 2005; Jachens et al., 2005) in terms of modeling phase arrival timing, peak ground motion amplitudes, and general seismic waveforms. In addition, we performed forward modeling to obtain 3d structure modifications to improve the fit to available data.

2.9.2 Computational set up and 3D model used in the simulations

ID	Date	lon	lat	Strike	Dip	Rake	Depth	Moment	Mw
gilr93016	01/16/1993	-121.455	37.028	331	83	166	7	2.40E+23	4.9
boli99230	08/18/1999	-122.686	37.907	115	49	69	8	7.25E+22	4.5
napa00247	09/03/2000	-122.414	38.377	60	75	18	11	3.74E+23	5
gilr02134	05/14/2002	-121.6	36.967	212	87	-6	8	2.86E+23	4.9
dubl03033	02/02/2003	-121.937	37.74	67	88	-19	14	1.36E+22	4.1
smar06166	06/15/2006	-121.492	37.102	360	78	-152	5	4.18E+22	4.4
glen06215	08/03/2006	-122.589	38.363	256	86	19	5	5.64E+22	4.4
lafe07061	03/02/2007	-122.098	37.901	82	89	-1	14	2.77E+22	4.2
oakl07202	07/20/2007	-122.18	37.8	321	89	168	5	2.52E+22	4.2

Figure 2.18: Table 1. Earthquake simulated in this study. Event ID and the source parameters are obtained from BSL Moment Tensor Catalog.

For the 3D waveform modeling, we used the elastic finite-difference code, E3D developed by Larsen and Schultz (1995). With the BSL cluster we can simulate ground motions throughout the greater San Francisco Bay Region to a maximum frequency of 0.5 Hz for models with a minimum wave speed of 500m/s. We have performed simulations of 9 Mw4.1-5.0 events using source parameters obtained from the BSL Moment Tensor Catalog (Figure 2.18:Table 1). Broadband seismic data was obtained form the Berkeley Digital Seismic Network (BDSN), and strong motion data was obtained from the USGS strong Motion Instrumentation Program (SMIP) and the California Geologic Survey (CGS) California Strong Motion Instrumentation Program (CMSIP). The data was corrected to absolute ground velocity (cm/s). We compare synthetic and observed ground velocity in three passbands, namely 0.03-0.15Hz, 0.1-0.25Hz, and 0.1-0.5Hz.

2.9.3 Modeling results

From the 3D waveform simulations, we found that the USGS model explains important features of the overall waveforms very well, but the synthetics arrive earlier than the observations at all distances. The records and synthetics were cross-correlated to determine the delay time (dt) for optimal alignment. (Figure 2.19). The cross-correlations of both P-waves and S-waves (Rodgers et al., 2007) show systematic delays indicating that on average the USGS 3D model is too fast.

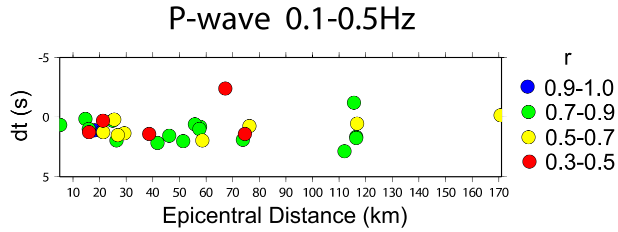

Figure 2.19: Delay time dt is estimated by cross-correlating the data and synthetic waveform pairs in 0.1-0.5Hz. The time axis is relative to the reported origin time.

Figure 2.20 shows the synthesized PGV in the 0.1-0.5 Hz in map view, and waveform comparisons in the 0.03-0.15Hz, 0.1-0.25Hz and 0.1-0.5Hz passbands for the Bolinas event. The synthetic PGV correlates well with the sedimentary basins and bedrock ridges, in that it is relatively larger in sedimentary basins and lower on bedrock ridges compared to what is computed with a 1D layered velocity structure and the same source parameters. For example, elevated shaking was observed in the distant Hollister valley as well as the San Francisco Bay region. The waveform comparison shows a very good fit in the 0.03-0.15 and 0.1-0.25Hz passband, except the POTR path. This west to east path crosses the northern San Francisco Bay area through the delta region, and evidently requires further model refinement. Waveform modeling of several paths crossing the region is ongoing.

2.9.4 References

Brocher, T. M., (2005). Emprical relations between elastic wave speeds and density in the Earth's crust, *Bull. Seism. Soc. Am.*, 95 No. 6, 2081-2092. Dreger D. and B. Romanowicz (1994). Source Characteristics of Events in the San Francisco Bay Region, USGS open-file report, 94-176, 301-309.

Jachens, R., R. Simpson, R. Graymer, C. Wentworth, T. Brocher (2006). Three-dimensional geologic map of northern and central California: A basic model for supporting ground motion simulation and other predictive modeling, 2006 SSA meeting abstract, *Seism. Res. Lett.*, 77, No.2, p 270.

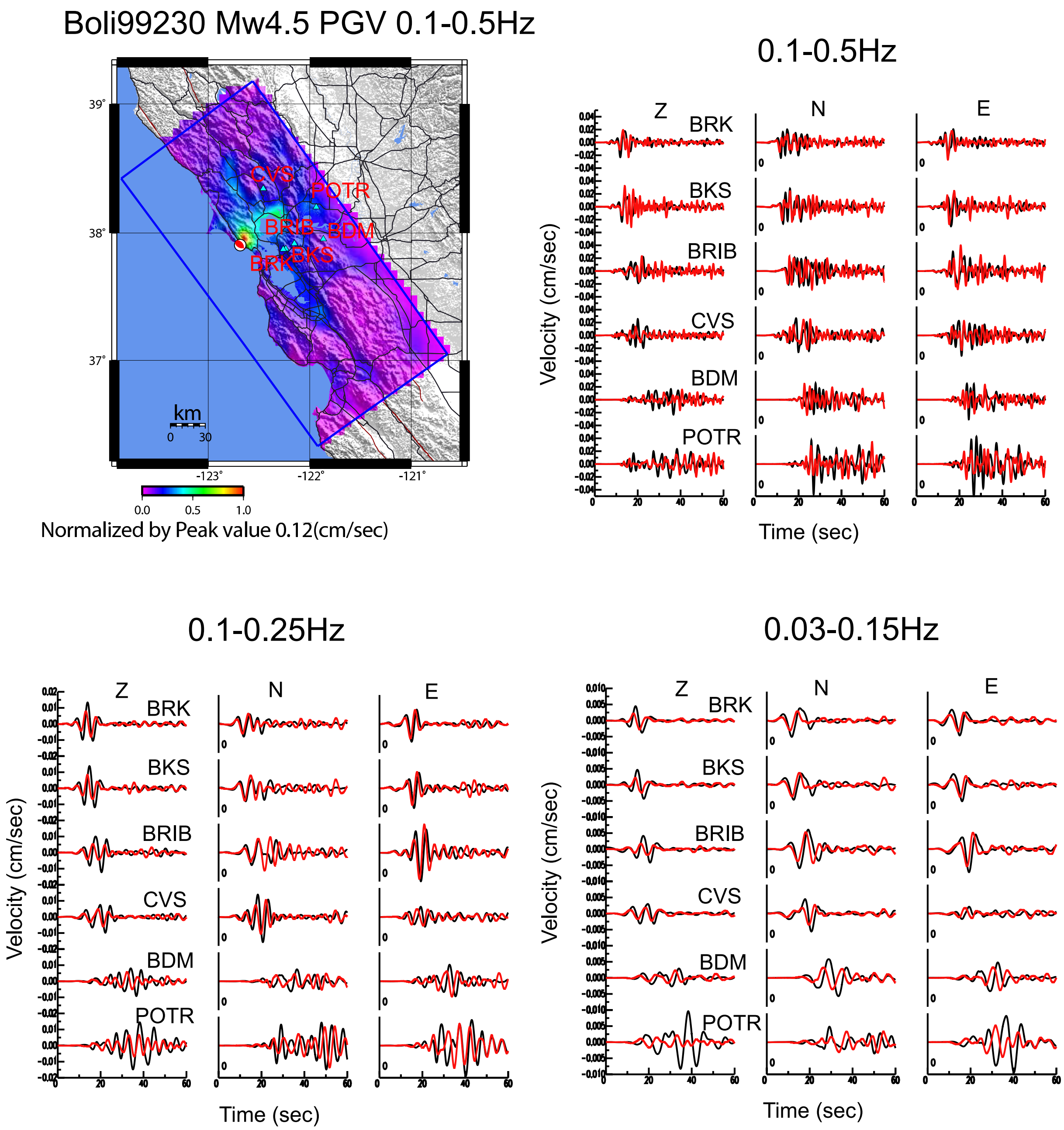

Figure 2.20: (Top left) Synthetic PGV ShakeMap for the Bolinas earthquake in 0.1-0.5Hz passband. Comparison between the data (black) and synthetics (red) in 0.1-0.5Hz (Top right), 0.1-0.25Hz (Bottom left), and 0.03-0.15Hz (Bottom right).

2.10. Inversion of the Teleseismic Observations for the Velocity Structure Within the Santa Clara Valley Basins

David Dolenc (now at U of Minnesota), Doug Dreger, and Shawn Larsen (LLNL)

2.10.1 Introduction

Previous analysis of the teleseismic data recorded by the 41-station seismic array in the Santa Clara Valley (SCV) (*Dolenc et al.*, 2005) showed strong correlations between basin depth reported in the USGS 3D seismic velocity model (ver. 2) (*Jachens et al.*, 1997) and different relative measures of ground motion parameters such as teleseismic arrival delays, P-wave amplitudes, and wave energy. The results suggested that the teleseismic dataset is sensitive to the basin structure and could therefore be used to improve the 3D velocity model.

We used teleseismic waveforms recorded by the SCV seismic array in an inversion to refine the USGS v2 model velocity structure within the SCV basins. To reduce the extremely large model space, we inverted only for the velocity structure within the basins while the basin geometry, as defined in the USGS v2 velocity model, was held fixed. The P- and S-wave velocities, and density in the basins were modeled as laterally uniform and with vertical gradients. The minimum S-wave velocity included in the model was 1 km/s.

2.10.2 Inversion

We followed the approach described by *Aoi* (2002). The observation equation is first linearized and then solved iteratively by singular value decomposition. Synthetic waveforms as well as sensitivity functions are needed to obtain the solution. We used the elastic finite-difference code E3D (*Larsen and Schultz*, 1995) to calculate the waveforms and obtain the sensitivity functions numerically, by taking the difference of waveforms from perturbed and unperturbed models.

The results of the inversion using the waveforms for the M_w=6.4 Near Coast of Central Chile event are shown in Figure 2.21. The top two rows show the first 20 s of the waveforms as only this time window was used in the inversion. The bottom two rows show a 60 s time window. In addition to the P-wave, the pP-wave can be seen arriving just after the first 20 s. The results show that although the waveforms for only the first 20 s were used in the inversion, the final model also better describes the P-wave coda following the pP arrival.

Figure 2.22 compares the velocities in the SCV basins for the USGS v2 model (below station 238), initial, and final model after 3 iterations. Density and density gradient were not free parameters but were determined from P-wave velocity using the Nafe-Drake equation (*Brocher*, 2005).

2.10.3 Conclusions

The results suggest that the velocity structure in the SCV basins is slower than modeled in the USGS v2 velocity model. Additional tests showed that the inversion is stable and the final model is obtained in 3-4 iterations (*Dolenc et al.*, 2007). We started to test a more recent version of the USGS 3D velocity model (SF06) (*Jachens et al.*, 2006). We are also testing the stability of the inversion with additional free parameters that will enable us to model the velocity structure within the basins with a few layers with individual velocity gradients. We will also increase the grid spacing in our modeling to include slower velocities in the shallow parts of the basins.

2.10.4 Acknowledgements

Part of this work was supported by the USGS grants 99HQGR0057 and 00HQGR0048. The Hellman Faculty Fund is acknowledged for partial support.

2.10.5 References

Aoi, S., Boundary shape waveform inversion for estimating the depth of three-dimensional basin structures, *Bull. Seism. Soc. Am. 92*, 2410-2418, 2002.

Brocher, T. M., Empirical relations between elastic wavespeeds and density in the Earths crust, *Bull. Seism. Soc. Am. 95*, 2081-2092, 2005.

Dolenc, D., D. Dreger, and S. Larsen, Basin structure influences on the propagation of teleseismic waves in the Santa Clara Valley, California, *Bull. Seism. Soc. Am. 95*, 1120-1136, 2005.

Dolenc, D., D. Dreger, and S. Larsen, Simultaneous inversion of the teleseismic, local, and microseism observations for the velocity structure within the Santa Clara Valley basins, *Seism. Res. Lett. 78*, 310, 2007.

Jachens, R. C., R. F. Sikora, E. E. Brabb, C. M. Wentworth, T. M. Brocher, M. S. Marlow, and C. W. Roberts, The basement interface: San Francisco Bay area, California, 3-D seismic velocity model, *Eos Trans. AGU, 78*, F436, 1997.

Jachens, R., R. Simpson, R. Graymer, C.Wentworth, and T. Brocher, Three-dimensional geologic map of Northern and Central California: A basin model for supporting earthquake simulations and other predictive modeling. *Seism. Res. Lett. 77*, 270, 2006.

Larsen, S. and C. A. Schultz, ELAS3D: 2D/3D elastic finite-difference wave propagation code, Technical Report No. UCRL-MA-121792, 1995.

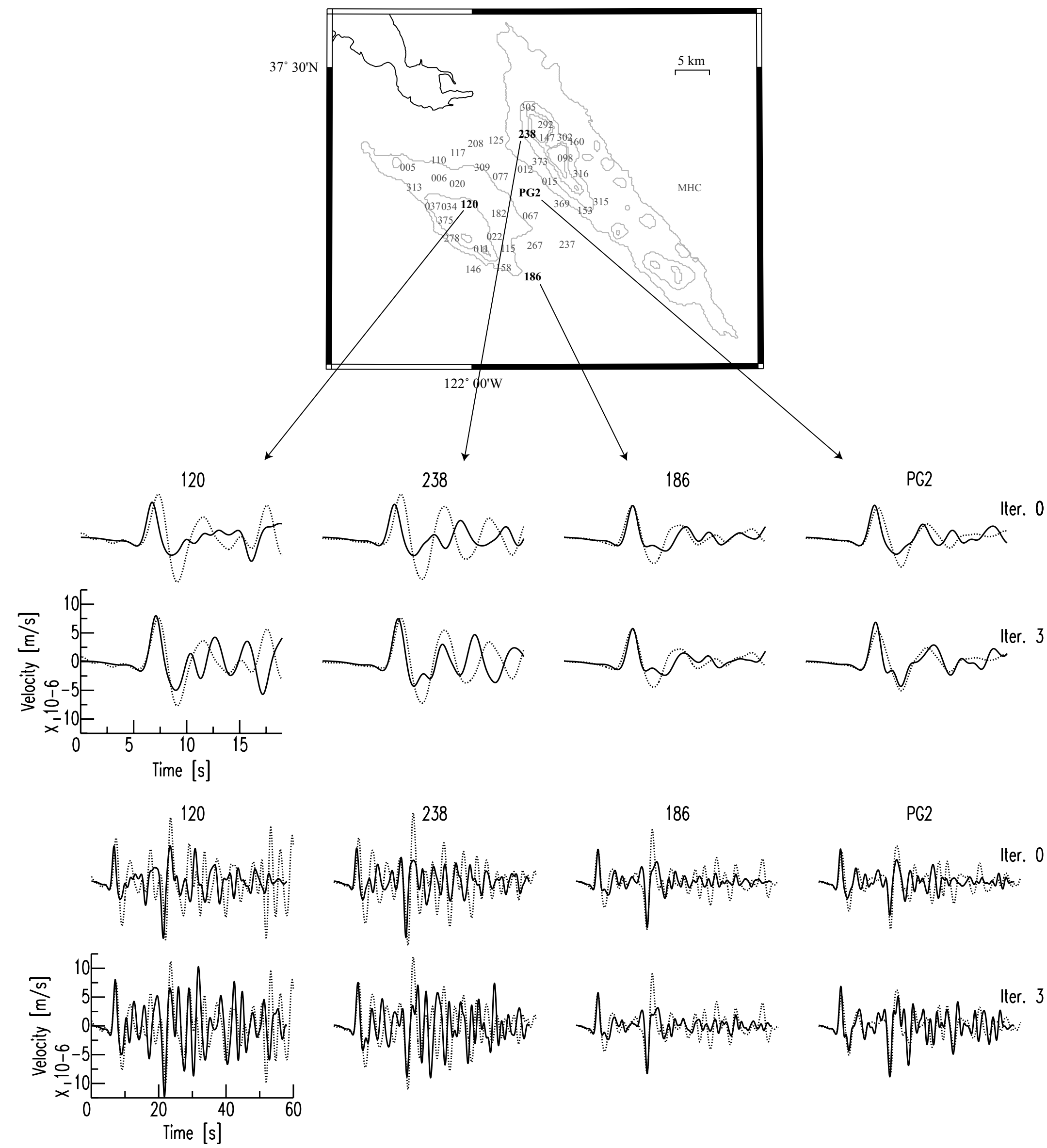

Figure 2.21: Results of the inversion for the M_w=6.4 Near Coast of Central Chile event. Top two rows: The 20 s time window that was used in the inversion. Only four of the 38 stations that were used in the inversion are shown. The observed waveforms are shown for comparison (dotted). Bottom two rows: The longer time window (60 s) shows that final model also better describes the P-wave coda.

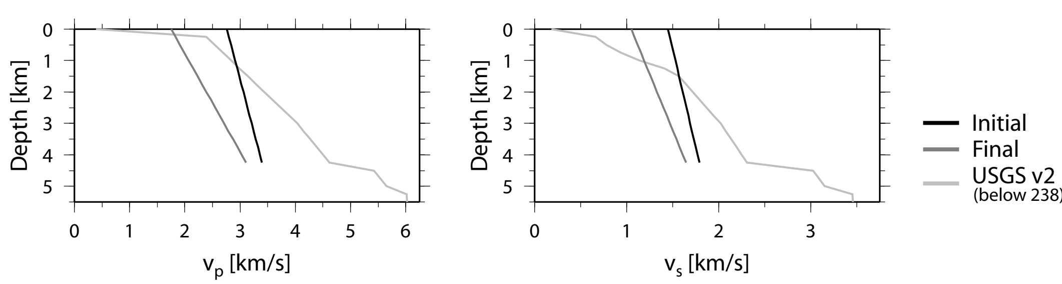

Figure 2.22: Velocities in the SCV basins for the USGS v2 model (below station 238), initial, and final model.

2.11. Observations of Infragravity Waves at the Endeavour Ocean Bottom Broadband Seismic Station (KEBB)

David Dolenc (now at U of Minnesota), Barbara Romanowicz, Paul McGill (MBARI), and William Wilcock (U of Washington)

2.11.1 Introduction

The long-period background noise observed at ocean bottom seismic stations is mainly due to deformation of the seafloor under the pressure forcing by long-period ocean surface gravity waves (infragravity waves; 0.002 to 0.05 Hz). Understanding the nature and characteristics of the coupling between infragravity waves and the solid earth is important for the study of infragravity wave generation and dissipation as well as for the study of the earth's hum and structure using non-seismic sources.

Station KEBB was installed 247 km offshore Vancouver Island at a water depth of 2376 m in August 2003 in collaboration between the University of Washington (UW), the University of Oregon, and the Monterey Bay Aquarium Research Institute (MBARI) as part of a three-year multidisciplinary experiment to monitor the linkages between the seismic deformation and hydrothermal fluxes on the northern Juan de Fuca plate. KEBB comprises a three-component broadband seismometer Guralp CMG-1T, sensitive over a wide frequency range, from 50 Hz to 2.8 mHz (360 sec), a recording, and a battery package. The seismometer is completely buried in the ocean floor sediments. The station is continuously recording data which were retrieved in August 2004 and September 2005.

2.11.2 Infragravity waves

Infragravity waves can be observed at KEBB in the period band from 30 to 400 sec. A comparison of the power spectral density (PSD) at KEBB, MOBB (ocean bottom station in Monterey Bay, CA; *Romanowicz et al.*, 2006), and YBH (land station in northern CA, one of the quietest BDSN stations) is shown in Figure 2.23. KEBB shows a noise hump for periods longer than 30 sec and MOBB for periods longer than 20 sec. The longer short-period cutoff value of the noise hump at KEBB is due to hydrodynamic filtering since KEBB is in deeper water (2376 m) than MOBB (1000 m). The two peaks observed at KEBB between 20 and 30 sec are due to instrumental noise and are present throughout the deployment. The long-period noise on the horizontal component is stronger at KEBB than at MOBB.

When compared to the energy of the short-period ocean waves recorded at local buoys, the low-frequency seismic noise is found to be mainly generated when the short-period ocean waves reach the coast, and not when the storm passes directly above KEBB (Figure 2.24).

Two types of modulation of the infragravity signal are observed at KEBB (*Dolenc et al.*, 2007b). A long-period modulation is best correlated with the energy of the 14-16 sec period ocean waves. The entire infragravity band signal is also modulated in phase with the tides.

2.11.3 Conclusions

Infragravity waves are generated in the nearshore region and are observed at KEBB only after they propagate from the shelf into deeper water and pass over KEBB. This agrees with the previous analysis of the MOBB data which also showed that the infragravity waves are generated in the nearshore region (*Dolenc et al.*, 2005). It sheds some light on the generation of the earth's low frequency "hum" , confirming that coupling of infragravity waves with the solid earth occurs close to the shore (*Rhie and Romanowicz*, 2006). The long-period noise due to infragravity waves is unavoidable in shallow ocean bottom installations and postprocessing is needed to remove it from the seismic observations (*Dolenc et al.*, 2007a).

2.11.4 Acknowledgements

The KEBB deployment was funded by the W. M. Keck Foundation, MBARI, and UW.

2.11.5 References

Dolenc, D., B. Romanowicz, D. Stakes, P. McGill, and D. Neuhauser, Observations of infragravity waves at the Monterey ocean bottom broadband station (MOBB), *Geochem., Geophys., Geosys., 6*, Q09002, doi:10.1029/2005GC000988, 2005.

Dolenc, D., B. Romanowicz, R. Uhrhammer, P. McGill, D. Neuhauser, and D. Stakes, Identifying and removing noise from the Monterey ocean bottom broadband seismic station (MOBB) data, *Geochem. Geophys. Geosys., 8*, Q02005, doi:10.1029/2006GC001403, 2007a.

Dolenc, D., B. Romanowicz, and W. Wilcock, Observations of infragravity waves at the Endeavour ocean bottom broadband station (KEBB), *Seism. Res. Lett., 78*, 261, 2007b.

Romanowicz, B., D. Stakes, D. Dolenc, D. Neuhauser, P. McGill, R. Uhrhammer, and T. Ramirez, The Monterey Bay broadband ocean bottom seismic observatory, *Annals of Geophysics, 49*, 607-623, 2006.

Rhie, J. and B. Romanowicz, A study of the relation between ocean storms and the Earth's hum, G-Cubed, 7, doi:10.1029/2006GC001274, 2006.

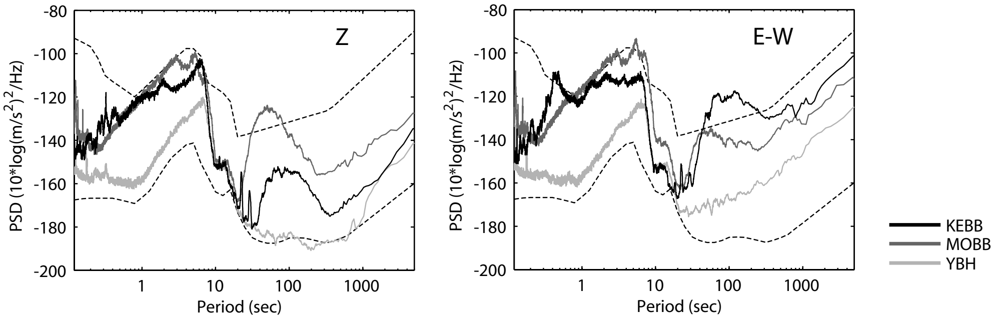

Figure 2.23: PSD at KEBB, MOBB, and YBH for the vertical (left) and horizontal (right) component on a stormy day (10/08/2003). The USGS high- and low-noise models for land stations are shown as dashed lines.

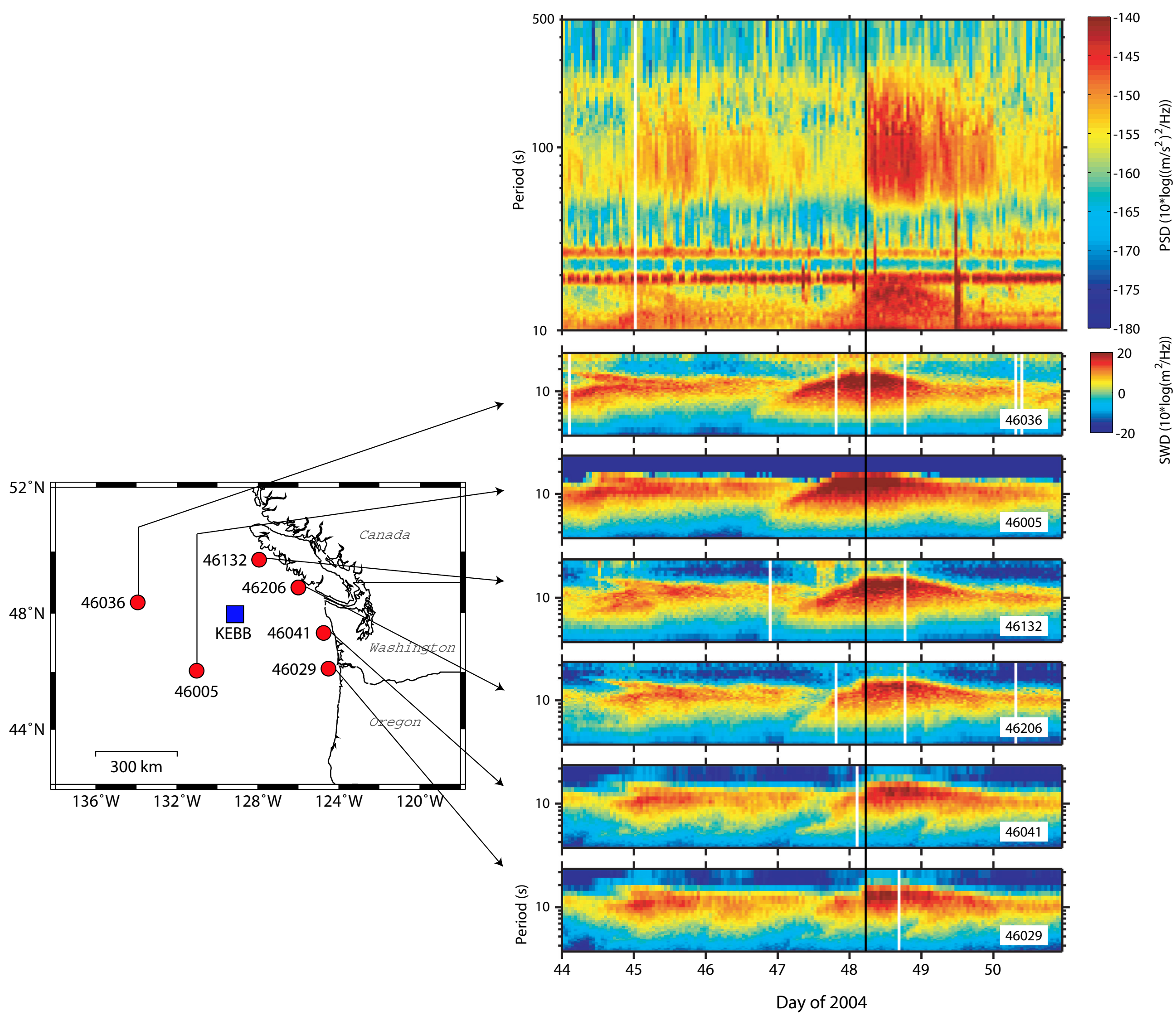

Figure 2.24: Top panel: PSD for the vertical KEBB component as a function of time (7 days) and period (10-500 sec). Bottom 6 panels: The spectral wave density of the ocean waves measured at the buoys. The storm observed on day 48 was approaching from the WSW direction. The change of the infragravity peak width (vertical black line) coincides with the time when the short-period ocean waves reach the coast and not when they pass above KEBB.

2.12. Identifying Isotropic Events Using an Improved Regional Moment Tensor Inversion Technique

Sean R. Ford, Douglas S. Dreger, William R. Walter (Lawrence Livermore National Laboratory)

2.12.1 Introduction

This research seeks to apply a regional distance complete moment tensor approach to tectonic and man-made seismic events in order to document performance in the ability to identify and characterize anomalous (non-double-couple) seismic radiation. Identification of events with demonstrably significant non-double-couple components can aid in discrimination and possibly yield determination (*Given and Mellman*, 1986; *Patton*, 1988; *Dreger and Woods*, 2002). As an initial application we calculate the full moment tensors of 17 nuclear tests at the Nevada Test Site (NTS), three collapses (two mine collapses and one explosion cavity collapse), and 12 earthquakes near the NTS.

We implement the time-domain full regional waveform inversion for the complete moment tensor (2nd rank tensor, M_{ij}) devised by *Minson and Dreger* (2007) after *Herrmann and Hutcheson* (1993) based on the work of *Langston* (1981). Data are collected for a total of 55 stations from the US National Seismic Network, IRIS/USGS, Berkeley Digital Seismic Network, Trinet, and the Lawrence Livermore National Laboratory (LLNL) network. We remove the instrument response, rotate to the great-circle frame, integrate to obtain displacement, and filter similarly to the synthetic seismograms.

2.12.2 Results

It is difficult to grasp the source-type from the standard focal mechanism plot. And decompositions of the deviatoric component are non-unique, where the DC and CLVD decomposition followed here could be replaced by two DCs (*Julian et al.*, 1998). Following the source-type analysis described in *Hudson et al.* (1989) we calculate -2ϵ and k, which are given by

$$\epsilon = \frac{-\hat{m}_1}{|\hat{m}_3|}$$

and

$$k = \frac{M_{ISO}}{|M_{ISO}| + |\hat{m}_3|}$$

where $\hat{m}_1$, $\hat{m}_2$ and $\hat{m}_3$ are the deviatoric principal moments for the T, N, and P axes, respectively, and M_{ISO} is the isotropic moment where $M_{ISO} = \mathrm{trace}(M_{ij})/3$. ϵ is a measure of the departure of the deviatoric component from a pure double-couple mechanism, and is 0 for a pure double-couple and ±0.5 for a pure CLVD. k is a measure of the volume change, where $+1$ would be a full explosion and -1 a full implosion. We calculate the source-type plot parameters for 12 earthquakes, 17 explosions and three collapses (one cavity and two mine) and produce the source-type plot (Figure 2.25). The nuclear tests occupy the region where $k > 0.25$, the earthquakes cluster near the origin (with some interesting deviations), and the collapses plot almost exactly at (1,-5/9), which is the location for a closing crack in a Poisson solid. The populations of earthquakes, explosions, and collapses separate in the source-type plot. These initial results are very encouraging and suggest a discriminant that employs the k, -2ϵ parameters.

2.12.3 Acknowledgements

Sponsored by the National Nuclear Security Administration, Office of Nonproliferation Research and Development, Office of Defense, Nuclear Nonproliferation. Contract No. DE-FC52-06NA27324. We thank Jeff Stevens for discussions regarding vanishing tractions at the free surface, Howard Patton for insights on the CLVD contribution to the explosion source, and Bruce Julian for the code to make the source-type plots. Figures were made with Generic Mapping Tools (*Wessel and Smith*, 1998).

2.12.4 References

Dreger, D. and B. Woods (2002). Regional distance seismic moment tensors of nuclear explosions; seismic source mechanism through moment tensors, *Tectonophysics, 356* (1-3), 139-156.

Given, J. W. and G.R. Mellman (1986). Estimating explosion and tectonic release source parameters of underground nuclear explosions from Rayleigh and Love wave observations, Tech. rep., Sierra Geophysics Report No. SGI-R-86-126, Kirkland, WA.

Herrmann, R. B. and K. Hutchensen (1993). Quantification of MLg for small explosion, Tech. rep., Phillips Laboratory Report PL-TR-93-2070.

Hudson, J. A., R. G. Pearce, R. G., and R. M. Rogers (1989). Source type plot for inversion of the moment tensor, *J. Geophys. Res., 9* (B1), 765-774.

Julian, B. R., A. D. Miller and G. R. Foulger (1998). Non-double-couple earthquakes; 1. Theory, Rev. *Geophysics, 36* (4), 525- 549.

Langston, C. A. (1981). Source inversion of seismic waveforms; the Koyna, India, earthquakes of 13 September 1967, *Bull. Seis. Soc. Amer., 71* (1), 1-24.

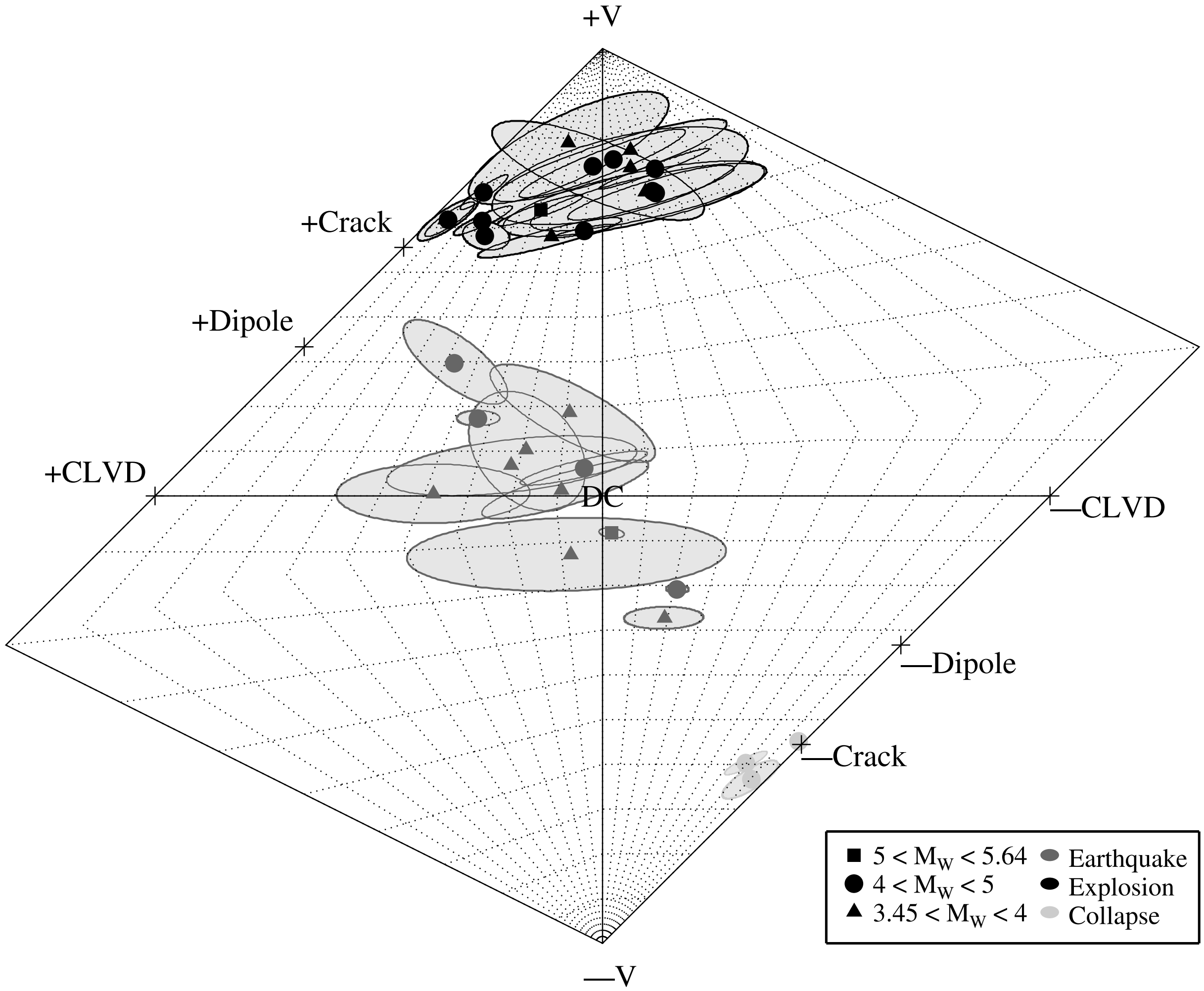

Figure 2.25: Source-type plot of the 12 earthquakes (blue), 17 explosions (red), 3 collapses (green), and their associated 95% confidence regions (shaded) analyzed in this study. The magnitude of the event is given by the symbol. The abscissa measures the amount of volume change for the source and the ordinate measures the departure from a pure DC.

Minson, S. and D. Dreger (2007). Improved seismic moment tensor inversion, submitted to *Geophys J. Int.*

Muller, G. (1973). Seismic moment and long-period radiation of underground nuclear explosions, *Bull. Seis. Soc. Amer., 63* (3), 847-857.

Panning, M., D. Dreger and H. Tkalcic (2001). Near-source velocity structure and isotropic moment tensors; a case study of the long valley caldera, *Geophys. Res. Lett., 28* (9), 1815-1818.

Patton, H. J. (1988). Source models of the Harzer explosion from regional observations of fundamental-mode and higher mode surface waves, *Bull. Seis. Soc. Amer., 78* (3), 1133-1157.

Saikia, C. K. (1994). Modified frequency-wavenumber algorithm for regional seismograms using Filon's quadrature; modelling of Lg waves in Eastern North America, *Geophys. J. Int., 118* (1), 142-158.

Sileny, J. (2004). Regional moment tensor uncertainty due to mismodeling of the crust, *Tectonophysics, 383* (3-4), 133-147.

Sileny, J. and V. Vavrycuk (2002). Can unbiased source be retrieved from anisotropic waveforms by using an isotropic model of the medium?; Seismic source mechanism through moment tensors, *Tectonophysics, 356* (1-3), 125-138.

Song, X. J., D. V. Helmberger and L. Zhao (1996). Broad-band modelling of regional seismograms; the basin and range crustal structure, *Geophys. J. Int., 125* (1), 15-29.

Wessel, P., and W. H. F. Smith (1998). New, improved version of generic mapping tools released, in American Geophysical Union, San Francisco, Vol. 79, 579.

2.13. Recalibrating M_L for CISN

Robert Uhrhammer, Margaret Hellweg, Pete Lombard, Kate Hutton (Caltech), Egill Hauksson (Caltech), Allan Walter (USGS Pasadena), Dave Oppenheimer (USGS Menlo Park)

2.13.1 Research Objectives

Richter (1935) and *Gutenberg and Richter* (1942) developed the local magnitude scale using Wood-Anderson seismographs. *Richter* (1935) defined "local" magnitude as:

$M_L = \log A - \log A_o(\Delta) + dM_L$

where: M_L is the local magnitude estimate; $\log A$ is the logarithm of the maximum trace amplitude A (in mm) recorded by a standard Wood-Anderson torsion seismograph; $\log A_o(\Delta)$ is the logarithm of a standard event of magnitude zero at the same epicentral distance Δ in km; and, dM_L is the station adjustment. The M_L estimate for an event is then the arithmetic average of the individual estimates from the Wood-Anderson seismographs that recorded the event.

In the past thirty years, the instrumentation with which we measure earthquakes has changed, and we can now process the data digitally. Nonetheless, we would like to continue to assign events with local magnitudes which are consistent with those that have been calculated in Northern and Southern California for the past 75 years.

2.13.2 Data Set

Initially, a set of approximately 100,000 waveforms from 255 candidate earthquakes recorded by 1160 horizontal channels (Station-Network-Channel-Location, or SNCL labels are used to describe each) from the AZ, BK, CI and NC networks were extracted. The candidate events were selected from the CISN 2000-2006 seismicity catalog by gridding the state into 50km square bins and selecting the largest M_L 3+ event that occurred in each bin, and also (to obtain an adequate USArray data set) the largest M_L 3+ event in 2006 (or second largest if the largest 2000-2006 event event in the bin occurred in 2006). The SNCL channels included both broadband and strong motion instruments.

Local magnitude (M_L) was calculated from each channel's trace by deconvolving the instrument response and convolving the response of a Wood-Anderson seismograph (*Uhrhammer et al*, 1996). For each event, differences for all SNCL pairs were calculated, giving a dataset with more than 10 million differential observations. These differences were simultaneously inverted to determine a station adjustment for each SNCL, dM_L(SNCL), and a function describing the amplitude decay as a function of distance, called $\log A_o$.

2.13.3 Approach

Following a sequence of exploratory inversions, the data set was culled to remove events and SNCL's with fewer than 7 data each and to also remove data with event-SNCL distances greater than 500 km. The remaining differential data were then inverted simultaneously, via constrained linear least-squares, to determine the perturbations to the amplitude decay function ($\log A_o$) and the adjustment (dM_L) for each SNCL with the constraints: (1) $\log A_o(100km)$ = -3; and (2) the sum of the dM_Ls for selected SNCLs with historical dM_L values = the sum of their historical dM_L values. This approach was taken to ensure consistency with past magnitudes determined in Northern and Southern California.

2.13.4 Amplitude Attenuation Function

The constrained linear least-squares perturbations to the $\log A_o$ function were found to be very stable and well represented by a sixth order Chebyshev polynomial at hypocentral distances from 8 km to 500 km. At shorter distances, it is approximated by a line with a slope close to 2. In this study, we use hypocentral distance, rather than epicentral distance as originally used by *Richter* (1935), to accurately represent variation in the $\log A_o$ attenuation function at close distances. This $\log A_o$ form was adopted and a CISN $\log A_o$ algorithm was developed and used in all subsequent inversions for the dM_L SNCL adjustments. A plot of the CISN $\log A_o$ function is shown in Figure 2.26.

2.13.5 SNCL dM_L

Following another sequence of exploratory inversions, the data set was further culled to include only broadband data SNCLs. The final inversion used data from 217 earthquakes which occurred throughout California for 560 broadband horizontal channels from the AZ, BK, CI and NC networks. For each event, differences in M_L for all SNCL pairs were calculated, giving a dataset with 2607484 observations. These differences were simultaneously inverted to determine the dM_L station adjustment for each SNCL with the constraint: dM_L(PAS.E) + dM_L(PAS.N) + dM_L(BAR.N) + dM_L(MWC.E) + dM_L(MWC.N) + dM_L(PLM.E) + dM_L(PLM.N) + dM_L(RVR.E) + dM_L(RVR.N) + 1.5 * (dM_L(BKS.E) + dM_L(BKS.N) + dM_L(BRK.N) + dM_L(BRK.E) + dM_L(MHC.N) + dM_L(MHC.E)) = +0.943 (the sum of the historical dM_L values at these stations). The 1.5 multiplier is used to equalize the weight-

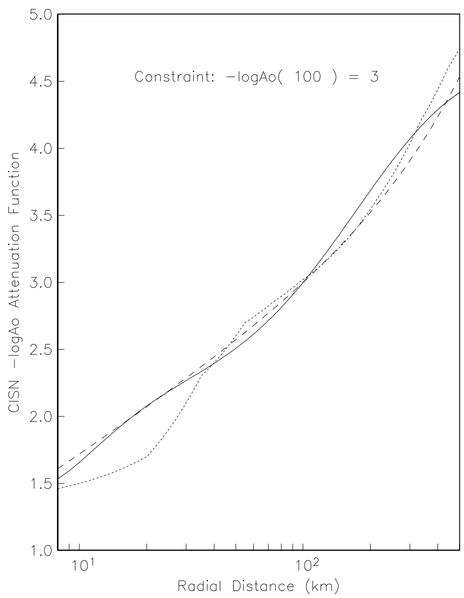

Figure 2.26: Comparison of the new CISN $-logA_o$ attenuation function (solid line) with those used in Northern California (short dashed line, *Richter*, 1935) and in Southern California (long dashed line, *Kanamori et al*, 1999). Note that distance is given from the hypocenter and not from the epicenter.

ing of the 6 BK SNCLs and the 9 CI SNCLs. A map of the CISN SNCL dM_L adjustments is shown in Figure 2.27.

Significance of Findings

The state-wide $\log A_o$ and station corrections for determining magnitudes will improve reporting for earthquakes in all of California on several counts. First, M_L was being calculated using only a subset of the currently existing broadband stations in both Northern and Southern California, as only they had been calibrated. In the past 10 years, many broadband stations and strong motion stations have been added to the networks. With the additional stations, M_L determination should become much more reliable. Second, until now Northern (*Uhrhammer et al*, 1996) and Southern California (*Kanamori et al*, 1999) have been using different $\log A_o$ functions, with their attendant dM_L values for each SNCL. Thus different magnitudes were often determined by Northern or Southern California for an earthquake if it was near the boundary of the reporting regions, or for very large earthquakes in the other region. When the results of this project are implemented in the realtime and event review systems, this should no longer be the case.

2.13.6 Acknowledgements

Work on this project has been supported by the CISN funding of the California Governor's Office of Emergency Services under contract 6023-5 and the United States Geological Survey project 07HQAG0013.

2.13.7 References

Richter, C.F., An instrumental earthquake magnitude scale, *Bull. Seismol. Soc. Am.*, *25*, 1-32, 1935.

Gutenberg, B. and Richter, C. F, Earthquake magnitude, intensity, energy and acceleration, *Bull. Seismol. Soc. Am.*, *32*, 163-192, 1942.

Uhrhammer, R., Loper. S. J., Romanowicz, B., Determination of local magnitude using BDSN broadband records *Bull. Seismol. Soc. Am.*, *86*, 1314-1330, 1996.

Kanamori, H., Maechling, P., Hauksson, E., Continuous Monitoring of Ground-Motion Parameters *Bull. Seismol. Soc. Am.*, *89*, 311-316, 1999.

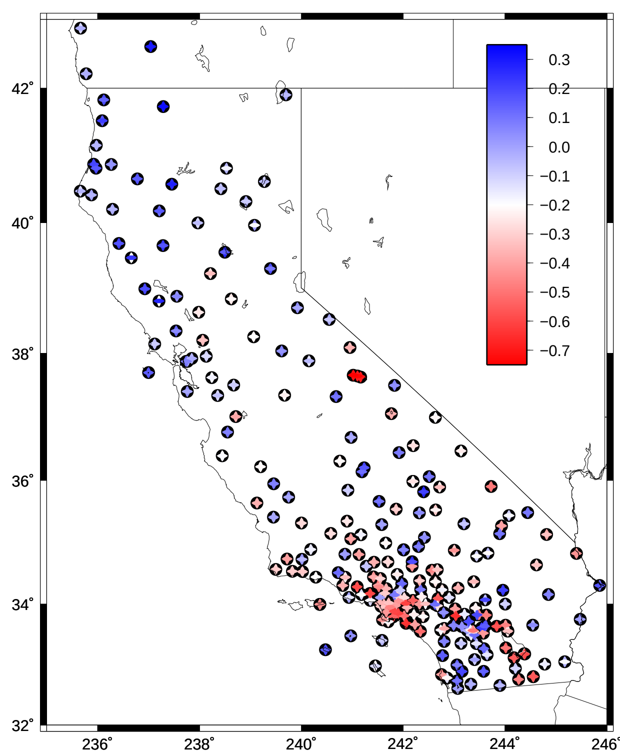

Figure 2.27: CISN dM_L adjustments for broadband stations in Northern and Southern California.

2.14. The Orinda Events: Complexity in Small Events

Margaret Hellweg

2.14.1 Introduction

Are small earthquakes like large earthquakes? Does their faulting involve the same physics? How small do aftershocks get, and where do they occur? Do they exhibit similar complexity to that observed in large events? These questions are difficult to answer, because small earthquakes and their tiny aftershocks are rare in our recordings.

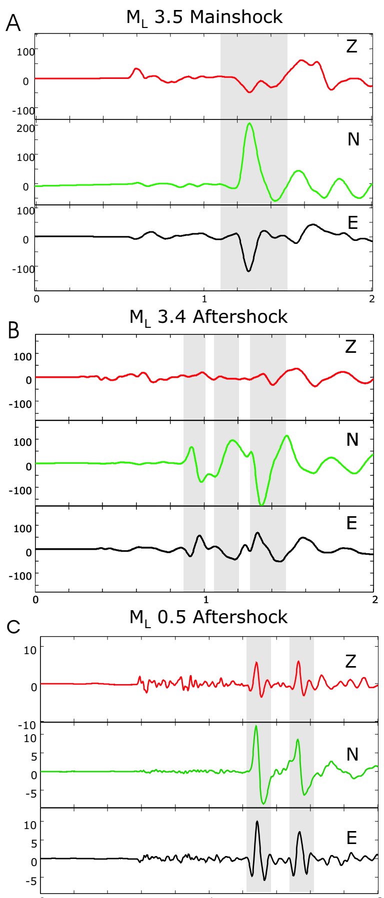

Figure 2.28: Example waveforms of (A) the mainshock, which is simple, and (B) the largest and (C) a small aftershock, which are complex. This is most easily seen in the S-waves (gray shading), which have more than one large arrival om B amd C.

A sequence of small earthquakes near Orinda, California, occurred almost under the BSL's station BRIB (37.92 N, 122.15 W). At the surface, this station has a broadband seismometer and an accelerometer. As it is also a borehole station of the Northern Hayward Fault network, it has a geophone and an accelerometer, each with 3-components, at a depth of 119 m. The borehole instruments are sampled at 500 sps. The sequence began on October 19, 2003, at 14:35:27 UTC, with an earthquake with M_d 2.5. The mainshock (MS, M_L 3.5, Figure 2.28A) followed about an hour later. Over the course of the next 3 months, there were more than 4000 aftershocks, with magnitudes ranging from -2.5 to 3.4.

2.14.2 Event Complexity

Most events in the Orinda sequence, like the MS, have classically simple waveforms, a single P pulse followed by a single S pulse (Figure 2.28A). However, many earthquakes of all sizes exhibit one of two types of complexity. In one type, several events of similar size occur within a very short interval, as a sort of "rapid-fire" burst (*Hill et al*, 1990, *Asch et al*, 1997). In the second type of complexity, more than one P-wave pulse arrives before the first S-wave (Figure 2.28 B, C). Using measurements from waveforms of a few events, we estimate the source location of the P-pulse of each subevent from its polarization (*Plesinger et al*, 1986, *Abercrombie*, 1995) and its t_{s-p}.

As with the other events of the sequence, t_{s-p} values for the subevents lie between 0.58 and 0.7 s, and they are located within the cluster. Figure 2.29A shows as an example the locations of three subevents from the event in Figure 2.28B (P1, P2 and P3) and two subevents from the event in Figure 2.28C (Pa and Pb) in relationship to the mainshock (MS), the M_d 2.5 foreshock (FS) and several aftershocks (small dots), as well as to the station BRIB. The distances are given in km. The table (Figure 2.29B) gives the spatial separation of the subevents and the intervals between them. It also gives the ratio of the subevent spacing to the values of v_P (4.1 km/s) and v_S (2.3 km/s) assumed for the source volume. The intervals between the subevents are consistent with the propagation of rupture at speeds around 0.8 v_S.

2.14.3 Summary and Perspectives

Although the earthquakes of the Orinda sequence are small, their study contributes to understanding and defining earthquake hazard in Northern California. They occurred in an otherwise seismically quiet region of the Bay Area, between the Hayward and Calaveras faults. The only previous recent seismicity in the area occurred as a brief sequence in 1977 (*Bolt et al*, 1977). Thus, this sequence offers the opportunity to learn more about the seismicity and seismic hazard between the two faults. In addition, the many aftershocks provide data for improving the velocity structures between these two major faults, particularly at shallow levels. Cursory comparisons between the Orinda and other nearby sequences with similarly sized mainshocks suggest that the Orinda sequence has produced many more aftershocks. Learning more about the physics at these earthquakes' sources will help understand why this is true.

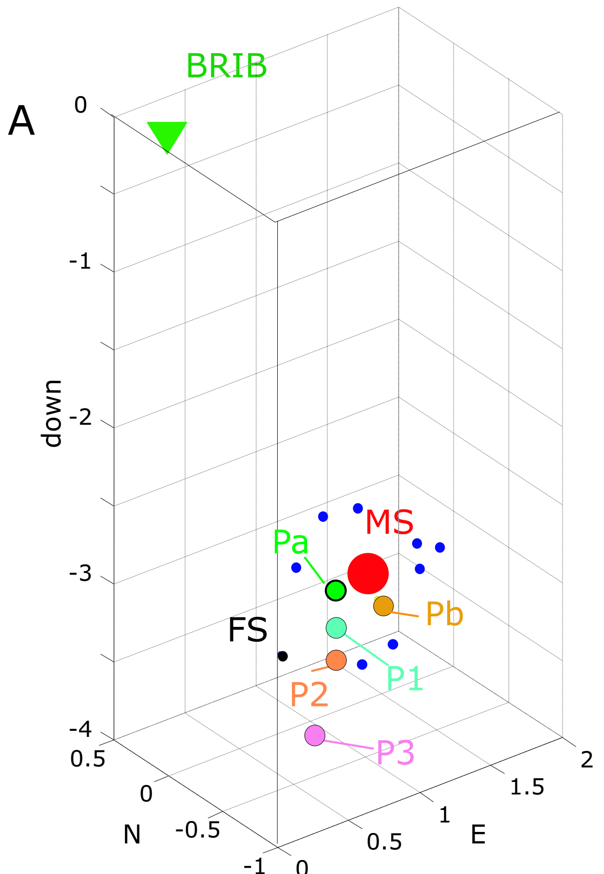

B

Subevent-Pair	Δt_P [s]	δ [km]	δ/v_P [s]	δ/v_S [s]	$(\delta/v_S)/\Delta t_P$
P2-P1	0.092	0.195	0.048	0.085	0.92
P3-P2	0.259	0.465	0.113	0.202	0.78
Pb-Pa	0.25	0.363	0.089	0.158	0.63

Figure 2.29: Locations (from P-wave polarization and t_{s-p}) of the M_L 2.5 foreshock (FS), the mainshock (MS) and the P-wave pulses of the largest aftershock (P1, P2, P3) and a small aftershock exhibiting complexity (Pa, Pb).

2.14.4 References

Abercrombie, R.E., Earthquake locations using single-station deep borehole recordings: Implications for microseismicity on the San Andreas fault in southern California. *J. Geophys. Res.*, *100*, 24003-24014, 1995.

Asch, G., K. Wylegalla, M. Hellweg, D. Seidl, and H. Rademacher, Observations of Rapid-Fire Event Tremor at Lascar Volcano, Chile, *Annali di Geofisica*, *39*, p. 273-282, 1996.

Bolt, B., J. Stifler and R. Uhrhammer. The Briones Hills Earthquake Swarm of January 8, 1977, Contra Costa County, California. *Bull Seismol. Soc. Am.*, *67*, 1555-1564, 1977.

Hill, D.P., W.L. Ellsworth, M.J.S. Johnston, J.O. Langbein, D.H. Oppenheimer, A.M. Pitt, P.A. Reasenbert, J.L. Sorey and S.R. McNutt, The 1989 Earthquake Swarm Beneath Mammoth Mountain, California, An Initial Look at the 4 May through 30 September Activity, *Bull. Seis. Soc. Am.*, *80*, 325-339, 1990.

Plesinger, A., M. Hellweg and D. Seidl, Interactive high-resolution polarization analysis of broadband seismograms. *J. Geophysics*, *59*, p. 129-139, 1986.

2.15. Using 1906 Simulations to Assess Performance of Northern California Networks

Margaret Hellweg, Peter Lombard, John Boatwright (USGS), Howard Bundock (USGS), Hamid Haddadi (CGS)

2.15.1 Introduction

Emergency responders depend on real time data products such as earthquakes' locations and their magnitudes. ShakeMaps (*Wald et al* 1996) are also critical tools for estimating the impact of large and great earthquakes on society. These products can only be as reliable as the seismic systems which record and transmit ground shaking. We test the real time ShakeMap capabilities of the seismic networks in Northern California Seismic System (NCSS) (USGS Menlo Park, network code: NC; UC Berkeley, network code BK; the California Geological Survey, network code CE; USGS Strong Motion Program, network code NP). These networks have a large number of freefield strong motion stations; however, only about 160 of them, mostly in the San Francisco Bay Area, report data in real time. Thus only these stations can contribute to initially produced ShakeMaps.

2.15.2 ShakeMap Scenarios

Boatwright and Bundock (2005) produced a new Modified Mercalli intensity map in the form of a ShakeMap for the 1906 San Francisco earthquake reviewing all intensities reported in the Lawson report (*Lawson et al*, 1908; Figure 2.30A). We use this as a reference for the quake's actual ground motion to compare with ShakeMaps produced using subsets of the real time strong motion stations in Northern California from the BK, NC and NP networks. Ground motion for each site is taken from *Graves* (2006) synthetic ground motions for a 1906-type event (M_w 7.8, epicenter 2 mi W of San Francisco, rupture from San Jose to Cape Mendocino) and fed into ShakeMap.

Figure 2.30B shows the ShakeMap which would result if all 160 real time stations in the NCSS were able to transmit their data reliably to the datacenter where the ShakeMap is produced. Two things stand out in comparison with Figure 2.30A: The high level of ground shaking around the Bay Area and the extremely low estimate of shaking along the northern segment of the San Andreas Fault, where there are few stations. The latter factor can be somewhat alleviated by introducing the extent of fault rupture (Figure 2.30C). This information may be available within an hour of the quake, either from finite fault inversions or from the distribution of aftershocks. The estimated relatively slow decay of ground motion with distance from the fault is caused by the attenuation relationship currently used in ShakeMap (*Boore et al*, 1997).

Figure 2.30B may be considered a "best case scenario", with all real time stations reporting. The 1906 earthquake produced strong shaking. If the data center at the USGS Menlo Park were incapacitated, no data from the NC and NP networks would be available. In this case, the only data to constrain the initial ShakeMap would come from the 27 BK strong motion sites (Figure 2.30D).

2.15.3 Conclusions

We simulate the performance of the Northern California Seismic System (networks NC, NP and BK) of the California Integrated Seismic Network for the case of a repeat of the 1906 earthquake to assess its ability to produce reliable ShakeMaps. Among the many factors that influence the robustness of the system are reliability of telemetry from individual stations and nodes, as well as of the data center. Even with the correct location and magnitude for the earthquake and with all 160 real time strong motion instruments reporting ground motions, it is still critical to estimate the fault length to produce a usable ShakeMap.

2.15.4 References

Boatwright, J. and H. Bundock, Modified Mercalli intensity maps for the 1906 San Francisco earthquake plotted in ShakeMap format. *USGS Open-File Report*, *OF 2005-1135*, 2005.

Boore, D. M., W. B. Joyner, and T.E. Fumal, Equations for Estimating Horizontal Response Spectra and Peak Accelerations from Western North American Earthquakes: A Summary of Recent Work, *Seism. Res. Lett.*, *68*, 128-153, 1997.

Graves, R., Broadband Ground Motion Simulations for Earthquakes in the San Francisco Bay Region, *Seismol. Res. Lett.*, *77*, 275, 2006.

Lawson, A., G. K. Gilbert, H. F. Reid, J. C. Branner, H.W. Fairbanks, H. O. Wood, J. F. Hayford and A. L. Baldwin, The California Earthquake of April 18, 1906: Report of the State Earthuake Investigation Commission, 1908.

Wald, D. J., V. Quitoriano, T. H. Heaton, H. Kanamori, C. W. Scrivner, and C. B. Worden, TriNet ShakeMaps: Rapid Generation of Instrumental Ground Motion and Intensity Maps for Earthquakes in Southern California, *Earthquake Spectra*, *15*, 537-556, 1996

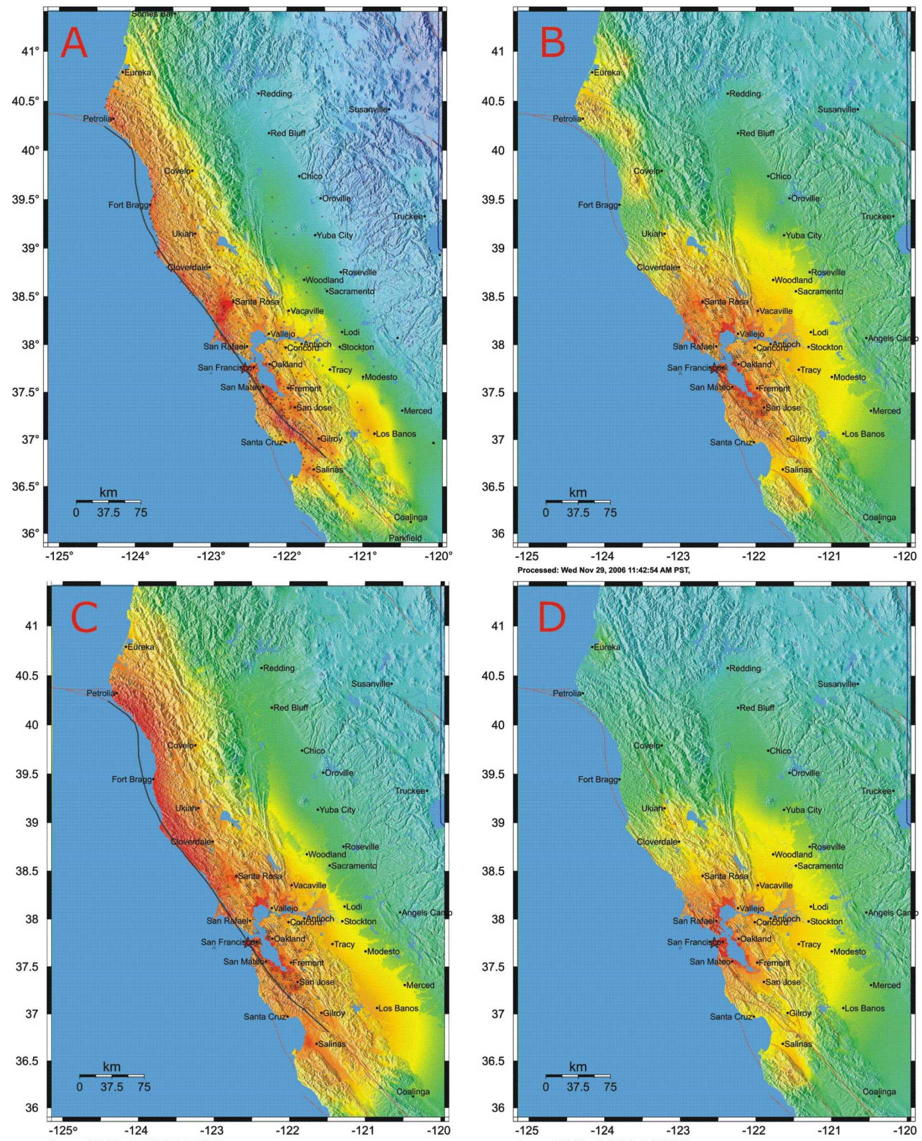

PERCEIVED SHAKING	Not felt	Weak	Light	Moderate	Strong	Very strong	Severe	Violent	Extreme
POTENTIAL DAMAGE	none	none	none	Very light	Light	Moderate	Moderate/Heavy	Heavy	Very Heavy
PEAK ACC.(%g)	***<.17***	***.17-1.4***	***1.4-3.9***	***3.9-9.2***	***9.2-18***	18-34	34-65	65-124	>124
PEAK VEL.(cm/s)	<0.1	0.1-1.1	1.1-3.4	3.4-8.1	8.1-16	***16-31***	***31-60***	***60-116***	***>116***
INSTRUMENTAL INTENSITY	I	II-III	IV	V	VI	VII	VIII	IX	X+

Figure 2.30: *Boatwright and Bundock* (2005) ShakeMap (A) and scenario ShakeMaps for assessing network performance (B-D). (A) The ShakeMap compiled by *Boatwright and Bundock* (2005) from the Lawson report (1908) provides a baseline against which to assess the initial ShakeMaps which would be computed from ground motion measured in a similar earthquake, if it were to occur today. (B) ShakeMap for 160 real time stations in Northern California from the BK, NC and NP networks. The initial ShakeMap would be ready within 10 minutes after an earthquake occurs. The hypocenter and magnitude are assumed to be the same as in 1906, however the length of the fault rupture is not known. (C) For this ShakeMap the same data is used as for (B), but in addition to hypocenter and magnitude, the extent of fault rupture is also used. Strong shaking is now also predicted along the Coast. (D) Maps (B) and (C) represent best cases for real time reporting. If telemetry to and from USGS Menlo Park is interrupted, ShakeMaps from UC Berkeley would be based only on the 27 stations of the sparse BK network.

2.16. Scanning of Unusual Seismicity in the Mendocino Triple Junction Region

Aurélie Guilhem, Douglas S. Dreger, and Robert M. Nadeau

2.16.1 Introduction

Anomalous seismic activity with wide-ranging behavior has been detected in the vicinity of the Mendocino Triple Junction (MTJ) and offshore transform faults. Among those unusual earthquakes are non-volcanic tremors, repeating earthquakes and slow-rupture or low-stress-drop earthquakes. These unusual events, together with 'typical' earthquakes, provide clues regarding the mechanics of faulting in the offshore region. One difficulty in the study of seismicity of the region is that the events located far offshore may go undetected or they may have poor locations with large uncertainty. Another difficulty is that there is a class of events that have either low stress drop or have slow rupture processes that make typical detection difficult. We present here preliminary results of a low-frequency continuous waveform scanning method to detect and locate events in the offshore region as well as compute the seismic moment tensor.

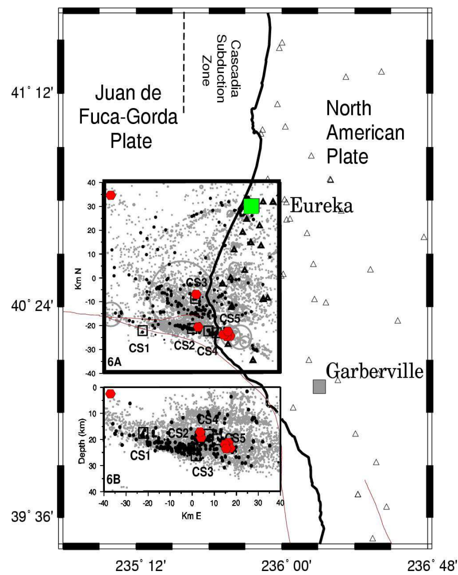

Figure 2.31: Map of the unusual seismic activity in Mendocino region. The green square is a BDSN station (JCC), the triangles are NCSN stations. Seismicity (gray points) has been relocated with hypoDD using the NCSN stations. Red circles are few slow earthquakes and small black circles show repeating earthquake seismicity.

2.16.2 Unusual seismic events in Mendocino area

The Mendocino Triple Junction is a structurally and seismically complex region where the North American, the Pacific and the Juan de Fuca-Gorda plates intersect. The triple junction at Mendocino is the junction of the northern part of the San Andreas fault, the Cascadia subduction zone and the Mendocino Transform fault. Several unusual seismic events have been recorded in this area, including non-volcanic tremors, repeating earthquakes and slow/low-stress-drop earthquakes (Figure 2.31).

Thus far we have concentrated our efforts on the slow earthquakes or low-stress-drop earthquakes. This class of events is identified by a large discrepancy ($\geq$0.5) between the moment magnitude M_w and the local magnitude M_L, where M_w is larger. Based on the Berkeley Moment Tensor catalog, at least 18 slow earthquakes have occurred and have been recorded between 1992 to the present with a M_w range between 4.0 and 6.8. Smaller slow earthquakes may have occurred, but they have not been detected. Analyses show that some of the slow earthquakes have stress drops of 0.4 bar when the stress drop for a normal earthquake is between 10 and 100 bars. Whereas the corner frequency of a $M_L \approx M_w \approx 4$ earthquake is about 2Hz, for a slow event (M_L=4 and M_w=5) the corner frequency is on the order of 0.1Hz, which is more appropriate for a M_w6.5+ event.

A catalog of relocated events shows a sequence of four low-stress-drop earthquakes which occurred in 1997 and 1999. All have a very similar location in latitude and longitude, but their depth varies in a range of 4 km. Because they are located at the same place on the Mendocino transform fault and also because they have about the same moment magnitude, these four events may appear as potential repeating slow-earthquakes.

Using a cross-correlation analysis with two of these four events as references, we have scanned about 6 years, between 2000 and the end of 2006, of continuous broadband data recorded at four stations of the Berkeley network (ORV, MOD, WDC and YBH) and filtered between 0.02 and 0.05 Hz. We run the cross-correlation analysis for the three components at each station and we study all the hits giving at least 60% of similarities with the references and seen at, at least, 3 stations.

We obtained a large number of hits due to large teleseisms. Because of the large S-P arrival time of the teleseisms, a positive result in the cross-correlation occurred for either the P-waves or S-waves. With this method, we have not detected any additional slow earthquakes in the

Mendocino transform fault that we did not know about. This result may also be due to the choice made in the references.

2.16.3 Detection, localization and moment tensor solution for an offshore slow earthquake

Previous studies (*Dreger et al.*, 1998 and *Tajima et al.*, 2002) have investigated the capability of a sparse broadband network, the Berkeley Digital Seismic Network (BDSN), at monitoring a region located outside the network, and tested the feasibility of a new automated moment-tensor determination system that continuously monitors seismic waveforms from the same network.

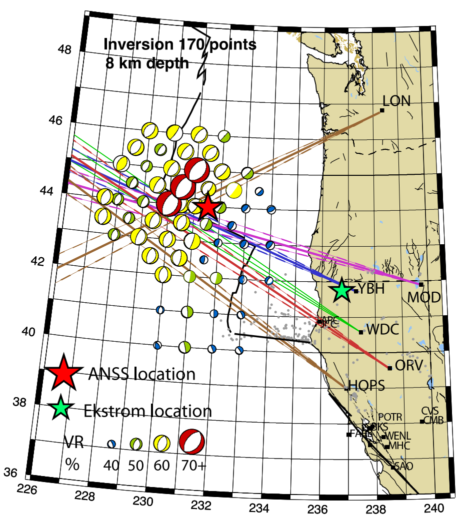

Figure 2.32: Low-frequency study of an offshore slow earthquake. Association of azimuthal rotation and seismic moment tensor grid search in the localization of an unusual event. The lines indicated the rotation axes plus or minus 3 degrees for each station.

Before using the moment and scanning method for events in Mendocino Triple Junction region, we need to test its feasibility for a recorded slow-earthquake. We have decided to apply it to a slow/low-stress drop event in December 2000 extracted from Goran Ekström's catalog. Ekström analysed and located it onshore in Northern California (Figure 2.32). However a first triangulation analysis of seismic records between 0.02 and 0.05 Hz from a few stations of the BDSN network (YBH, MOD, WDC, ARC and ORV) has given an offshore location. Despite the difficulty of identifying the body waves, analyses of P and Rayleigh wave particle motion have been done and were used in order to determine the azimuth between the seismic stations and the event. Such an azimuthal analysis has confirmed an offshore location (lines from seismic stations on Figure 2.32).

However, the uncertainty on location that we obtained is relatively large and depends on the quality of the stations used. We have completed our research by a grid search analysis of the seismic moment tensors using ORV, MOD, WDC and YBH to quantitatively locate the earthquake using the variance reductions from the computation. By this frequency waveform scanning and moment tensor grid search we are able to define a smaller area for the location of the event around the ridge segment between the Pacific and Gorda plates. Finally, the ANSS catalog location is similar to our location using this method, suggesting the potential success of a low-frequency continuous waveform scanning in locating events in the offshore region, as well as computing the seismic moment tensor. We also have to mention here that the moment tensor solutions indicate a high CLVD component with a normal mechanism which could be consistent with an explosion on the ridge segment. The ANSS catalog gives a M_b 4.7 and a M_s 3.9. With our method we have found a M_w between 4.4 and 4.5 for the best moment tensor solutions.

With the goal of better constraining the location and mechanism of the offshore events, it would be important to consider a better coverage of broadband stations in the future. In the case of the earthquake in 2000, very few broadband stations were continuously recording. Some part of the analysis has considered the records at a station in Washington state, LON station (Figure 2.32). Today, many more high quality stations are operating in many places along the coast and can be easily used.

2.16.4 Conclusion

We plan to implement the low-frequency continuous moment tensor scanning method in the Mendocino region. Such a method would improve the response time for rapid characterization of earthquake sources and tsunami hazard from offshore events.

2.16.5 Acknowledgements

Part of this work is supported by the National Science Foundation (NSF) grant NSF-EAR-0537641.

2.16.6 References

Dreger, D.S., R. Uhrhammer, M. Pasyanos, J. Franck, and B. Romanowicz (1998), Regional and Far-Regional Earthquake Locations and Source Parameters Using Sparse Broadband Networks: A test on the Ridgecrest Sequence, *Bulletin of the Seismological Society of America*, vol. 88, 6, 1353–1362.

Tajima, F., C. Megnin, D.S. Dreger, and B. Romanowicz (2002), Feasibility of Real-Time Broadband Waveform Inversion for Simultaneous Moment Tensor and Centroid Location Determination, *Bulletin of the Seismological Society of America*, vol. 92, 2, 739–750.

2.17. ElarmS AlertMap: ShakeMap-Based Analysis of Earthquake Early Warning Results

Gilead Wurman, Richard M. Allen and Peter Lombard

2.17.1 Introduction

Earthquake Early Warning (EEW) efforts at the Berkeley Seismological Laboratory have recently expanded to become part of a large statewide effort involving Caltech, SCEC, the USGS and Berkeley to evaluate EEW algorithm performance in California. As part of this effort we have been developing several diagnostic tools to assess the performance of the ElarmS EEW methodology being developed at UC Berkeley. One of these tools incorporates elements of ShakeMap (*Wald et al.*, 2005) to generate second-by-second maps of predicted shaking based on data available to ElarmS in that second. We term these products AlertMaps.

These maps are very useful in evaluating the overall performance of ElarmS (and potentially other EEW algorithms) because they provide an intuitive geospatial representation of the availability of data and the behavior of the ElarmS methodology at each point in time. We discuss the technical aspects of generating AlertMaps, and present several snapshots of the AlertMap generated for the 20 July 2007 M_w 4.2 Oakland Earthquake.

2.17.2 Generating ElarmS AlertMaps

Since February of 2006 we have been automatically executing the ElarmS algorithm for every event of $M \geq 3$ in northern California (*Wurman et al.*, 2007). As this processing is performed without human input, we refer to the procedure as Non-Interactive (NI) processing. We currently produce AlertMap output as part of the NI processing, allowing us to evaluate the performance of ElarmS for every event, a task that was much more difficult before the development of the AlertMaps.

In the NI processing procedure, ElarmS produces plain-text output once per second for 60 seconds beginning at the event origin time. The output contains all the data available to ElarmS in that second, including peak ground motion observations for each station, as well as station triggers and associated parameters such as maximum predominant period (τ_p^{max}) and peak velocity or displacement ($P_{d/v}$) for that station and channel. The output also includes the event information (location, origin time, magnitude and other metadata) for each event associated from the individual station data.

The AlertMap output is entirely derived from this plain-text timeslice data, which is converted to AlertMap output via a series of perl scripts. The first of these digests the ElarmS text output at each second and converts it to XML files formatted for use by ShakeMap (*Wald et al.*, 2005). A ShakeMap subroutine then executes for each second of output, producing a raster of ground motion predictions on a regular grid of approximately 2.5° lat by 4.2° lon around the estimated epicenter of the event. In addition, ShakeMap produces an XML file of predicted ground motion at just under 400 broadband stations of the NCSN and BDSN networks. All these ground motion predictions are based on the event location and magnitude, as well as any observations of actual peak ground motion available in each second. Using present computing resources, this step takes approximately 10 seconds to produce a one second timeslice. Reducing this processing time is a matter both of dedicating more computing re-

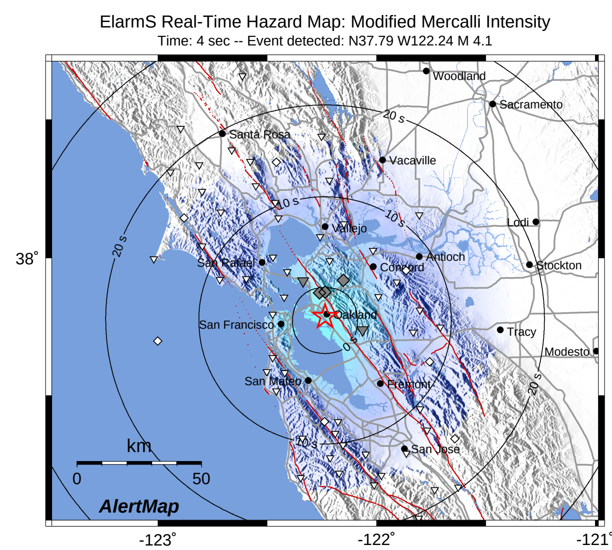

PERCEIVED SHAKING	Not felt	Weak	Light	Moderate	Strong	Very strong	Severe	Violent	Extreme
POTENTIAL DAMAGE	none	none	none	Very light	Light	Moderate	Moderate/Heavy	Heavy	Very Heavy
PEAK ACC.(%g)	<.17	.17-1.4	1.4-3.9	3.9-9.2	9.2-18	18-34	34-65	65-124	>124
PEAK VEL.(cm/s)	<0.1	0.1-1.1	1.1-3.4	3.4-8.1	8.1-16	16-31	31-60	60-116	>116
INSTRUMENTAL INTENSITY	I	II-III	IV	V	VI	VII	VIII	IX	X+

Figure 2.33: AlertMap frame for the 20 July 2007 M_w 4.2 Oakland earthquake, at 4 seconds after event origin. Color scale represents predicted MMI according to the scale at bottom. Circular contours represent time until onset of peak ground motion in seconds, based on a moveout of 3.75 km/s. Triangles represent strong-motion accelerometer stations, inverted triangles represent broadband velocity stations, and diamonds represent collocated installations. Larger grey stations have reported triggers at this time.

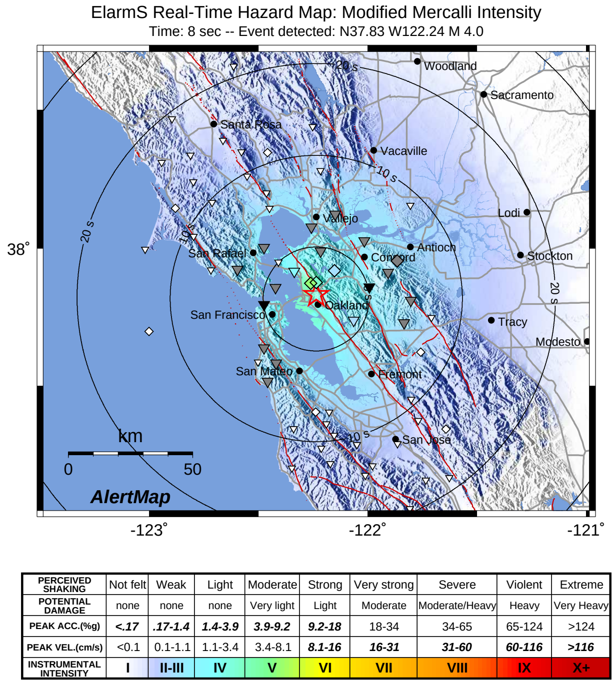

Figure 2.34: AlertMap for the Oakland event at 8 seconds after origin time. Black stations are those currently experiencing peak ground motions, and colored stations have reported peak ground motions according to the scale at bottom.

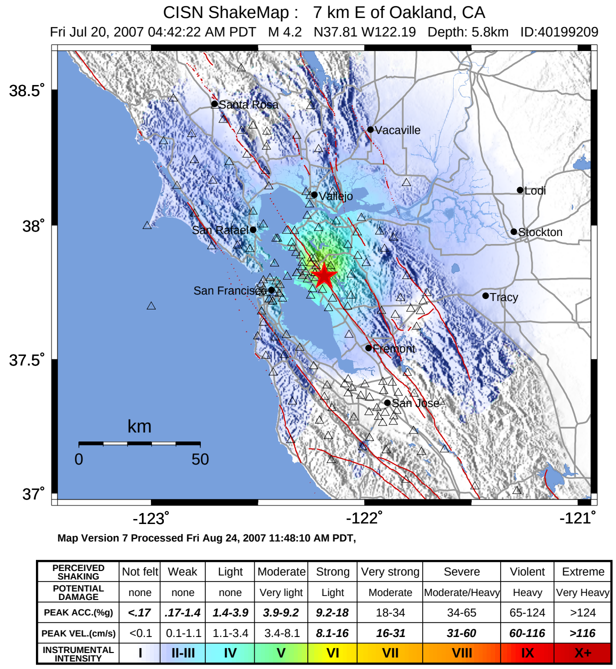

Figure 2.35: ShakeMap produced by USGS for the Oakland event. Color scale represents observations of MMI at stations (triangles) and is interpolated for all points between stations.

sources to the problem, and of simplifying the ShakeMap procedure and optimizing it to run in the minimum possible time.

When the ground motion grid files are available for all 60 seconds (less than 60 seconds if the event was not detected immediately) a script generates a Postscript map for each second, representing all the data and event parameters available in that second. Sixty of these maps are combined to produce an animation which presents the performance of ElarmS in an intuitive geospatial and temporal manner.

2.17.3 The 20 July 2007 Oakland Earthquake

On 20 July 2007 a M_w 4.2 earthquake occurred in Oakland, CA and was detected by the ElarmS NI processing. Initial event detection occurred 3 seconds after event origin, and the first magnitude estimate of M 4.1 was available one second later, or 4 seconds after origin. The magnitude estimate over the following 10 seconds varied between 4.0 and 4.3, eventually stabilizing on M 4.2 15 seconds after event origin.

Figure 2.33 shows the AlertMap at 4 seconds after origin, the time of the first magnitude estimate of M 4.1. Note the magnitude and location are recorded in the title of the map. The color scale represents the predicted modified Mercalli intensity (MMI) at all points based only on the event location and magnitude. At this time no stations have reported peak ground motions, so no bias correction has been applied to the empirical ground motion prediction equations (*Newmark and Hall*, 1982; *Boore et al.*, 1997; *Wald et al.*, 1999; *Boatwright et al.*, 2003). The grey symbols represent stations which have reported triggers at this time, and the circular contours show the time in seconds until the onset of strongest ground motions (assuming a moveout speed of 3.75 km/s). At this time the epicenter location is somewhat south of the true location, and by looking at the map it becomes apparent that this is due to the fact that only stations to the north of the event have triggered at this time, leading to temporarily poor azimuthal coverage for this time period. This problem is eliminated in the following few seconds.

By the time 8 seconds have passed since the origin, the location has stabilized and several stations have reported observations of peak ground motion (Figure 2.34). The stations which have reported peaks are color-coded according to the corresponding MMI in this map, while stations currently experiencing peak ground shaking are filled in black. The observations of peak ground motion are used to compute a bias to the ground motion prediction equations, altering the predicted ground motions around the epicenter. Note that Oakland has already experienced peak ground motion (in fact it had already experienced the peak even 4 seconds after the origin), and San Francisco is just beginning to experience peak ground motion. However, much of the remaining Bay Area receives as much as 10 to 15 seconds warning. We find that the performance of ElarmS depends primarily on the density and distribution of stations around the source, so that the warning time for an event of this size would be comparable to that for a larger event ($M_w \sim 7$) if it were to nucleate in the same area.

An additional benefit to using ShakeMap algorithms to generate AlertMaps is this makes direct comparison between ElarmS predictions and the actual ShakeMap for each event. Figure 2.35 shows the ShakeMap for this event produced by USGS. A comparison between the ShakeMap and the AlertMap frames shows that even the first available ground motion predictions (Figure 2.33), which are based entirely on the event location and magnitude, are very similar to the observations shown in the ShakeMap. The availability of actual peak ground motion observations in Figure 2.34 helps to refine these predictions further.

2.17.4 Conclusions

We are currently generating an animated AlertMap for the first 60 seconds of each event of $M \geq 3$ in northern California. These AlertMaps allow us to assess simply and quickly the performance of ElarmS for each of these events. The information presented in these maps is organized in an intuitive geospatial manner which is immediately familiar to users of ShakeMap, allowing for easy direct comparison between ElarmS predicted ground motions and actual observed ground motions represented in the regular ShakeMap product.

2.17.5 Acknowledgements

We thank Dave Wald for helpful discussions relating to ShakeMap. This work was funded by USGS/NEHRP Grants 05HQGR0074 and 06HQAG0147.

2.17.6 References

Boatwright, J., H. Bundock, J. Luetgert, L. Seekins, L. Gee, and P. Lombard, The dependence of PGA and PGV on distance and magnitude infered from northern California ShakeMap data, *Bull. Seismol. Soc. Am., 93,* 2043-2055, 2003.

Boore, D.M., W.B. Joyner, and T.E. Fumal, Equations for estimating horizontal response spectra and peak accelerations from western North American earthquakes: A summary of recent work, *Seismol. Res. Lett, 68,* 128-153, 1997.

Newmark, N.M., and W.J. Hall, Earthquake spectra and design, *Geotechnique, 25,* 139-160, 1982.

Wald, D.J., V. Quitoriano, T.H. Heaton, and H. Kanamori, Relationship between peak ground acceleration, peak ground velocity, and modified Mercalli intensity for earthquakes in California, *Earthquake Spectra, 15,* 557-564, 1999.

Wald, D.J., B.C. Worden, V. Quitoriano, and K.L. Pankow, ShakeMap®Manual: Technical manual, users guide, and software guide, *Tech. Methods 12-A1,* U.S. Geol. Surv., Reston, VA, 2005.

Wurman, G., R.M. Allen, and P. Lombard, Toward earthquake early warning in northern California, *J. Geophys. Res., 112,* B08311, doi:10.1029/2006JB004830, 2007.

2.18. Parkfield-Hollister Electromagnetic Monitoring Array

Karl Kappler, H. Frank Morrison, Gary D. Egbert

2.18.1 Introduction

The primary objective of the UC Berkeley electromagnetic (EM) monitoring array is to identify EM fields that might be associated with earthquakes. For an overview of the sites and instruments see *Kappler et al. 2006*. We have continued to analyze the data from the Parkfield-Hollister (PKD-SAO) electromagnetic monitoring array taken during the four-year time window January 2002 to December 2005. We stress that although the data have been collected since 1996, large gaps in data acquisition due to lack of funding for array maintenance, together with incomplete documentation of when array sensors were swapped out and/or repaired, has made it difficult to examine small variations in parameters derived from array data. The focus this year has been on identifying those components of the EM fields observed which are coherent with natural micropulsations of earth's magnetosphere. The residuals obtained by removing this known natural source reflect the EM activity which is incoherent with the dominant natural fields. The method of separation is based upon projecting the observed data onto the eigenvectors of the robust estimated spectral density matrix (SDM).

2.18.2 Data Analysis

We point out that there are several regions in our four year window where robust estimates of the SDM could not be calculated, as this procedure [*Egbert 1997*] relies upon having at least two observatories operating; on several occasions either one or both of the observatories were not operational, or at least one group of channels (electric or magnetic) at a single site were down. Since there are many disjoint time windows to analyze, and our primary interest is identifying any variation in EM fields which may possibly be associated with the M6 Parkfield 2004 earthquake, we focused first on the days [137-299], 2004. This 163-day window features no swapping of instruments, auxiliary power supplies, or data loggers. Signal-to-noise ratios for all primary array channels are very good, with the exception of Hy at SAO, which was slightly degraded. This slight degradation did not significantly impact our robust SDM estimates. The SDM is estimated in each frequency band from a multivariate time-series of band averaged Fourier coefficients, having dimension NxM, when N is the number of array channels, and M is the number of time windows which were Fourier transformed out of a day's data (typically 898 for Periods 4-30s). The actual robust SDM estimate is calculated as per the iterative method of *Egbert 1997*, resulting in a collection of 25 covariance matrices, (one matrix for each frequency band) for each of our 163 days. In order to compress and display this data, we reduce each SDM to a list of its four dominant eigenvalues. These are calculated in units of signal to noise ratio. For all data presented in this summary we consider the array to be comprised of the eight primary channels, 100m electrodes and horizontal magnetometers. Figure 2.36 is a plot of these daily eigenvalues.

Since the dominant eigenvector on one day is not necessarily collinear, or even approximately collinear with the dominant eigenvector calculated on some other day, Figure 2.36 is subject to variation resulting from the fact that it was made by simply ordering the eigenvalues in descending fashion. The lack of guaranteed day-to-day continuity in eigenvalues suggests that a time series plot obtained by plotting daily eigenvalues of the SDM is difficult to interpret physically. This motivates us to look at the prevailing modes of the eigenvector decomposition. A two-week window comprising days 137-151 was sub-selected, and each day's dominant eigenvectors were averaged according to the ranks of their corresponding eigenvalues. In this we obtain four dominant average modes. These modes are simply linear combinations of array channels, which tend to exhibit coherence, on average. By calculating daily the power observed in each mode, we obtain the following time series:

It is apparent from Figure 2.37 that the third eigenvalue shows a weekly period, implying that most of the power in this mode can be attributed to cultural noise. At least some of the unusual noise in the highest frequency band of the third eigenvalue seems to have dispersed into the fourth, and possibly other average modes. This may suggest that signal of this period is not coherent with typical cultural noise. The two dominant modes of the SDM are normally associated with the plane-wave natural micropulsation sources [*Egbert 1989*]. We suggest that any signals associated with seismic activity along the fault – should they exist – are unlikely to be coherent with the MT source-field. As a method of looking more closely at the recorded time-series, we calculate residual fields by subtracting off the contributions of these natural fields. We select a method of residual calculation that uses sensors at a remote site to predict fields at PKD, where the intersite transfer function itself is calculated as an average over the two week interval (days 137-151). Our residual calculation intentionally uses no Parkfield data, except in the transfer function calculation, which is performed over a time-window distant from the earthquake, ensuring that the residuals will not unintentionally iden-

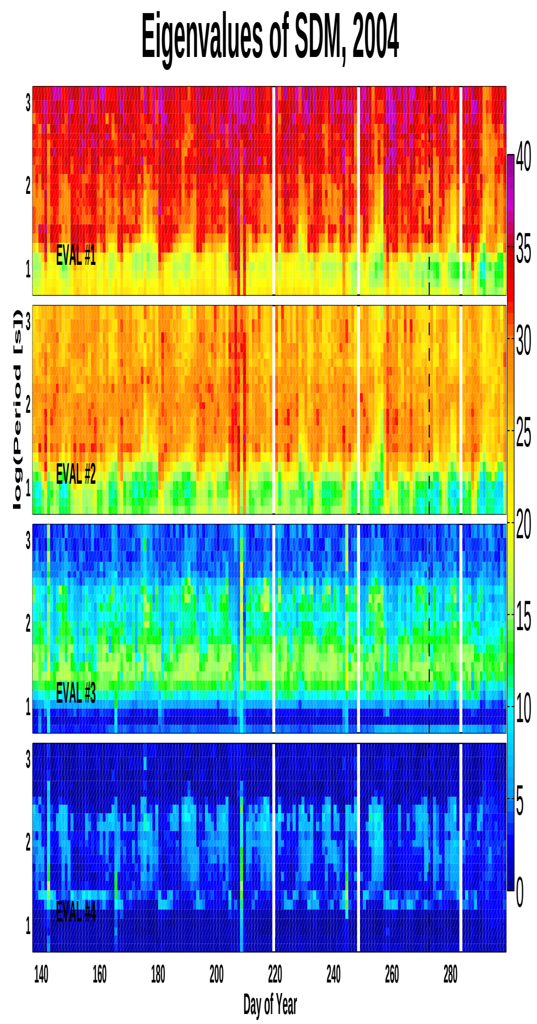

Figure 2.36: Eigenvalues of the SDM, the y-axis is log(Period (s)), and the x-axis is day-of-year. The color bar represents units (10*log10(SNR)). Note the variation in amplitude in the highest frequency of the third eigenvalue.

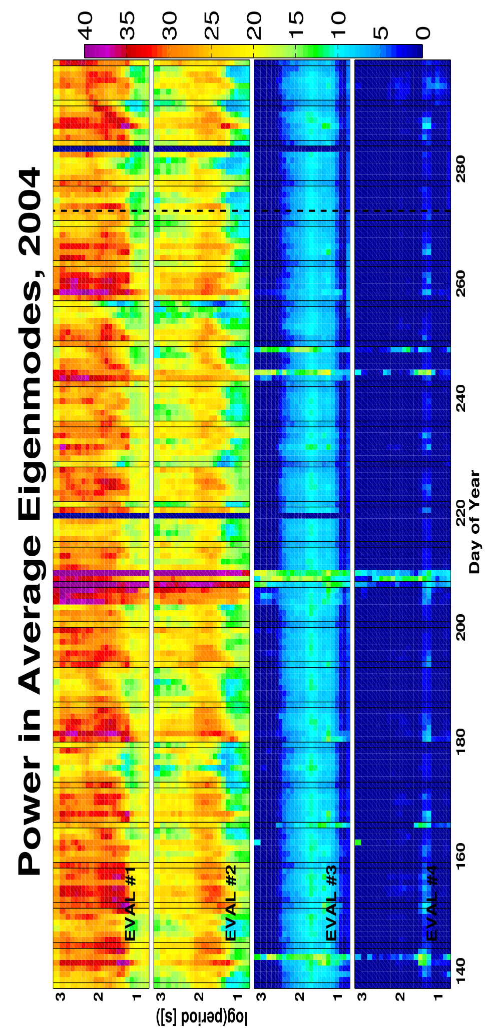

Figure 2.37: Power observed in dominant modes of the SDM. Note the large increase in power around days 205-210, which correspond to a major solar storm. Sundays are marked with thin black vertical lines, and the earthquake with the thick black dashed line

tify the signature of an EM process at work only at PKD by lumping such a signature in with the predicted signal. We use a method based on the average eigenmodes calculated from the SDM, which is essentially a method of similar triangles. Recall that an eigenvector of the SDM is simply a linear combination of array channels.

$$EV_k = \sum_{i=1}^{N_{PKD}} p_{i,k} P_i + \sum_{i=1}^{N_{SAO}} s_{i,k} S_i \qquad (2.1)$$

where $s_{i,k}$, $p_{i,k}$ are scalar coefficients for the k^{th} eigenmode, and P_i, S_i are array data for SAO and PKD respectively. The index of summation N_{site} reflects the number of channels operating at the site. Numeric values for the $p_{i,k}$ and $s_{i,k}$ are fixed during the calculation of the k^{th} average eigenmode, and yield the fixed PKD to SAO component ratio:

$$PS_k = \frac{\sum_{i=1}^{N_{PKD}} {p_{i,k}}^2}{\sum_{i=1}^{N_{SAO}} {s_{i,k}}^2} \qquad (2.2)$$

Now choosing an eigenmode, i.e. fixing k (we thus omit further reference to k), we can project actual SAO data onto the chosen mode, observing a set of coefficients:

$$\sum_{i=1}^{N_{SAO}} \left[s_i^{obs}\right]^2 \qquad (2.3)$$

We then predict the PKD data assuming the existence of a complementary vector, collinear with $\Sigma\, p_i\, P_i$ obeying the ratio:

$$\frac{\sum_{i=1}^{N_{PKD}} {p_i}^2}{\sum_{i=1}^{N_{SAO}} {s_i}^2} = \frac{\sum_{i=1}^{N_{PKD}} \left[p_i^{pred}\right]^2}{\sum_{i=1}^{N_{SAO}} \left[s_i^{obs}\right]^2} \qquad (2.4)$$

By solving for the predicted PKD signal for the first two eigenmodes, and subtracting from the recorded PKD data, we obtain residual fields.

Figure 2.38 illustrates the signal (predicted) and residual fields for the sensor Hy (oriented N-S) at PKD for three months around the earthquake. We choose to show the band at a period of 85s because this period is in the midst of the band where magnetic anomalies were reported by *Fraser-Smith et al.* We see that no significant variation is evident in either the natural fields or in the local residual fields.

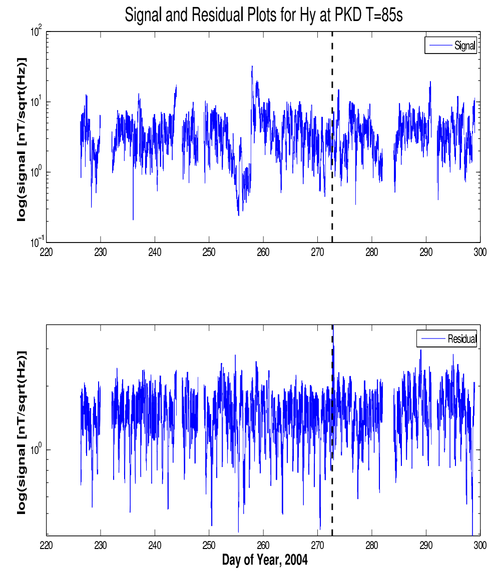

Figure 2.38: Magnetic Fields Calculated from SAO (a) and Residual Magnetic fields from subtracting predicted fields from observed data (b)

2.18.3 Future Work

This year we plan on a statistical analysis of the residuals for all bands over the 163 day time window. Any bands showing statistically significant variation around the time of the earthquake will be expanded in the time window to a four-year analysis in order to better gauge the time-scale on which the outliers are significant. Special attention will be paid to the residuals in the so-called MT "dead-band", near our high frequency cutoff. Since there is very little natural signal or cultural noise in this band (Figures 2.36 and 2.37), it would be the band in which anomalous signals ought to stand out most readily if they were present.

2.18.4 References

Egbert, G.D., Booker, J.R., (1989), Multivariate Analysis of Geomagnetic Array Data 1.The Response Space, *Journal of Geophys. Res.* V94 No.B10 pp14227-14247

Egbert G. D. (1997), Robust multiple-station magnetotelluric data processing, *Geophys. J. Int. 130* pp475-496

Fraser-Smith, A. C., Bernardi, A., McGill, P. R., Ladd, M. E., Helliwell, R. A., and Villard, O. G., 1990, Low-frequency magnetic field measurements near the epicenter of the Ms 7.1 Loma Prieta Earthquake, *Geophys. Res. Lett.*, 17, 1465-1468

Kappler, K., Egbert, G.D., Morrison, H.F., Parkfield-Hollister Electromagnetic Monitoring Array, *BSL Annual Report*, 2006

Kappler, K. Egbert, G.D., Morrison, H.F., Long-Term Analysis of ULF electromagnetic fields at Parkfield CA, *in progress*

2.19. Creep on the Rodgers Creek Fault Identified Using PS-InSAR

Gareth Funning, Roland Bürgmann and Alessandro Ferretti (TRE, Milan)

2.19.1 Introduction

Deformation in the northern San Francisco Bay Area is dominated by a series of sub-parallel strike-slip faults. Existing GPS observations provide some constraint on the slip rates of these faults, however these have only limited resolution for resolving shallow fault behavior, such as brittle creep. We use Permanent Scatterer InSAR (PS-InSAR) data to dramatically increase the density of surface deformation observations. We find a discontinuity in observed surface velocities across the Rodgers Creek fault, around Santa Rosa and further north, consistent with shallow creep at rates of up to 6 mm/yr (*Funning et al.,* ,2007). The creeping segments are located in areas of local transtension, suggesting that lowered normal stresses may play a role in the distribution of creep. The existence of creep could significantly reduce expected moment release in future earthquakes on the Rodgers Creek fault, and thus has implications for seismic hazard assessment.

2.19.2 Data

For this study we use data acquired by the European Space Agency satellites ERS-1 and ERS-2 between 1992 and 2001. The North Bay region is covered in its entirety by a single descending track scene (track 342, frame 2835), and in total 30 useable images were acquired over this frame in the study interval. Permanent scatterers (PS) were identified using the method of *Ferretti et al.* (2001) , and a best linear line-of-sight (LOS) velocity estimated for each. In total, 71000 PS were identified (Figure 2.39a).

On a regional scale, the velocity field obtained by PS-InSAR shows the deformation due to accumulation of strain on the major strike-slip faults. In Figure 2.39a this is represented by a color change from red to blue from west to east, signifying an eastward increase in velocity of $\sim$ 10 mm/yr towards the satellite. This is consistent with right-lateral shear across the fault system (e.g. *Bürgmann et al.*, 2006). More locally, steps in LOS velocity across faults represent shallow creep on those structures. We can identify such features for the Hayward and, we argue below, Rodgers Creek faults.

2.19.3 Estimating creep rate from velocity profiles

In the vicinity of Santa Rosa, we observe a step in velocity across the Rodgers Creek fault. We investigate this feature, which we interpret as representing surface fault creep, by plotting cross-fault profiles through our reduced PS-InSAR dataset at 5 km intervals (Figure 2.39b,c). To estimate fault offset rates, we fit parallel straight lines to windows of datapoints on either side of the fault, and calculate the separation between them. The gradients of the lines reflect the regional component of deformation, along with any residual error in satellite orbital position, and are used to detrend the profiles. Assuming pure right-lateral strike-slip motion, we then convert the LOS velocities to creep rates, propagating the uncertainties of the measurements through the calculation.

We obtain rates which peak at 6.0 ± 0.6 mm/yr immediately north of Santa Rosa (profile G–G'), and die off to the north and south. It is possible that the southernmost profile (H–H') appears less steplike than when plotted in plan view (Figure 2.39b) due to the fault bend at Santa Rosa. These rates, which represent the averages over an 10 year interval, are comparable with the estimate of 4.3 mm/yr recently obtained from alignment array measurements at site RC1 (Figure 2.39b) which do not overlap in time with our measurements.

2.19.4 Discussion

Significant creep is observed over a 25 km zone north of Santa Rosa, but not further south – in our dataset or by other workers, raising the question of the cause of this along-strike change in fault behavior. One potential factor is fault geometry – if slip were transferred eastwards to the Maacama fault, north of Santa Rosa, there would be a $\sim$ 8 km releasing stepover consistent with an unclamping of the Rodgers Creek fault. Further targeted PS-InSAR and GPS studies may allow us to determine where this slip transfer occurs, and thus to quantify the importance of this effect.

2.19.5 Acknowledgements

This work was supported by grants from the Department of Energy and the USGS-NEHRP external program. SAR data are copyrighted by the European Space Agency and were obtained via the WInSAR consortium.

2.19.6 References

Bürgmann, R., G. Hilley, A. Ferretti, and F. Novali, Resolving vertical tectonics in the San Francisco Bay area from GPS and permanent scatterer InSAR analysis, *Geology*, *34*, 221–224, 2006.

Ferretti, A., C. Prati, and F. Rocca, Permanent scatterers in SAR interferometry, *IEEE Trans. Geosci. Remote Sensing*, *39*, 8–20, 2001.

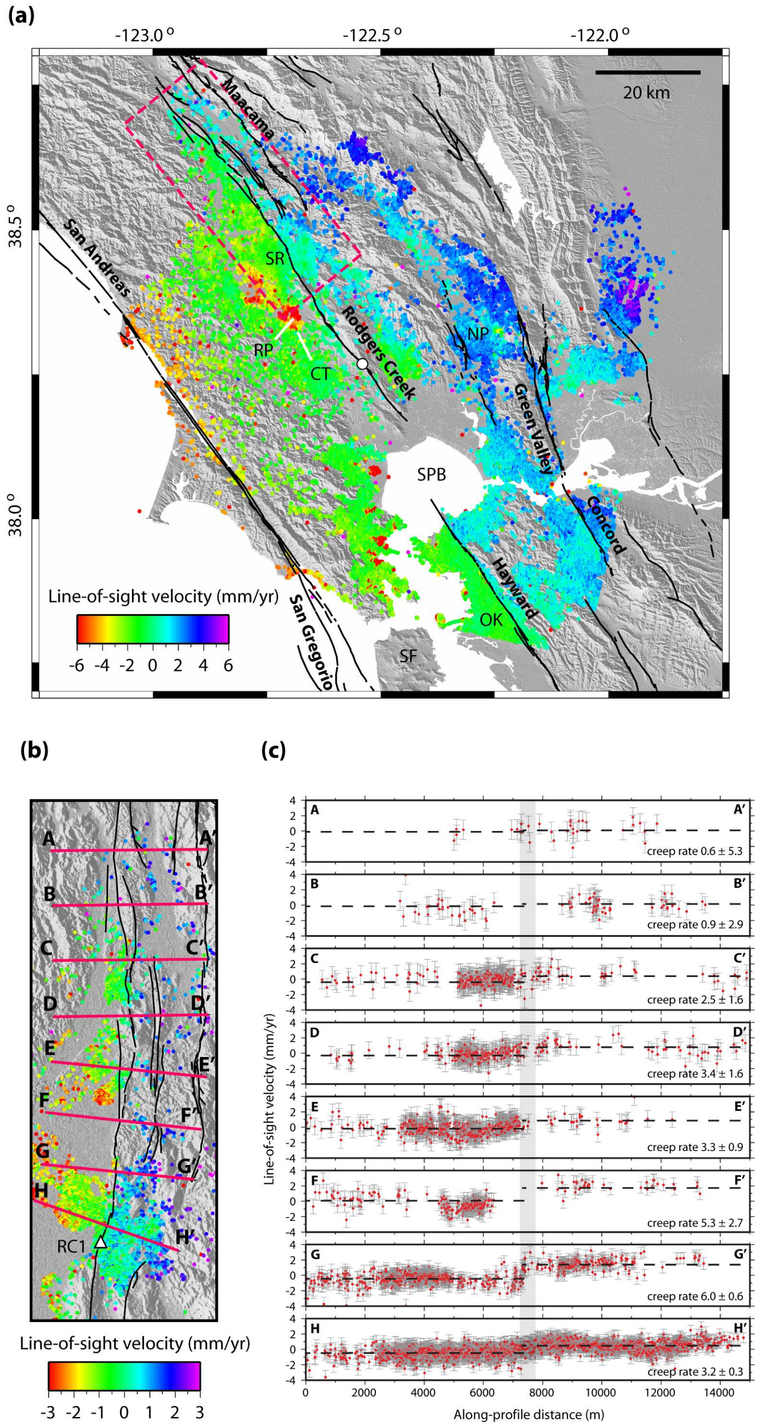

Figure 2.39: PS-InSAR evidence for creep on the Rodgers Creek fault. *(a)* Regional surface velocity field. Solid lines show mapped active faults. Dashed box shows location of *(b)*. [SR: Santa Rosa, RP: Rohnert Park, CT: Cotati, NP: Napa, SF: San Francisco, OK: Oakland, SPB: San Pablo Bay] *(b)* Detail of velocities in the Santa Rosa area. Note change in color palette. Locations of 15 km-long fault-perpendicular profiles are shown. White triangle indicates location of alignment array RC1. *(c)* Profiles of PS-InSAR data across the Rodgers Creek fault near Santa Rosa. Red points signify PS velocity measurements within 2.5 km of the profile line; error bars indicate 1σ uncertainties. Black dashed line indicates the best average linear fit to velocities from a range of windows either side of the fault. Gray box indicates the approximate location of the fault.

2.20. Asymmetric motion across the San Francisco Bay Area faults. Implications on the magnitude of future seismic events.

Nicolas Houlié and Barbara Romanowicz

2.20.1 Introduction

The San Francisco Bay area is one of the tectonically most deformed areas in the world. This deformation is the result of relative motion of the Pacific (PAC) and North-America (NAM) plates. A large part of the strain (75%) is accommodated along structures lying in a 50 km wide land stripe. At least two major seismic events ($M_w \geq 6.5$) are expected along the San Andreas (SAF) and Hayward faults (HAY) within the next decades. Triggering effects between the two seismic events may not be excluded (*Lienkaemper et al.*, 1997). The last major event in the area occurred in 1989 (Loma Prieta event) (*Segall and Lisowski* 1990, *Dietz and Ellsworth* 1990). The velocity field after this large event was perturbed (*Argus and Lyzenga* 1994) and the microseismicity significantly increased since then in the southern portion of the San Francisco Bay Area (SFBA) (ANSS catalog). As the prediction of the next event is based on the estimation of the energy accumulated along active faults (San Andreas, Hayward, Rogers Creek, Calaveras, Green Valley fault, Greenville fault), it is important to quantify the strain amplitude during the interseismic cycle across these faults. Dedicated to monitoring the deformation of Northern California, the Bay Area Regional Deformation (BARD) network provides data with which we can investigate the spatial distribution of the strain accumulation, the motion along faults and any unexpected transient deformation that would be related to seismic events (acceleration along the fault, landslides, hydrogeological features). Our study area will be limited in this work to the San Francisco Bay Area (SFBA).

Here we test the potential asymmetry of the motion along the San Andreas and San Gregorio faults. The asymmetry of the motion is a unique opportunity to link the velocity models used in seismic tomography and moment tensor inversions with geodetic observations, by investigating the rigidity of the PAC oceanic crust. The asymmetry was already mentioned both by geodesists (*Lisowski, M.,* 1991) and by seismologists *Le Pichon et al.,* 2005) but never tested in the SFBA on a real geodetic dataset. We evaluate the velocity field in the light of this hypothesis. We discuss the implications of the new location of the strain peak from the perspective of a future event. Additionally we provide some elements on the geometry of tectonic features in the San Pablo Bay region.

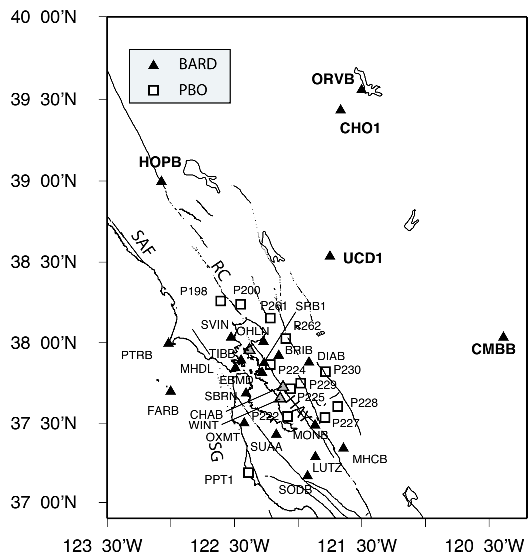

Figure 2.40: Map of the permanent GPS benchmarks of the BARD (black triangles) and PBO (white squares) networks. The sites HCRO (Hat Creek Radio Observatory), PKDB (Parkfield, CA), SAOB (San Andreas Geophysical Observatory) and YBHB (Yreka Blue Horn Mine, CA) are located outside the map.

2.20.2 Data and data processing

The BARD network is a permanent GPS network comprising 40 GPS sites, installed since 1994 in Northern California (*Romanowicz et al.*, 1994). Some of these sites have been transferred to the Plate Boundary Observatory (PBO), but not all. The receivers operating are mainly Ashtech (Z-12 and μZ) and Trimble receivers (TR4000) with Choke Ring antennas. During the last two years, the network was upgraded, replacing the old receivers (mostly Ashtech Z-12) by Trimble NETRS with high-rate capabilities. The BARD network is streaming data to the Berkeley Seismological Laboratory in real-time (from 1s to 15s) (*Romanowicz et al.*, 1994). All the data are archived at the Northern California Earthquake Data Center (NCEDC, `http://www.ncedc.org`) (*Neuhauser et al.*, 2001). Today, the BARD network has operated long enough to provide high accuracy velocities in the San Francisco Bay Area (*Blewitt and Lavallée*, 2002).

All the data have been processed by using the GAMIT/GLOBK tool suite (*King and Bock*, 2006, *Herring*, 2005). We have adjusted all the 4018 daily solutions using five reference sites (BAY1, GOLD, JPLM, PPT1, VNDP) that are present in our dataset and included in the ITRF2000 release (*Altamimi et al.*, 2002). The adjustment of the whole dataset of daily solutions was succesfully completed by minimizing the shifts between the ITRF velocities and our solutions.

2.20.3 Results

Both asymmetric and symmetric deformation models are able to fit the GPS observations in the azimuth N55. We confirm that the transverse compressive component of the deformation across the Hayward fault is negligible. The location of the strain measurable from the GPS observations in the SFBA and its related shear stress rate have a direct impact on the expected time-recurrence of large earthquake in the Bay Area (*Thatcher*, 1990). We argue that discriminating between the two models is necessary in order to better integrate the GPS observations into constraints on the seismic cycle deduced from the monitoring of the seismic events and long-term geological evidences.

2.20.4 References

Altamimi, Z., P. Sillard, and C. Boucher (2002), ITRF2000: A New Release of the International Terrestrial Reference Frame for Earth Science Applications, *J. Geophys. Res.*, *107*(B10), 2114, doi:10.1029/2001JB000561.

Argus, D., and G. Lyzenga (1994), Site velocities before and after the Loma Prieta and Gulf of Alaska earthquakes determined from VLBI, *Geophys. Res. Lett.*, *21*(5), 333–336.

Blewitt, G., and D. Lavallée (2002), Effect of annual signals on geodetic velocity, *J. Geophys. Res.*, *107*(B7), 2145, doi:10.1029/2001JB000570.

Dietz, L., and W. Ellsworth (1990), The October 17, 1989, Loma Prieta, California, earthquake and its aftershocks: Geometry of the sequence from high-resolution locations, *Geophys. Res. Lett.*, *17*(9), 1417–1420.

Herring, T. (2005), *GLOBK: Global Kalman Filter VLBI and GPS Analysis Program, version 10.2*.

King, N., M. Murray, W. Prescott, R. R Clymer, and B. Romanowicz (1994), The bay area regional deformation (bard) permanent gps array, in *Eos Trans. AGU, Fall Meet. Suppl*, S42B-09.

King, R., and Y. Bock (2006), *Documentation of the GAMIT software*, MIT/SIO.

Le Pichon, X., C. Kreemer, and N. Chamot-Rooke (2005), Asymmetry in elastic properties and the evolution of large continental strike-slip faults, *J. Geophys. Res.*, *110*(B03405), doi:10.1029/2004JB003343.

Lienkaemper, J., J. Galehouse, and R. Simpson (1997), Creep response of the Hayward fault to stress changes caused by the Loma Prieta earthquake, *Science*, *276*, 2014–2016.

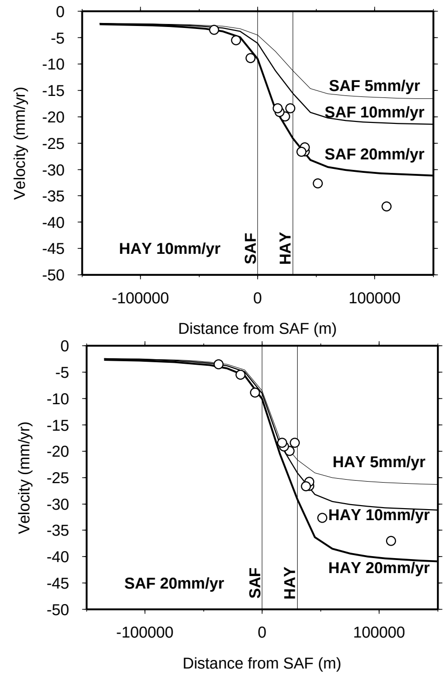

Figure 2.41: Validation of the asymmetric hypothesis of motion across SAF and HAY faults. Both locking depths are equal to 10 km. We combine the velocity fields associated wth SAF and HAY. By varying the velocity along the Hayward (top) and San Andreas fault (bottom), keeping the other velocity fixed, we have determined the slip velocities of the HAY and SAF are respectively equal to 10 and 20 mm/yr. Some additional residuals are visible at the UCD1 site. This residual velocity could be explained by different sources such as the interseismic deformation related to Calaveras or Greenville faults.

Lisowski, M., J. Savage, and W. Prescott (1991), The Velocity Field Along the San Andreas Fault in Central and Southern California, *J. Geophys. Res.*, *96*(B5), 8369–8389.

Neuhauser, D., D. Oppenheimer, S. Zuzlewski, L. Gee, M. Murray, A. Basset, W. Prescott, and B. Romanowicz (2001), Collaborative projects at the northern california earthquake data center (ncedc), *Eos Trans. Am. Geophys. Union*, *82*(47).

Romanowicz, B., D. Neuhauser, B. Bogaert, and D. Oppenheimer (1994), Accessing northern California earthquake data via Internet, *Eos Trans. Am. Geophys. Union*, *75*(23).

Segall, P., and M. Lisowski (1990), Surface Displacement in the 1906 San Francisco and 1989 Loma Prieta Earthquakes, *Science*, *250*, 1241–1243.

Thatcher, W. (1990), Present-day crustal movements and the mechanics of cylic deformation, in *The San Andreas Fault system, California*, vol. 1515, pp. 189–205.

2.21. A Decade of InSAR Observation across the Creeping Segment of the San Andreas Fault

Isabelle Ryder and Roland Bürgmann

2.21.1 Introduction

The San Andreas Fault system stretches from the southern California border 1,100 km northeastwards right up to the Mendocino triple junction offshore northern California. For much of its length, the fault is locked, displaying no significant offset between large seismic events. The parts of the fault that ruptured during the 1857 M_w 7.9 Fort Tejon earthquake and the 1906 M_w 7.9 San Francisco earthquake are examples of portions of the fault that are locked. In between these two rupture zones lies the 170 km-long creeping segment, from now on abbreviated CSAF. Various types of surface measurement in the last three decades or so have amply demonstrated that creep occurs along this section, with estimated creep rates up to 34 mm/year (*Burford and Harsh*, 1980; *Lisowski and Prescott*, 1981; *Schulz*, 1982; *Schulz*, 1989; *Titus et al.*, 2005). Since the discovery of creep at the Cienega Winery by Tocher in 1960 (*Tocher*, 1960), the CSAF has essentially become the world's type locality for fault creep: no other fault section is known to creep along such a great length, nor at such a high rate. Several other faults in the San Andreas Fault system have well-documented creep, for example the Calaveras Fault (e.g. *Rogers and Nason*, 1971; *Johanson and Bürgmann*, 2005) and the Hayward Fault (e.g. *Savage and Lisowski*, 1993; *Simpson et al.*, 2001), but the rates are less than 10 mm/year. Why some faults creep while others are locked is not known. It is, however, important to study this question. Collectively, the creeping faults in the San Francisco Bay region constitute a major part of the San Andreas Fault system; if we are to know the system well enough to predict earthquakes, then we need to understand the mechanics of creep. In this project we use Interferometric Synthetic Aperture Radar (InSAR) measurements covering almost a decade to record spatial variations in creep rate along the CSAF. We then invert these surface data for shallow creep rates and deep slip rates on the fault.

2.21.2 InSAR Observations

We use SAR data from the European ERS-1 and ERS-2 satellites acquired between May 1992 and January 2001 to construct interferograms across the CSAF. Processing was carried out using the Caltech/JPL software ROI_PAC (*Rosen et al.*, 2004), with a bridge unwrapping algorithm. Topographic effects were removed using a 90 m digital elevation model derived from Shuttle Radar Topography Mission (SRTM) data (*Farr and Kobrick*, 2000; *Rodriguez et al.*, 2006). Agriculture in the Salinas valley and the San Joaquin basin results in temporal decorrelation in many of the interferograms, and steep topography, particularly on the northeast side of the fault, leads to geometrical decorrelation. Collectively, these zones of incoherence lead to isolated patches in the unwrapped interferograms. Figure 2.42 shows a stack of twelve interferograms which can be unwrapped consistently across the fault. The stacking process increases the signal-to-noise ratio above that of individual interferograms, so that a more robust identification of spatial variations in creep rate can be made. The stack assumes a linear velocity for each pixel. The fault is clearly delineated by the abrupt offset running northwest to southeast across the stack image. The displacement gradient near the fault is much greater than would be expected for a fault locked to the bottom of the seismogenic layer (about 12-15 km in this region), implying that significant shallow slip occurred during the decade of observation. The positive range change on the southwest part of the image is enhanced in the Salinas Valley. We surmise that this enhancement is due to subsidence caused by aquifer discharge in this highly agricultual area. The area of > 10 mm/year positive range change in the southeast quadrant of the stack exactly coincides with the town of Coalinga and the nearby oil fields. It is possible that this range change anomaly is due to pumping of oil. The agreement of our 9-year creep rate with estimates obtained by other workers over earlier and/or longer periods of time show that creep rate on the years to decadal time scale has been approximately constant over the last 30 years. If there was any increase in creep rate as a result of either the 1857 Fort Tejon or the 1906 San Francisco earthquake, then presumably the rate has now levelled off.

2.21.3 Inversion for Creep Rate

To obtain an idea of the distribution of creep rate, we perform inversions using both the InSAR stack and GPS velocities. The CSAF is well-covered by continuous (Plate Boundary Observatory) and campaign GPS sites. Initially, separate InSAR and GPS inversions are carried out, as preliminaries to a joint inversion. The InSAR stack is downsampled by a factor of 20 in the north and east directions. Slip is constrained to be positive (i.e. right-lateral), and an upper bound of 40 mm/year on the slip rate is imposed. In the joint inversion, a maximum shallow creep velocity of 33 mm/year occurs in the centre of the segment, and to first order tapers off on either side, more rapidly to the south than to the north. This mirrors

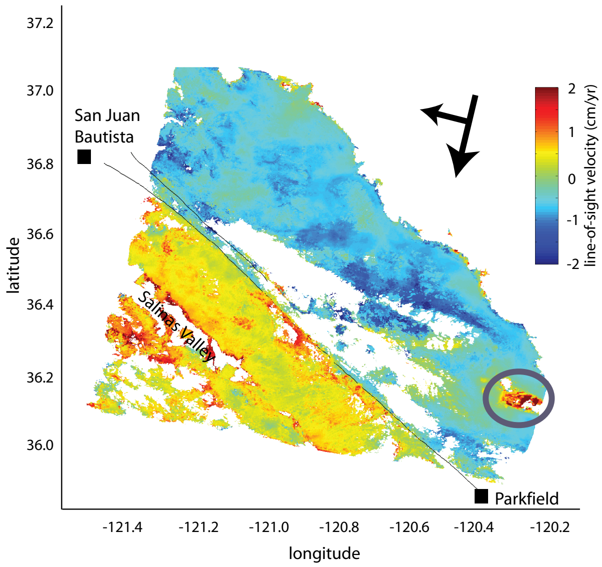

Figure 2.42: Stack of 12 descending ERS interferograms made from SAR scenes acquired between May 1992 and January 2001. Colours show range change, which is the surface displacement in the line of sight between the satellite and the ground. Red is positive range change, i.e. motion away from the satelite. Arrows show satellite ground track (towards south-southwest) and look direction (towards west-northwest). Fault traces for the CSAF and Calaveras Fault are marked. The line-of-sight offset rate across the fault is 10 mm/year, which is equivalent to a right lateral displacement rate of 32 mm/year. Grey ellipse in bottom right outlines area of suspected subsidence, possibly related to oil pumping near Coalinga. Subsidence may also be occurring in the agricultural Salinas Valley.

the pattern illustrated in Figure 3 of Titus et al. (2005), which is a compilation of surface geodetic slip rate estimates from different workers since the 1970s. Shallow creep rate falls to very low values (< 10 mm/year) around Parkfield. Intermediate depth creep rates reach a maximum of 38 mm/year just north of centre, tapering off to the north, and decreasing before rising again towards Parkfield. The deep slip rate is about 35 mm/year.

2.21.4 Future Work

The other key aspect of deformation along the CSAF that needs to be studied is the temporal variation of surface displacement and, by implication, of creep rate on the fault. Preliminary work has been started using a Persistent Scatterer approach, to construct displacement time series at individual points on the ground. This relatively new technique identifies individual radar scatterers that remain coherent over a long period of time (years to decades). In addition, time series from Plate Boundary Observatory GPS points are being studied to look for variations in creep rate over time, and possible correlations in time between features at different points along the fault. Building a detailed picture of both spatial and temporal variations should help us understand the mechanics, as well as the kinematics, of creeping fault zones.

2.21.5 Acknowledgements

This project is funded by NSF grant number EAR-0337-308. All SAR data is from the European Space Agency (ESA).

2.21.6 References

Burford, R.O. and P.W. Harsh, Slip on the San Andreas fault in central California from alinement array surveys, *Bull. Seism. Soc. Am., 70,* 1233–1261, 1980.

Johanson, I.A. and R. Bürgmann, Creep and quakes on the northern transition zone of the San Andreas fault from GPS and InSAR data, *Geophys. Res. Lett., 32,* L14306, 2005.

Lisowski, M. and W.H. Prescott, Short-range distance measurements along the San Andreas fault system in central California, 1975 to 1979, *Bull. Seism. Soc. Am., 71,* 1607–1624, 1981.

Rogers, T.H. and R.D. Nason, Active fault displacement on the Calaveras fault zone at Hollister, *Seism. Soc. Am. Bull., 61,* 399–416, 1971.

Savage, J.C. and M. Lisowski, Inferred depth of creep on the Hayward fault, central California, *J. Geophys. Res., 98,* 787–793, 1993.

Schulz, S.S., G.M. Mavko, R.O. Burford and W.D. Stuart, Long-term fault creep observations in central California, *J. Geophys. Res., 87,* 6977–6982, 1982.

Schulz, S.S., Catalog of creepmeter measurement in California from 1966 through 1988, *USGS Open File Report, 89,* 65, 1989.

Simpson, R. W., J.J. Lienkamper and J.S. Galehouse, Variations in creep rate along the Hayward fault, California, interpreted as changes in depth of creep, *Geophys. Res. Lett., 28,* 2269–2272, 2001.

Titus, S.J., C. DeMets and B. Tikoff, New slip rate estimates for the creeping segment of the San Andreas fault, *Geology, 33,* 205–208, 2005.

Tocher, D., Creep on the San Andreas fault – creep rate and related measurements at Vineyard, California, *Bull. Seism. Soc. Am., 50,* 396–404, 1960.

2.22. Indian Plate Motion, Deformation, and Plate Boundary Interactions

Edwin (Trey) Apel, Roland Bürgmann, and Paramesh Banerjee (Wadia Institute of Himalayan Geology)

2.22.1 Introduction

We use 1867 GPS-measured velocities to geodetically constrain Indian plate motion and intra-plate strain to examine plate boundary deformation and plate interactions around the Indian plate. Our solution includes 14 GPS velocities from continuously recording stations from within the stable Indian plate interior which are used to estimate the rotation parameters of the Indian plate. These refined plate motions estimates allow for the rigorous analysis of the India-Eurasia convergence zone where we estimate convergence to be 5-10% higher than previous geodetic estimates (e.g., *Paul et al.*, 2001; *Socquet et al.*, 2006a). Dense station coverage along the Himalayan range front allows us to rigorously test boundary parameterizations and develop a preferred plate boundary model. In our preferred model the Himalayan range front accumulates ~50% of the India-Eurasia convergence with as much as 25 mm/yr of slip accumulation along some segments.

We use a block modeling approach to incorporate both rigid block rotation and a first-order model of near-boundary elastic strain accumulation effects in a formal inversion of the GPS velocities. The robust plate motion parameters for Eurasia, Australia, and India allow for the rigorous testing of variable plate boundary geometries and considerations of models that include smaller microplates within the plate boundary zones. These models allow us to further illuminate patterns in the interseismic strain accumulation along the Indian plate boundaries including Himalayan range front.

2.22.2 GPS Velocities

Our primary data in this study is a solution of 164 stations, including 42 campaign style sites from central and northwestern India and 14 CGPS from India's continental interior stations that we processed. The earliest campaign data were collected in 1995, but most sites were first occupied in 2001. Occupations have been repeated every year since although some stations have been lost. Each survey-style station was occupied for 4-6 days continuously, once a year. Processing details can be found in (*Banerjee and Bürgmann*, 2002). Selected, globally distributed IGS sites were used to define an ITRF00 reference frame.

In addition to our own analysis we integrate GPS-station velocities from published work along the Himalayans, throughout China, and Southeast Asia. We integrate a large number of published solutions (*Apel et al. and references therein*, 2006b) with our own solution. These velocities were combined with our solutions by rotating them into a common reference frame. We combine velocities published in an ITFR00 reference frame into our own solution by minimizing the misfit at co-located stations. After the combination we compare our combined solution the published values to estimate misfit. For most sites the RMS is ~1-2 mm/yr, well within the 95% confidence intervals for these sites.

2.22.3 Plates and Blocks

Plate boundary locations are critical for characterizing GPS velocities and the plate kinematics of a particular region. While some plate boundaries in the Indian region are well defined by active fault traces, youthful geomorphology, and abundant local seismicity, others appear more diffuse and ambiguous. We draw on the distribution and kinematics of 20th century seismicity, local geology, and mapped faults, and the GPS velocity itself to define our block model boundaries. Within this paper the term plate (and microplate) refers to the rigid, coherent, lithospheric entity defined by faults, seismicity etc. The term block is the specific implementation of these data into a parameterized set of variables within our block model (e.g. *Apel et al.*, 2006a).

We define our blocks as rigid entities on a spherical earth bounded by dislocations in an elastic halfspace and invert for poles and rates of rotation that minimize the misfit to the GPS velocities using the block modeling code by Meade and Hager (2005). Because our inversion combines rigid block rotation with elastic strain accumulation effects, the parameterization of the block boundary geometry is critical. Geometry of the block boundaries is based heavily on seismicity and adopted from plate reconstructions (*Replumaz and Tapponnier*, 2003) and prior analyses (*Socquet et al.*, 2006a; *Reilinger et al.*, 2006; *Simons et al.*, 2007; *Meade*, 2007; *Thatcher*, 2007) or adjusted as indicated by the geodetic data.

2.22.4 Results

Some block motions are well defined and vary little within our model. The Eurasian block, Australian block, and Indian block rotation parameters are defined primarily by the sites that lie within the stable interior and are affected very little by plate boundary strain. With respect to Eurasia the pole of rotation for the Indian plate is located at 23.641±0.979°N 8.732±4.402°E with an angular rotation rate of 0.359±0.012° Myr-1 (Figure 2.43). Relative poles shown in Figure 2.43 illustrate the consistency of our solution.

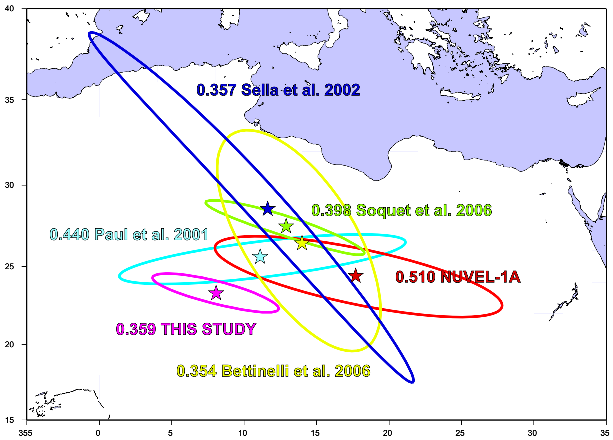

Figure 2.43: Relative plate poles of India's motion with respect to Eurasia. Values that precede the reference are the poles' magnitude measured in deg/My with a counter-clockwise positive convention.

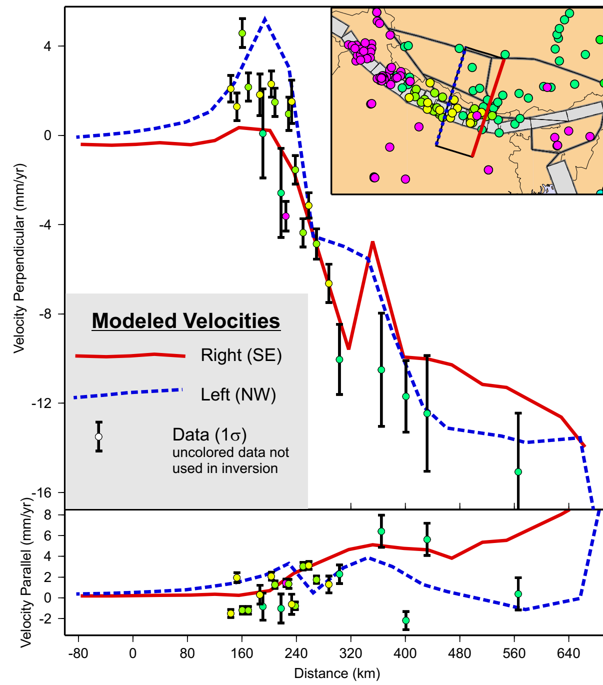

Figure 2.44: Velocity profile of measured and predicted velocities in Tibet. The inset figure shows the block configuration used in the inversion. GPS stations are colored according to source.

Along the Himalayan Range Front we estimate IND-EUR convergence to vary from 34-41 mm/yr from ∼76 °-91 ° east longitude (Figure 2.44, inset). We parameterize the Himalayan front with four main blocks defined by the major geologic features like the Indus-Zangbo suture, Gulu rift, and Karakorum fault. As much as 25 mm/yr of contraction is accommodated by the Himalayan thrust (Figure 2.44). Our model, along the front, fit the data quite well. Some systematic misfit with the Himalayan blocks may be related to unmodeled east-west extension.

2.22.5 References

Apel, E. V., R. Bürgmann, G. Steblov, N. Vasilenko, R. King, and A. Prytkov, Independent active microplate tectonics of northeast Asia from GPS velocities and block modeling, *Geophysical Research Letters*, 33, L11303, doi:10.1029/2006GL026077, 2006a.

Apel, E., R. Bürgmann, and P. Banerjee, Geodetically constraining Indian plate motion and implications for plate boundary deformation, *seismo.berkeley.edu/annual_reports/ar05_06/node19.html*, 2006b.

Banerjee, P., and R. Bürgmann, Convergence across the northwest Himalaya from GPS measurements, *Geophysical Research Letters*, 10.1029/2002GL015184, 2002.

Meade, Brendan, Mechanics of the India-Asia Collision Zone, *Geology*, 35, p. 81-85, 2007.

Meade, B. J., and B. H. Hager, Block models of crustal motion in southern California constrained by GPS measurements, *Journal of Geophysical Research*, 110, B03403, 10.1029/2004JB003209, 2005.

Paul, J., Bürgmann, R., Gaur, V. K., Bilham, R. Larson, K. M., Ananda, M. B., Jade, S., Mukal, M., Anupama, T. S.. Satyal, G., Kumar, D., The motion and active deformation of India, *Geophysical Research Letters* 28(4), 2001.

Reilinger R., et al., GPS constraints on continental deformation in the Africa-Arabia-Eurasia continental collision zone and implications for the dynamics of plate interactions, *Journal of Geophysical Research*, 111, B05411, doi:10.1029/2005JB004051, 2006.

Replumaz A., and P. Tapponnier, Reconstruction of the deformed collision zone Between India and Asia by backward motion of lithospheric blocks, *Journal of Geophysical Research*, 108 (B6), 2285, doi:10.1029/2001JB000661, 2003

Simons W. J. F., et al., A decade of GPS in Southeast Asia: Resolving Sundaland motion and boundaries, *Journal of Geophysical Research*, 112, B06420, doi:10.1029/2005JB003868, 2007.

Socquet, A., Vigny, C., Chamot-Rooke, N., Simons, W., Rangin, C. and Ambrosius, B., India and Sunda plates motion and deformation along their boundary in Myanmar determined by GPS, *Journal of Geophysical Research*, 111, B05406, 10.1029/2005JB003877, 2006a.

Thatcher W., Microplate model for the present-day deformation of Tibet, *Journal of Geophysical Research*, 112, B01401, doi:10.1029/2005JB004244, 2007.

2.23. Hidden Dykes detected on Ultra Long Period seismic signals at Piton de la Fournaise volcano?

Nicolas Houlié and Jean-Paul Montagner(IPG Paris, France)

2.23.1 Introduction

Both the magma feeding system geometry and the total volume of magma injected in the volcanic edifices still remain poorly known. This constitutes one of the main limitations for a better understanding and prediction of volcanic eruptive events. However, while the existence of a magma chamber is still debated on several volcanoes, it is often observed on paleovolcanoes around the world (*Gudmundsson*, 2002). The tracking of magma in motion within the volcanic feeding system is thus a key challenge of modern volcano-seismology. The Réunion island was created by the Réunion hotspot and is the most recent island of the Mascarene chain. Piton de la Fournaise is one of the two stratovolcanoes located on the eastern part of Réunion Island (France). Following the quiescent period between 1992 and 1998, the volcano has been quasi continuously active since the March 1998 event. The quality of the erupted basalts has been constant during the last two centuries and was described as “steady state basalt” (*Albarède et al.*, 1997). The geometry of the magma feeding system is still debated. Some authors suggest that the magma feeding system is complex and composed of small magma reservoirs (*Lénat and Bachèlery*, 1990) but the large deformations of the whole volcano cannot be explained by such small subsurface sources (*Houlié*, 2005). It is now generally agreed that there is an upper magma chamber located (we will refer to this magma chamber as P2 (Aki and Ferrazzini, 2001)) at sea level (*Nercessian et al.*, 1996; *Sigmundsson et al.*, 1999; *Aki and Ferrazzini*, 2001). The volume of the upper magma chamber is estimated to be $5 \cdot 10^{-8}\ m^3$. Gravimetry measurements made along an East- West profile across the volcano have been used to locate the upper magma chamber (Lesquer, 1990). Its location is coincident with the observed seismicity (Nercessian et al., 1996; Battaglia et al., 2005). The proposed volume of the magma chamber is large enough (radius$\sim$ 500 m) to deform the whole volcano far away from the summit and west of the Enclos Fouqué, as is observed (*Houlié*, 2005). On the other hand, while the proposed size for the magma chamber is in agreement with geochemical measurements, it would be undetectable to seismic imaging. The migration of fluid coming out of this upper magma chamber and circulating inside the edifice can be detected by deformation at the surface. The use of long period (LP) or very long period (VLP) seismic events ($0.2Hz \leq f \leq 0.5Hz$) has been successfully applied to several volcanoes (Chouet, 1988) in order to investigate fluid circulation inside several volcano edifices. We present seismological evidence for a long-term response of the volcano to the deformation induced by changes in pressure inside the magma chamber located at sea level (*Houlié and Montagner*, 2007). The seismic signals are associated with the main eruptive events and recorded in the $10^{-3} - 10^{-2}Hz$ frequency range.

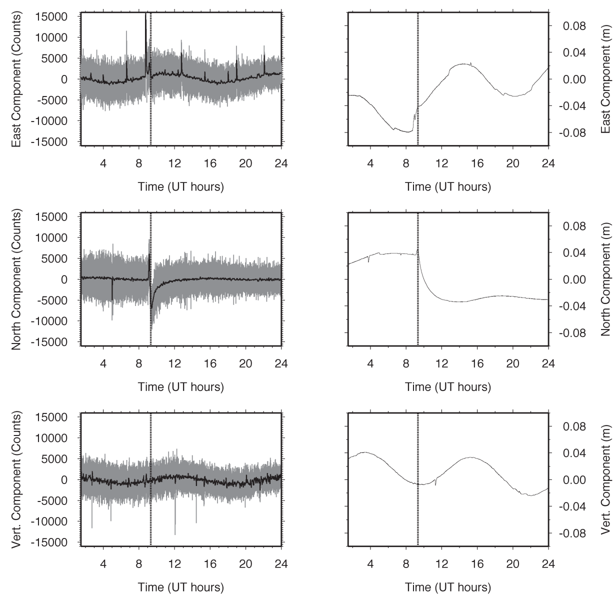

Figure 2.45: March 27th 2001. Left: GEOSCOPE data, in counts (the data are filtered by using a lowpass filter of $10^{-2}Hz$). The three components of the LH channel (the sampling rate is equal to 1 s) are plotted. A deformation is detected by the broadband seismometer on the two horizontal components of the seismogram. Right: After deconvolving the instrument response, the displacement on the Northern component is equal to $\sim 65mm$. Right column is displacement (in meters). The time of the eruptive event is indicated by a grey vertical line.

2.23.2 Results

The estimation of volume change ΔV and its location using a broadband seismometer data is still approximate in the case of the Piton de la Fournaise and the volumes estimated here are constituting an upper bound limit.We are aware that this approach is simplistic but we believe that it is justified by the fact that the Mogi’s model is still routinely used in volcano observatories to determine the pressure change in the edifice. A large number of deformation models are available in the literature (*Yang and Davis*, 1986; *Gudmundsson*, 1987). Some additional experiments will be necessary to discriminate the relative contributions of tilt and displacement during the transfer of magma out of the upper reservoir. The transient deformations extend over a region larger than 10 km across and with a typical duration of 500-1000 s. The similar pattern of deformation observed suggests that the source of the events has been stable over the last 15 yr. Large scale deformations were already suggested based on GPS benchmark time-series located on the western part of the Enclos Fouqué. We also confirm here that the EastWest displacement of the GPS benchmark 1B80 (Figure 2.46) could be related to the magma chamber pressure state and not to the slip along a discontinuity located along the border of the Enclos Fouqué, as previously suggested (*Houlié*, 2005). The GPS station located at the summit of the edifice constitutes a complementary tool to detect the long-term deformation episodes ($T > 6$ months). The GPS receivers at the summit are only sensitive to the long-term component of the deformation of the magma chamber. Due to their location above the source, their sensitivity is reduced to the vertical component accuracy of the GPS (15 mm) (*Houlié*, 2005). The variability of the signal on the eastern component of RER suggests that it might be possible to locate the source of the over/under pressure provided that an additional broadband seismometer survey takes place.

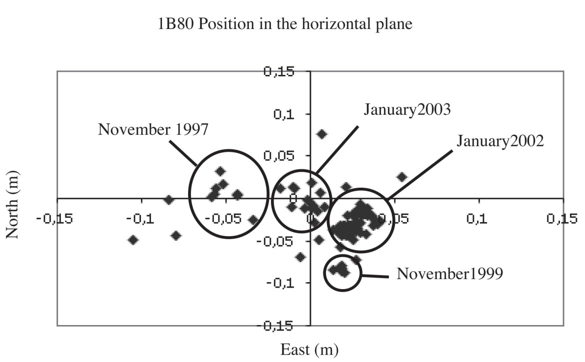

Figure 2.46: Displacement of the site 1B80 during 1997-2002 period. The shear modulus μ is estimated to be 1.95 GPa at the Piton de la Fournaise. This low value is similar to the one used in Hawaii (Rubin and Pollard, 1987) to model the injection of basalt at Kilauea volcano. Figure from Houlié (2005). Data: OVPF/IPGP.

2.23.3 References

Aki, K., Ferrazzini, V., 2001. Comparison of Mount Etna, Kilauea, and Piton de la Fournaise by a quantitative modeling of their eruption histories. J. Geophys. Res. 106 (B3), 40914102.

Albarède, F., Luais, B., Fitton, G., Semet, M., Kaminski, E., Upton, B.G.J., Bachelery, P., Cheminée, J.L., 1997. The geochemical regimes of Piton de la Fournaise volcano (Réunion) during the last 530,000 years. J. Petrol. 38, 171201.

Gudmundsson, A., 1987. Formation and mechanics of magma reservoirs in Iceland. Geophys. J. R. Astron. Soc. 91, 2741.

Gudmundsson, A., 2002. Emplacement and arrest of sheets and dykes in central volcanoes. J. Volcanol. Geotherm. Res. 116, 279298.

Houlié, N. and Montagner, J-.P., Hidden Dykes detected on Ultra Long Period (ULP) seismic signals at Piton de la Fournaise volcano, 261, 1-2, 10.1016/j.epsl.2007.04.018, *Earth Planetary Science Letters* (2007).

N. Houlié, Mesure et Modélisation de données GPS de volcans. Applications à des études de déformation à diverses échelles et à la tomographie des panaches atmosphériques., Ph.D. thesis, Institut de Physique du Globe de Paris (2005).

Nercessian, A., Hirn, A., Lépine, J.C., Sapin, M., 1996. Internal structure of piton de la fournaise volcano from seismic wave propagation and earthquake distribution. J. Volcanol. Geotherm. Res. 70, 123143.

Sigmundsson, F., Durand, P., Massonnet, D., 1999. Opening of an eruptive fissure and seaward displacement at piton de la fournaise volcano measured by radarsat satellite radar interferometry. Geophys. Res. Lett. 26, 533536.

Yang, X., Davis, P.M., 1986. Deformation due to a rectangular elastic tension crack in an elastic half-space. Bull. Seismol. Soc. Am. 76, 865881.

2.24. The Fate of the Juan De Fuca Plate: Implications for a Yellowstone Plume Head

Mei Xue and Richard M. Allen

2.24.1 Introduction

In the Pacific Northwest, the Juan de Fuca plate, a remnant of the Farallon plate, continues to subduct beneath the North American continent (Figure 2.47). To the east of the Cascadia subduction zone lies the Yellowstone hotspot track. The origins of this track can be traced back to the voluminous basaltic outpourings of the Columbia Plateau around 17 Ma (*Watkins and Baksi*, 1974; *Christiansen and McKee*, 1978). If these basalts are the result of a large melting anomaly rising through the mantle to the base of the North America continent, such as a mantle plume head, the anomaly would need to punch through the subducting Juan de Fuca slab. Here, we use teleseismic body wave travel time tomography to investigate the fate of the subducted slab and its possible interaction with a plume head.

2.24.2 Tomographic results and resolution tests

We use a dataset collected from the Oregon Array for Teleseismic Study (OATS) operating from May 2003 to May 2006. The OATS array extends northwest-southeast across Oregon from the coast to the McDemitt Caldera (Figure 2.47). The dataset was complemented by data from 9 permanent networks and a temporary deployment: Berkeley Digital Seismograph Network (BDSN), Cascade Chain Volcano Monitoring (CC), Global Seismograph Network (GSN), Laser Interferometer Gravitational-Wave Experiment (LIGO), Princeton Earth Physics Project-Indiana (PEPP), Pacific Northwest Regional Seismic Network (PNSN), USArray Transportable Network (TA), University of Oregon Regional Network (UO), the United States National Seismic Network (USNSN), and the temporary deployment of the Wallowa Mountains Experiment. A total of 52 stations were used (Figure 2.47). The data from seismic events with epicentral distance greater than 30° and magnitude 6.0 and above from July 19th, 2003 to Nov. 10th, 2004 were inspected for all stations. For the S-velocity inversion, a total of 95 events (Figure 2.47) with clear S and SKS phases were recorded at 45 stations and a total of 2148 rays were used. For the P-velocity inversion, a total of 78 events with clear P and PKiKP phases were recorded at 46 stations and a total of 2101 rays were used. We follow a similar inversion procedure as described in *Allen, et al.*, 2002.

Here we present the vertical slices through our S- and P- wave velocity models along the OATS array where both models have the highest resolution (Figure 2.48a and b). The better ray coverage available from shear-wave arrivals means the Vs model has greater resolution than the Vp model. We therefore focus on the Vs model. The most prominent feature in our tomographic models is the high velocity anomaly which dips $\sim 46°$ and extends down to a depth of ~ 400 km. We interpret this feature as the subducted Juan de Fuca plate. Resolution tests show that we are able to resolve any slab to a depth of ~ 600 km. The second prominent feature is the low velocity body immediately beneath the slab extending to a depth of at least ~ 575 km. This layer has a similar geometry as the slab: a dip of $\sim 50°$ to the east and a thickness of ~ 75 km. The amplitude of this low velocity anomaly is estimated to be up to $\sim 3\%$ for Vs. Resolution tests show that the low velocity layer is required by data and is not an artifact of the inversion.

2.24.3 Proposed tectonic model

Using the relative plate motion between the Juan de Fuca plate and the North American Plate (HS3-NUVEL1A), the estimated total length of the slab subducted to the east in the last 17 Ma is ~ 480 km. This is less than the total imaged slab length of ~ 660 km from the present trench in an east-west direction. Therefore, the bottom edge of the slab we observe today was east of the trench around 17 Ma. Assuming a similar slab geometry to today, the ~ 180 km length of slab would reach a depth of ~ 60 km, comparable to the likely thickness of the continental lithosphere. We propose that the absence of the slab below 400 km depth today is due to the arrival of the Yellowstone plume head around 17 Ma, which destroyed the Juan de Fuca slab at depths greater than the thickness of the continental lithosphere. As the plume head material would spread westward beyond the trench, possibly as far as the Juan de Fuca Ridge, traction with the subducting plate would then pull some plume head material down into the mantle. We image this material as the low velocity layer beneath the slab in our Vs model. The observed low Vs anomaly of up to 3% is comparable with what is expected for plume head material 100-300° C hotter than the surrounding asthenosphere. Finally, this hot remnant plume head material beneath the slab may be partly responsible for the absence of a Wadati-Benioff zone associated with the subduction of the Juan de Fuca plate (*Xue and Allen*, 2007).

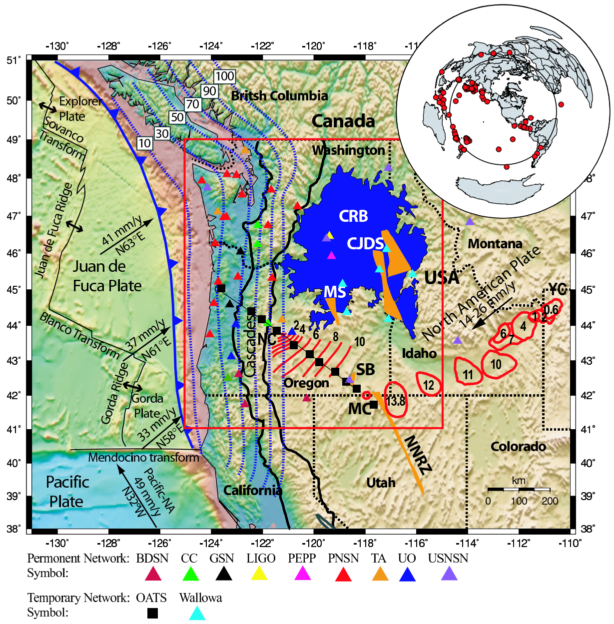

Figure 2.47: Tectonic map for the study region. Plate motions from HS3-NUVEL 1A are shown as black arrows (*Gripp and Gordon*, 2002). Blue dotted lines show the depth contours of the Juan de Fuca slab surface (*McCrory et al.*, 2006). The thick black lines delineate the Cascade Range. Age contours of initial rhyolitic volcanism along the Newberry track are shown in 1 Ma increments extending to the Newberry Caldera (NC) (*Jordan et al.*, 2004). Major rhyolitic caldera centers along the Yellowstone track are shown with age in Ma extending to the Yellowstone Caldera (YC) (*Pierce and Morgan*, 1992). Both tracks initiate in the region of the McDermitt Caldera (MC), which is shown as a red circle. The Columbia River Basalt is shown in blue (12 to 17 Ma)(*Christiansen et al.*, 2002). Dike swarms associated with the 17 Ma basaltic outpourings are shown in gold (*Camp and Ross*, 2004); *Christiansen and Yeats*, 1992): Chief Joseph Dike Swarm (CJDS), Monument Swarm (MS), Steens Basalt (SB), and Northern Nevada Rift Zone (NNRZ). The seismic stations used in this study are shown as triangles and squares with a total number of 52. Inset shows the distribution of the 95 events used in the inversion for the S-wave velocity model. The red square outlines the study region. The thick black line across OATS array indicates the location of the cross section shown in Figure 2.48

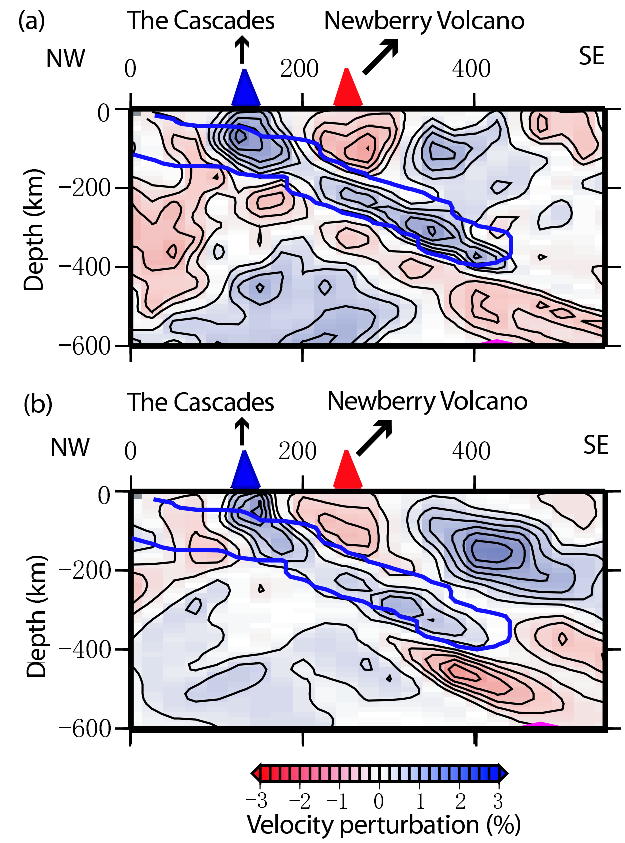

Figure 2.48: Vertical slices through the (a) Vs and (b) Vp models along the OATS line indicated in Figure 1. The envelope of the synthetic slab ending at 400 km depth is shown by the blue outline. The contour interval is 0.25% indicated by vertical lines in the color bar of the velocity scale. Zero contours are not shown. The locations of the Cascades and the Newberry Volcano are shown as blue and red triangles respectively.

2.24.4 Acknowledgements

We thank the people who assisted us in the deployment of OATS: Neal Lord, Lee Powell, Robert Pyzalski, Andrew Lockman, and William Unger from the University of Wisconsin; John Nabelek and Anne Trehu from Oregon State University, and all the land owners who hosted our stations. We thank Gene Humphreys for allowing us using data from their deployment at Wallowa Mountain. We also use data from Berkeley Digital Seismograph Network, Cascade Chain Volcano Monitoring, Global Seismograph Network, Laser Interferometer Gravitational-Wave Experiment, Princeton Earth Physics Project-Indiana, Pacific Northwest Regional Seismic Network, USArray Transportable Network, University of Oregon Regional Network, and the United States National Seismic Network.The IRIS DMC provided seismic data. This work was supported by the NSF (EAR-0539987).

2.24.5 References

Allen, R. M., et al., Imaging the mantle beneath Iceland using integrated seismological techniques, in *Journal of Geophysical Research-Solid Earth, 107*, 2325, doi:2310.1029/2001JB000595, 2002.

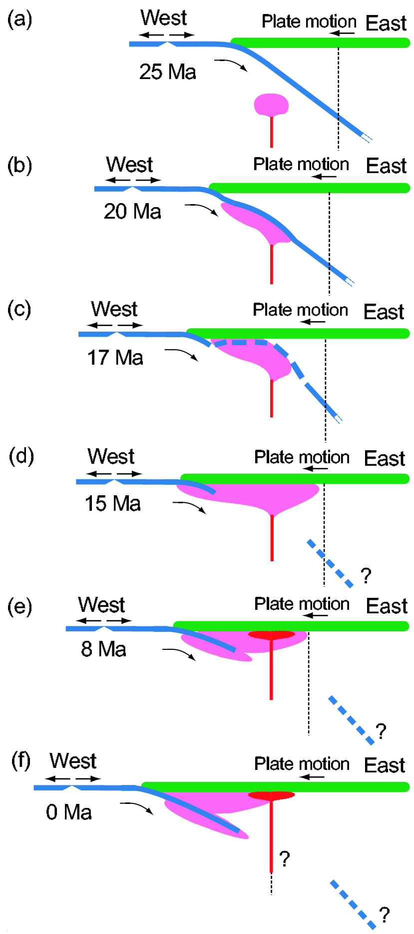

Figure 2.49: Proposed tectonic model for the interaction between the subducting Juan de Fuca Plate (blue) and the Yellowstone plume head (pink). Snapshots in time are shown as: (a) 25 Ma, the Yellowstone Plume is approaching the subducted Juan de Fuca plate; (b) 20 Ma, the plume head has intersected the Juan de Fuca plate and preferentially flowed westward along the base of the slab; (c) at 17 Ma, the plume head punched through the Juan de Fuca plate, destroyed a larger portion of the slab and caused the volcanism at the surface; (d) 15 Ma, the plume head material spreads out in a larger region at the base of the lithosphere; (e) 8 Ma, the subducting slab drags the remnant plume head material down into the mantle; (f) at present, the hot material from the remnant plume head has been brought to greater depth by the ongoing subducting slab. The vertical dashed line indicates the progression of the current Yellowstone caldera to the west. The red plume stem represents a hypothetical Yellowstone Plume since the arrival of the plume head (pink). Note: this model builds on the tectonic models proposed by *Geist and Richards*, 1993; *Pierce, et al.*, 2000.

Camp, V.E., M.E. Ross, Mantle dynamics and genesis of mafic magmatism in the intermontane Pacific Northwest, *Journal of Geophysical Research-Solid Earth 109*, 2004.

Christiansen, R.L., E.H. McKee, Late Cenozoic volcanic and tectonic evolution of the Great Basin and the Columbia intermontane regions, in: R.B. Smith, G.P. Eaton, (Eds), *Cenozoic tectonics and regional geophysics of the western Cordillera 152*, *Geological Society of America Memoir*, Boulder, Colorado, pp. 283-311, 1978.

Christiansen, R.L., G.R. Foulger, J.R. Evans, Upper-mantle origin of the Yellowstone hotspot, *Geological Society of America Bulletin 114*, 1245-1256, 2002.

Christiansen, R.L., R.S. Yeats, Post-Laramide geology of the U.S. Cordilleran region, in: B.C. Burchfiel, P.W. Lipman, M.L. Zoback, (Eds), *The Cordilleran Orogen: Conterminous U.S. G-3*, Geological Society of America, Boulder, Colorado, 261-406, 1992.

Geist, D., M. Richards, Origin of the Columbia Plateau and Snake River Plain - Deflection of the Yellowstone Plume, *Geology 21*, 789-792, 1993.

Gripp, A.E., R.G. Gordon, Young tracks of hotspots and current plate velocities, *Geophysical Journal International 150*, 321-361, 2002.

Jordan, B.T., A.L. Grunder, R.A. Duncan, A.L. Deino, Geochronology of age-progressive volcanism of the Oregon High Lava Plains: Implications for the plume interpretation of Yellowstone, *Journal of Geophysical Research 109*, doi:10.1029/2003JB002776, 2004.

McCrory, F.A., J.L. Blair, D.H. Oppenheimer, S.R. Walter, Depth to the Juan De Fuca Slab Beneath the Cascadia Subduction Margin A 3-D Model for Sorting Earthquakes, *U.S. Geological Survey, Data Series 91, Version 1.2*, 2006.

Pierce, K.L., W.J. Morgan, The track of the Yellowstone hotspot: Volcanism, faulting, and uplift, in: P.K. Link, M.A. Kuntz, P.L.B., (Eds), *Regional geology of eastern Idaho and western Wyoming 179*, *Geological Society of America Memoir*, 1-53, 1992.

Pierce, K.L., L.A. Morgan, R.W. Saltus, Yellowstone plume head: Postulated tectonic relations to the Vancouver slab, continental boundaries and climate, *USGS Open-File Report 00-498*, pp. 39, 2000.

Watkins, N.D., A.K. Baksi, Magnetostratigraphy and Oroclinal Folding of Columbia-River, Steens, and Owyhee Basalts in Oregon, Washington, and Idaho, *American Journal of Science, 274*, 148-189, 1974.

Xue, M. and R. Allen, The Fate of the Juan de Fuca Plate: Implications for a Yellowstone Plume Head, Earth and Planetary Science Letters, in Press.

2.25. Non-linear 3D Born Shear Wave Tomography in Southeastern Asia

Aimin Cao, Ahyi Kim, Mark Panning, and Barbara Romanowicz

2.25.1 Introduction

The crust and upper mantle in southeastern Asia is highly heterogeneous, presenting a challenge for path calibration, but it is well surrounded by earthquake sources, and a significant number of high quality broadband digital stations exist. Using a finite-frequency 2D approximation (NACT, Li and Romanowicz, 1995), we have already developed a 3D radially anisotropic model in a large region (longitude 30 to 150 degrees and latitude -10 to 60 degrees) from the existing long period waveform database in the range of 60 s to 400 s. The database was collected at Berkeley over the last 10 years for the construction of global mantle tomographic models (Li and Romanowicz, 1996; Megnin and Romanowicz, 2000; Gung et al., 2003; Panning and Romanowicz, 2004), and to it are added data from 20 new events in the period up to to 2005.

A data set of 38826 3-component waveforms recorded at 169 stations from 393 events was used in the waveform inversion. The data have been processed with an automated algorithm, which removes glitches and checks for many common problems related to timing, poor instrument response, and excessively noisy windows. A weighting scheme has been applied to ensure even distribution of data across the region. The model is parameterized laterally in spherical spline level 6, which corresponds to lateral resolution of $\sim$ 200 km. And the corresponding radially anisotropic model is parameterized in the spline level 5, which corresponds to a lateral resolution of $\sim$ 400 km. In this study we will use a newly developed "non-linear" 3D Born approximation (N-Born) to refine the above NACT model (Panning et al., 2007).

2.25.2 Method and Results

The N-Born is modified from the standard 3D "linear" Born approximation (Capdeville, 2005) by including a "Path Average" term. This term allows the accurate inclusion of accumulated phase shifts which arise in the case when the wavepath crosses a spatially extended region with a smooth anomaly of constant sign. The linear 3D Born terms account for single scattering effects outside of the great circle path and are modeled according to the expressions of Capdeville (2005). Accounting for scattering outside of the great circle path is the one difference with our initial NACT approach.

Because the calculation of the 3D Born sensitivity kernels is very expensive computationally, we have to select a target subregion (longitude 75 to 150 degrees and latitude 0 to 45 degrees) (Figure 2.50). In order to further reduce

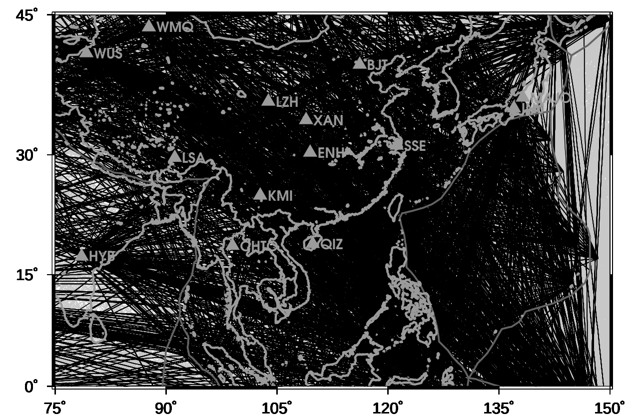

Figure 2.50: Raypath coverage in the subregion. The background grey raypath coverage is denoted for NACT and the black raypath coverage is for N-Born. Stations and events are required to be in the large region for the N-Born inversion, and so the N-Born raypath coverage is a subset of that of NACT.

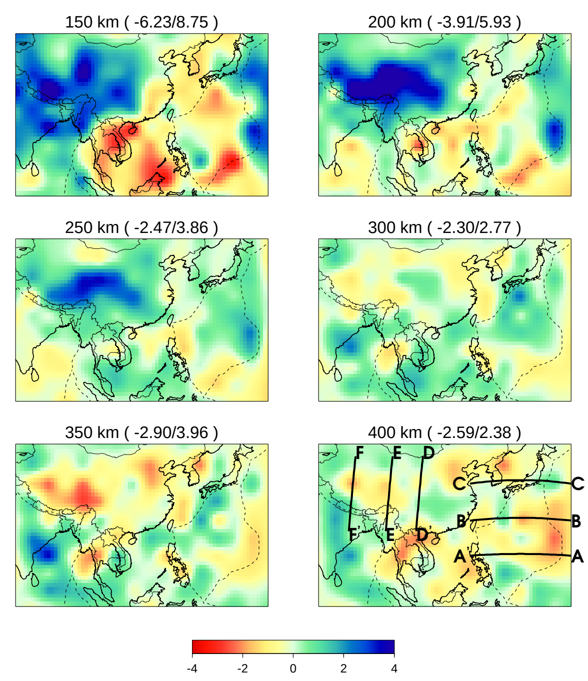

Figure 2.51: N-Born shear velocity model derived using the N-Born approximation in the subregion.

the intensity of the computation, we require that both events and stations must be in the large region, and only the ray paths along the minor arcs are selected. We calculated 3D Born sensitivity kernels for 162 events using the computing facilities (Jacquard) of the National Energy Research Scientific Computing Center (www.nersc.gov). When we generate synthetics for the N-Born inversion, we use N-Born (Panning et al., 2007) in the subregion and NACT outside of the subregion.

Our starting model is the NACT model in the large region. We expand its radially anisotropic (ξ) model from spherical spline Level 5 to Level 6, to conduct the conformal lateral parameterization for both isotropic and anisotropic inversion. We apply the N-Born approximation in the forward modeling part and calculate linear 3D Born kernels in the inverse part, and the adopted damping scheme for isotropic and radially anisotropic models is the same as that used in the NACT inversion.

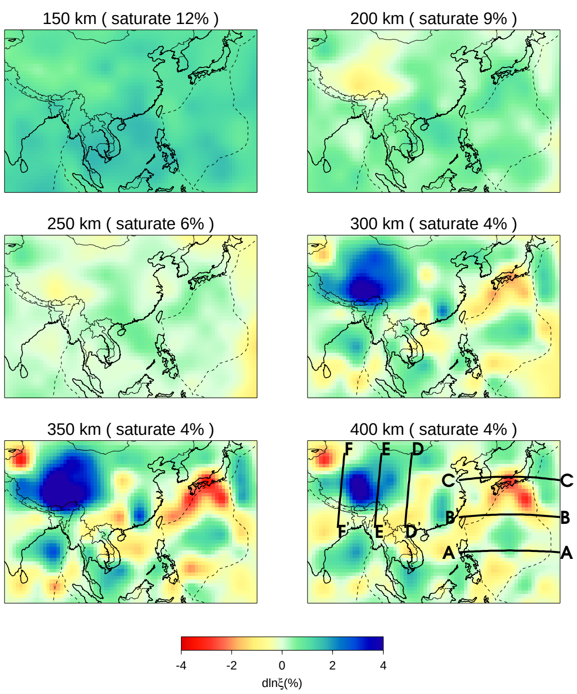

Figure 2.52: Radially anisotropic model of ξ ($\xi = \frac{V_{SH}^2}{V_{SV}^2}$) in the subregion. Values are shown relative to an isotropic model (ξ=1.0) with the anisotropy of the starting model above 220 km included. Blue regions represent regions where $V_{SH} > V_{SV}$ and red regions where $V_{SV} > V_{SH}$.

Our N-Born shear velocity isotropic and anisotropic models are shown in Figure 2.51 and 2.52, respectively. Both N-Born and NACT derived models can fit waveforms very well, with up to $\sim$ 83% variance reduction (depending on the choice of damping). While the models agree in general, there are some notable differences between them in detail. For example, beneath the Tibetan plateau, the N-Born model shows a stronger fast velocity anomaly in the depth range 150 km to 250 km, which disappears at greater depth. This indicates that there is no delamination of lithosphere beneath the plateau, as has been suggested by some authors. More importantly, the N-Born anisotropic model can recover well the downwelling structure associated with subducted slabs (e.g., around Phillippine plate) (Figure 2.51). Beneath the Tibet plateau, radial anisotropy shows $V_{SH} > V_{SV}$ (Figure 2.52) at depths of 300 km to 400 km, which implies horizontal rather than vertical flow and may help us to distinguish between end member models of the tectonics of Tibet.

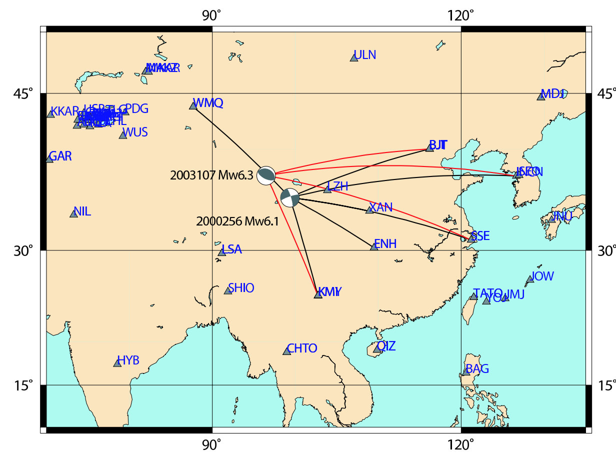

Figure 2.53: Event 2000256 (9/12/2000, Mw6.1), 2003107 (4/17/2003, Mw6.3) and IRIS station distributions. Source 2000256 (9/12/2000, Mw6.1) is used to obtain the velocity structures.

In order to refine the velocity structure beneath the region of our study, we perform forward waveform modeling with the method of frequency-wave number integration (FKI). Broadband seismograms are downloaded from IRIS and corrected to absolute ground velocity (cm/sec). We show 2 event locations of events 2000256 (9/12/2000, Mw6.1) and 2003107 (4/17/2003, Mw6.3), and the IRIS station distributions (Figure 2.53). We start with the 2000256 event, for which the continental ray paths are dominant, to obtain the 1D velocity structure between the source and each receiver. Broadband data are bandpass filtered at 0.005-0.05Hz. We used the Harvard CMT solution for the source parameters, and the starting model is a 1D layered average crustal velocity structure derived from CRUST2.0. Using the best velocity model we can obtain (Figure 2.54), we compute Green's functions and perform the moment tensor analysis for two ranges of frequency (0.01-0.05Hz and 0.005-0.03Hz). Then, we select the event 2003107, for which we have similar ray paths as for event 2000256, to perform the moment tensor analysis using Green's function obtained from our 1D simulation. We find a moment tensor solution in good agreement with the CMT solution, whereas the solution obtained using the PREM reference model is very poor. While this example was chosen because we expect that we can use Harvard CMT solutions for M>6 events as good references, this indicates that the additional regional modeling effort is worthwhile and will lead to better moment tensor solutions for smaller events in the area when we extend the modeling to higher frequencies (0.02-0.05Hz).

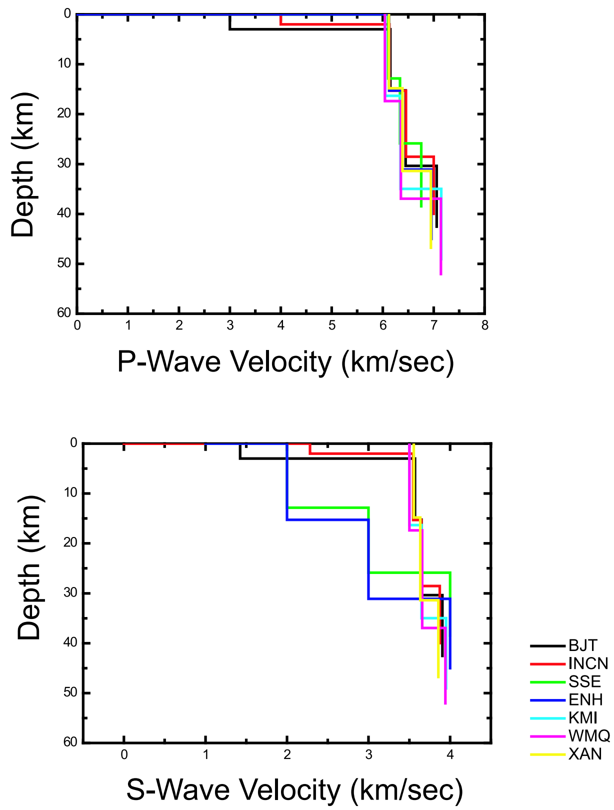

Figure 2.54: Best P-wave and S-wave velocity structures for the paths between event 2000256 and IRIS stations obtained from 1D forward modeling.

2.25.3 References

Capdeville, Y., An efficient Born normal mode method to compute sensitivity kernels and synthetic seismograms in the Earth, *Geophys. J. Int.*, 163, 639-646, 2005.

Gung, Y., B. Romanowicz, and M. Panning, Anisotropy and lithospheric thickness, *Nature*, 422, 707-711, 2003.

Li, X. D. and B. Romanowicz, Comparison of global waveform inversions with and without considering cross branch coupling, *Geophys. J. Int.*, 121, 695-709, 1995.

Li, X. D. and B. Romanowicz, Global mantle shear velocity model developed using nonlinear asymptotic coupling theory, *J. Geophys. Res.*, 101, 22,245-22,273, 1996.

Megnin, C. and B. Romanowicz, The 3D shear velocity structure of the mantle from the inversion of body, surface and higher mode waveforms, *Geophys. J. Int.*, 143, 709-728, 2000.

Panning, M. and B. Romanowicz, Inferences on flow at the base of Earth's mantle based on seismic anisotropy, *Science*, 303, 351-353, 2004.

Panning, M. and Y. Capdeville, and B. Romanowicz, Do first order 3D Born finite-frequency kernels improve modeling of surface waveforms? *Geophys. J. Int.*, submitted, 2007.

2.26. Inferring composition and temperature of the upper mantle from interpretation of long period seismic data and global attenuation measurements

Fabio Cammarano and Barbara Romanowicz

2.26.1 Introduction

Knowledge of the thermal and compositional structure of the upper mantle is essential to understanding the evolution of our planet. Direct constraints on shallow upper mantle chemical composition and temperatures are given by mineralogy and the geochemical signature of outcropping rocks. Overall, these data give a good idea of the ranges of temperatures and compositions expected in the first 200km. In general, there is a consensus that the average composition should not be far from the less depleted peridotites we sample, and therefore close to the "pyrolite" composition proposed by Ringwood (*Ringwood*, 1975). Shallow upper mantle T are consistent with those expected by a mantle adiabat with a potential T at surface of 1300^oC ($\pm 50^oC$). Also, melting conditions of peridotite rocks with depth (see, for example, the KLB1N solid curve by *Hirschmann*, 2000) are never fully reached, as indicated by seismic observations. This limits the maximum T we expect in the upper mantle. Below 200km, the best constraints on temperatures and compositions come from interpretations of seismic observations based on mineral physics. Recently, interdisciplinary studies which combine current knowledge of material properties at high P and T and geophysical observations are providing important insights into the nature of the upper mantle.

In a recent paper, (*Cammarano and Romanowicz*, 2007), we found that long period seismic waveforms require a high gradient of shear velocity between 250 and 350 km. Although some variations between continent and oceans are still seen until $\sim$ 300km, the feature we observed is clearly global and raises questions about the average thermal or compositional structure of the upper mantle. In that paper, we discussed the thermal and compositional feature based on the family of PREF models and applying a pressure and temperature-dependent Q model, developed by the previous work of one of us (*Cammarano et al.*, 2003). Also, we showed that the V_S gradient with depth would require a value of G' (i.e. the pressure derivative of shear modulus) for olivine equal to 2.5 (experimental olivine G' are between 1.2 to 1.6) to make possible to explain such a feature without modifying the thermal or compositional structure of the upper mantle and we argued that an enrichment in garnet component with depth is the most plausible explanation.

Here, we refine our interpretation by testing two thermoelastic models (PEPI03, *Cammarano et al.*, 2003 and LARS07, updated by *Stixrude and Lithgow-Bertelloni*, 2005) and the Faul and Jackson Q model (*Faul and Jackson*, 2005), discussed also in the preview report. We use the same 3-D V_S model obtained by inverting with respect to PREF, but we invert for T using the two average pyrolitic models coupled with the Faul and Jackson Q model at a given grain size and reference period at 150s. We test effects of grain size and extremely different activation volumes (V*) on the interpretation. Resulting 3-D structures are averaged and the $<Q_S>$ profile is compared with observations (the same of the previous report). Effects of variations in dry composition are tested using the LARS07 model. We model composition from harzburgite (1) to MORB (0). Pyrolite is given by a $\sim$ 17% of MORB component (0.17). In this report, we show uniquely average properties of the 3-D models.

2.26.2 Results

The two thermoelastic models for the same pyrolitic composition gave similar results in terms of thermal structure in the first 400km (Figure 2.55, second panel from the right) when coupled to the same P-T dependent Q model and assuming a given constant grain size and reference period (see Figure 2.55). Some differences between the two models appear in the first 150km. The two models differ in the transition zone as well, because of the large uncertainties on the shear properties of wadsleyite and ringwoodite. Here, we do not discuss further those features. Instead, we focus on the interpretation of the dV_S/dz gradient between 250 and 350km. Both pyrolite models (PEPI03 and LARS07) imply a negative thermal gradient to explain the V_S model required by seismic data (Figure 2.55). However, the consistent average Q structure predicted by those models attains very high values around 350km (Figure 2.55, third panel from the right) and we tested that the resulting $<Q>$ model is not consistent with the seismically observed global attenuation. Reducing the grain size, as expected, has the overall effect of reducing the temperatures to explain the same V_S structure, but the thermal gradients stay almost the same. We tested that even for a constant grain-size of 1mm, the resulting Q is still too high ($Q_S \sim 450$) for both thermoelastic models at 350 km. The average density and V_P structures that are consistently determined by the mineral physics models are also plotted in Figure 2.55. The observed discrepancies are due to the different relative variations of V_S compared to density

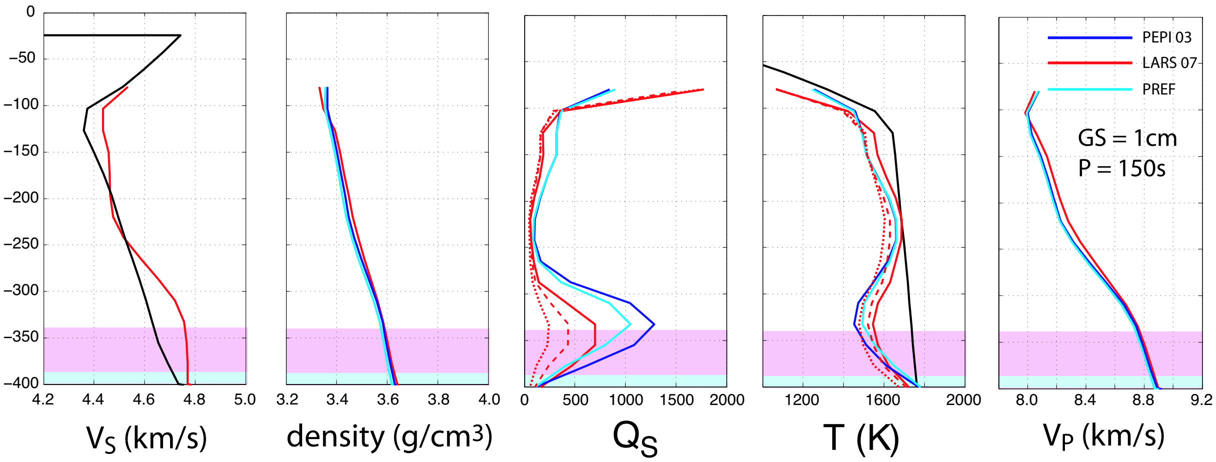

Figure 2.55: Comparison of thermal interpretation using PEPI03 and LARS07 pyrolitic models plus P-T and GS dependent Q model. Solid lines refer to GS=1cm, dashed for GS=1mm and dotted $V* = 0.6 \times 10^{-5}$. Color scheme is given in the legend. Reference period is 150s. Starting V_S and thermal (adiabatic) model are in black

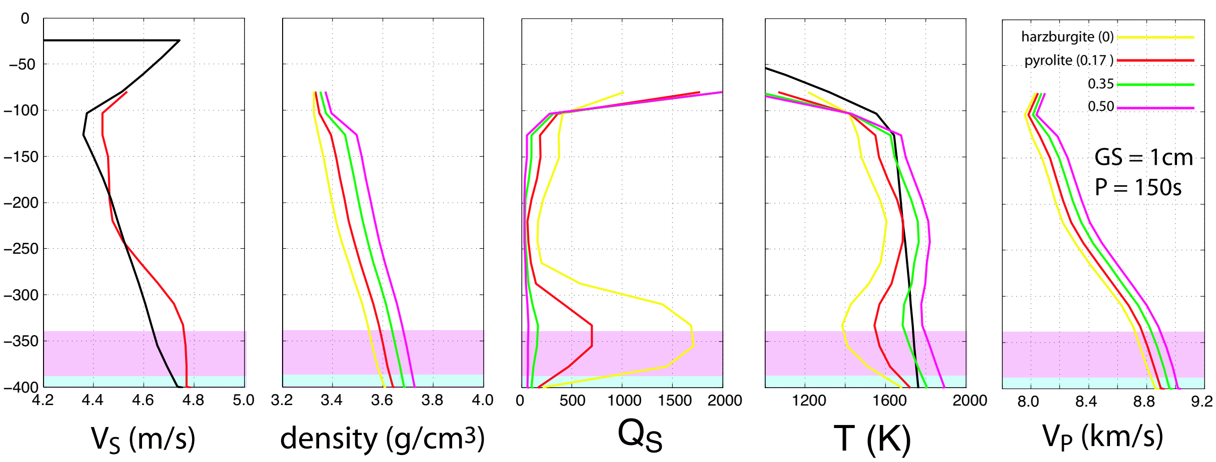

Figure 2.56: Comparison of thermal interpretation for 4 different compositions using LARS07 model plus P-T and GS dependent Q model at constant GS of 1cm and reference period of 150s. Color scheme is given in the legend. Starting V_S and thermal (adiabatic) model are in black

and V_P (heterogeneity ratios) between the two mineral physics models. Note, however, that variations in density are extremely small compared to the variations expected when interpreting the same $<V_S>$ model with variations in composition (compare density panels in Figure 2.55 and 2.56). We do not plot the similar indirect effects on V_P and density for a thermal interpretation when using different grain sizes. Alternatively to the discussed negative thermal gradient, an increase in grain size has been invoked to explain the isotropic features below 250km (*Faul and Jackson*, 2005). In our case, we found that such explanations would get a $<Q_S>$ structure that does not fit the seismic observations. The largest variations in thermal interpretation are obtained when varying the pressure dependence of the Q model, i.e. the activation volume V* (see also previous report). For example, by using a $V* = 0.6 \times 10^{-5}$, we found that a thermal explanation characterized by an overall cold upper mantle ($< T >\sim 1500K$) and a negative thermal gradient below 250km is now feasible. In spite of the low average T, the low V* keeps the Q_S values small enough in hot areas to get a $<Q_S>$ consistent with observed seismic attenuations (Figure 2.55). Note, however, that Q_S values may be too low at some depths (~ 20) compared to what is inferred seismically. In Figure 2.56, we show the different thermal interpretation using the LARS07 model for 4 compositions. If we assume an adiabatic 1300^oC geotherm, it is possible to explain the V_S gradient with a compositional variation with depth. The required compositional gradient may be estimated visually by looking at what depth the thermal profiles for different compositions cross the mantle adiabat (Figure 2.56). We observe an increase from 17% of MORB component mixed with harzburgite (that is the value of an average pyrolite) at 250km until 35% at $\sim$ 350km.

2.26.3 Conclusions

The combination of uncertainties on elastic and anelastic properties of mantle minerals together with long period seismic data and observed global attenuation measurements provide an important constraint on the nature of the upper mantle above 400km depth. In a previous paper, we found that adiabatic pyrolite is not compatible with seismic observations. One of the most striking features that is not reconcilable with such simple structure is the high V_S gradient we found globally below 250km (*Cammarano and Romanowicz*, 2007). Here we refine our interpretation by adding testing of predicted $<Q_S>$ structures against observations and investigating the effects of two mantle thermoelastic models. We found that a purely thermal interpretation would be possible only for low values of activation volume in order to be compatible with the $<Q_S>$ measurements and would imply a cold UM ($T \sim 1500K$) and a negative thermal gradient below 250km, on average, at the global scale. A compositional explanation, more dynamically feasible in our opinion, would be more consistent with an adiabatic (potential T of 1300^oC) thermal structure and predicts a significant enrichment in garnet component with depth. By using the Stixrude 2007 model, we estimate a doubling of MORB component with respect to pyrolite around 350km depth. Test on the dynamical evolution of this C or T structure and other studies on 3-D Q structure and including constrain from density are required to clearly discriminate between the two possibilities.

2.26.4 References

Cammarano F., Goes S., Vacher P. and Giardini D., Inferring upper mantle temperatures from seismic velocities, *PEPI*, 138, 197-222, 2003.

Cammarano F. and B. Romanowicz, Insights into the nature of the transition zone from physically constrained inversion of long-period seismic data, *PNAS*, 104, 9139-9144, 2007

Faul, U.H., and I. Jackson, The seismological signature of temperature and grain size variations in the upper mantle, *Earth Planet. Sci. Lett.*, 234, 119-134, 2005.

Hirschmann, M.M., Mantle solidus: experimental constraints and the effects of peridotite composition., *Geochem. Geophys. Geosyst.*, 1, paper 2000GC000070, 2000.

Ringwood, A.E., Composition and Petrology of the Earth's Mantle, McGraw and Hill, New York, 1975.

Stixrude, L. and C. Lithgow-Bertelloni, Thermodynamics of mantle minerals: 1. Physical properties, *Geophys. J. Int.*, 162, 610-632, 2005.

2.27. Q Constraints on Upper Mantle Temperature

Fabio Cammarano and Barbara Romanowicz

2.27.1 Introduction

Imperfections in the crystalline structure of any mineral govern deformation and viscoelastic relaxation (anelasticity) at seismic frequencies. The study of different creep mechanisms and their mutual relevance at different P-T conditions (e.g., *Frost and Ashby* 1982) is useful in understanding the possible physical mechanisms that may also be responsible for seismic attenuation (i.e. at much higher frequencies). Recently, accurate experimental data of shear attenuation for mantle minerals at seismic frequencies (e.g., *Jackson et al.* 2002) are starting to provide a better understanding of such phenomena. A grain-boundary sliding mechanism seems compatible with laboratory experiments. Temperature and grain-size dependence for olivine polycrystalline samples have been accurately measured and modeled (*Faul and Jackson*, 2005). Pressure dependence, represented by activation volume, remains mostly unknown, however.

Within the Earth, viscoelastic relaxation causes dissipation and dispersion of seismic waves, or what is commonly referred to as intrinsic attenuation. Seismic attenuation mostly affects the amplitude of the waveforms. However, other effects related to the 3-D elastic structure of the Earth (focusing, scattering) and noise in the data make it difficult to retrieve information on the intrinsic attenuation structure of the Earth (see for a review, *Romanowicz*, 1998). Nevertheless, observations of attenuation of free oscillation and surface waves constrain the radial (1-D) attenuation profile of the Earth's upper mantle well enough , in spite of the well known discrepancy between the two datasets.

Here we use the modified Burgers model defined by *Faul and Jackson* (2005) to predict the quality factor (Q_S) for a range of simple thermal and grain-size structures for the shallow upper mantle (down to 400 km). We assume the QL6 (*Durek and Ekström*, 1996) attenuation profile below that depth. We computed the Q_S values as a function of harmonic degree for fundamental and overtone spheroidal and toroidal modes, assuming a background reference velocity model. We found no distinguishable effects when testing two alternative velocity models (PREM *Dziewonski and Anderson*, 1980 and inverted PREF *Cammarano and Romanowicz*, 2007), indicating a weak sensitivity to the background velocity model used. We compared predicted values with seismic observations. Here, we show only comparisons with fundamental spheroidal modes (0S). We used five different compilations (see figure 2.58) based on attenuation of free oscillations and surface waves. Note that we do not consider here the discrepancy between the two types of observations. We defined a misfit function as

$$\frac{1}{N_\ell}\sum_{\ell=1}^{N_\ell}\left|\frac{q_o-q_s}{q_o}\right| \tag{2.5}$$

and we computed the total misfit for each given structure. Consistent with the frequency of surface waves, we used a reference period of 150s in the computations of Q_S profiles with the Faul and Jackson model. The frequency dependence determined by their work is 0.27. Choosing a different period, within the band of surface waves, has a secondary effect on fitting observations compared to the unconstrained pressure dependence, as we shall discuss later.

2.27.2 Results

In order to highlight the characteristics of the trade-off between grain size and temperature, we show in figure 2.57 (top panel), the misfit values for isothermal structure from 100 to 400km for various constant grain sizes. We found that Q_S observations are much more sensitive to T than grain size, as shown by the contour lines in figure 2.57. Note that the "cold" structure of the lithospheric part does not affect measurements significantly. Indeed, we test that a negligible variation of the misfit pattern is obtained when using a standard 60My old oceanic geotherm for all thermal structures in the first 80km, plus a linear gradient in the 20km below to join the isotherms. The average temperature ($< T >$) of the upper mantle is very well constrained by seismic observations for a given grain size. For example, we found that a 1 mm grain size requires $< T >\sim$1500K, while a higher temperature ($\sim$1600K) is required around 1cm and slightly increases with coarser grain sizes. Subsequently, by giving a reference temperature at 100km of 1600K, more or less consistent with the temperature expected from a 60my old oceanic geotherm at that depth, we tested linear temperature gradients down to 400km, from -1.5 $^o/km$ to 1.5 $^o/km$, for various grain sizes (middle panel of figure 2.57). Again, we found that observations are able to discriminate between different thermal gradients with depth at given grain sizes. In general, positive gradients are required at grain sizes > 1cm, while negative ones are preferred for millimeter grain-sizes. There is an obvious trade-off, here not shown, between the Tref(100km) and the gradients below. A reference temperature of 1700K at 100km will be more compatible with positive thermal gradients. In particular, we found that an adiabatic 1300^oC temperature is compatible with observations at

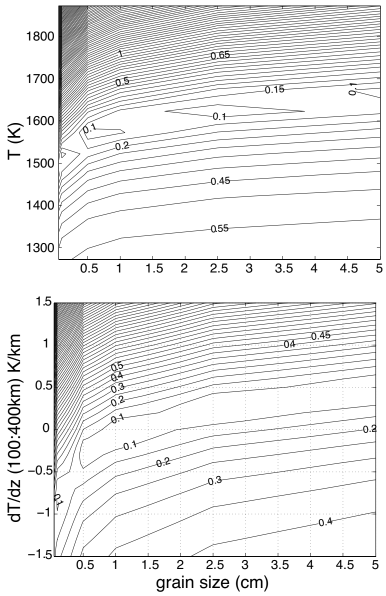

Figure 2.57: Misfit values to 0S attenuation measurements for isothermal, constant grain-size upper mantle structure (right panel) and for linear thermal gradients from 100 to 400km (left panel). For left panel, reference temperature at 100km is 1600K. Q_S values are computed at period of 150s

1cm constant grain size. In figure 2.58, we give an example of Q_S depth profiles (top panel) and their predicted attenuation as a function of harmonic degree compared to 0S measurements (bottom panel) for one best-fit model (grain size=2.5cm, dT/dz(K/km)=0.2, total misfit to 0S attenuation measurements equal to 0.06) and one poorly fitting model (GS=2.5cm and dT/dz=0.8, misfit = 0.32). Note that because of the discrepancy between seismic observations, we are able to reach only minimum values of misfit equal to 0.06. In general, Q models based on T and GS structures do not have the first-order jump that characterizes seismic models around 220 km depth. Nevertheless, the fit to attenuation measurements can resolve between our different models. This preliminary result seems to point out that the constant increase in Q_S due to change in T or GS is sufficient to first order. Large uncertainties exist on the activation volume (V*). We tested the extreme values provided by Faul and Jackson, i.e. 0.6 and 2×10^{-5}, compared to 1.2×10^{-5} used in the model. Low values of V* require negative thermal gradients, if Tref at 100km is set to 1600K. Conversely, very positive thermal gradients with depth are consistent with a high V*. We anticipate that, in spite of the limitation imposed by V* to interpret Q seismic observations, when P,T, GS dependent models are used together with elastic data at high P and T of mantle minerals for the interpretation of seismic data, we will be able to provide more constraints on the temperature and composition structure of the upper mantle (see *Cammarano and Romanowicz* 2007 and 2.26..

2.27.3 References

Cammarano F. and B. Romanowicz, Insights into the nature of the transition zone from physically constrained inversion of long-period seismic data, *PNAS*, 104, 9139-9144, 2007

Durek J.J. and G. Ekstrom, A radial model of anelasticity consistent with long period surface-wave attenuation, *Bull. Seis. Soc. Amer.*, 86, 144-158, 1996.

Dziewonski A.M. and D.L. Anderson, Preliminary reference Earth model, *Phys. Earth Planet. Int.*, 25, 297-356, 1981.

Faul, U.H., and I. Jackson, The seismological signature of temperature and grain size variations in the upper mantle, *Earth Planet. Sci. Lett.*, 234, 119-134, 2005.

Frost H.J. and M.F. Ashby, Deformation-Mechanism Maps: The Plasticity and Creep of Metals and Ceramics,166 pp.Oxford: Pergamon Press, 1982.

Jackson I., J.D. Fitz Gerald, U.H. Faul and B.H. Tan Grain size sensitive seismic wave attenuation in polycrystalline olivine, *J. Geophys. Res.*, 107, B122360, 2002.

Romanowicz B., Attenuation tomography of the earth's mantle: A review of current status, *Pure and Applied Geophysics*, 153, 257-272, 1998.

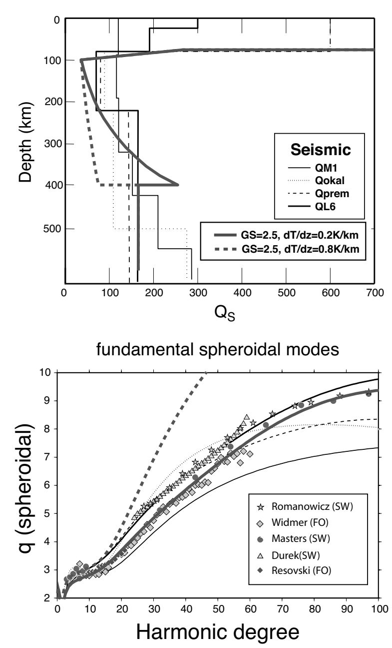

Figure 2.58: Examples of a good (solid red line) and a bad fit model (dashed).q is $1000/Q_S$. See text for details

2.28. Applying the Spectral Element Method to Tomography: Crustal Effects

Vedran Lekic and Barbara Romanowicz

2.28.1 Introduction

Crustal structure is characterized by large variations in topography/bathymetry of the surface and Moho, as well as by crustal velocity variations. While long period surface waves can be strongly affected by crustal structure, they lack the depth resolution necessary to constrain crustal thickness and velocity. Therefore, models of seismic velocities in the mantle depend on correcting the observed seismic waves for the effects of propagation through the crust. Typically, the effects of the crust are considered within the framework of normal mode summation and first order perturbation theory. One method, called the path average approximation (PAVA: *Woodhouse and Dziewonski*, 1984), assumes that the wave is only sensitive to structure along the great circle path joining the source with the receiver, and that this sensitivity is only a function of depth. Higher-order asymptotic approaches, such as non-linear asymptotic coupling theory (NACT: *Li and Romanowicz*, 1995), are capable of more accurately modeling the wave's actual sensitivity within the plane defined by the great circle path. However, in both approaches, the effects of crustal velocities are most often neglected, while the variations in Moho topography are considered as perturbations from an average Moho depth. On the other hand, the coupled Spectral Element Method (cSEM: *Capdeville et al.*, 2003) is capable of fully accounting for 3D wave propagation through structure. Figure 2.59 illustrates that the differences between synthetic seismograms calculated using cSEM and NACT in a PREM mantle and realistic crustal structure can be large, especially on the transverse component. We explore the contamination of elastic models of the mantle that can result from such inadequacies in the forward modeling of crustal effects.

2.28.2 Synthetic Tests

In order to quantify the contamination of mantle models that can arise from the use of linear crustal corrections, we carry out a series of synthetic tests. Starting with PREM (*Dziewonski and Anderson*, 1981) and Moho topography and crustal velocities from CRUST2 (*Bassin et al*, 2000), we use the cSEM to generate a synthetic dataset of long-period (60 - 400 sec) transverse component waveforms for a set of 41 earthquakes and a realistic station distribution. Though restricted to first-orbit phases, the dataset provides good fundamental-mode and overtone coverage throughout Asia and the westernmost Pacific. Using the PAVA and NACT waveform modeling techniques, we correct the synthetic dataset for crustal effects of CRUST2. We then invert the residual seismograms – which would ideally be very small – for mantle structure. Any retrieved mantle structure is contamination resulting from unmodeled crustal effects.

Figure 2.60 shows variations of isotropic shear speed obtained from an inversion of fundamental mode surface waves and overtones. The model explains 90 percent of the variance in the residual seismograms. Note the strong tectonic character of the mantle contamination. Mantle structure is artificially slow beneath continents, where linear crustal corrections underpredict the effects of crustal structure. Models developed using only transverse component higher modes and only fundamental mode surface waves are nearly identical to the model in Figure 2.60. Significant contamination of mantle structure extends to 100 km depth. Beneath Tibet, structure is different from surrounding mantle at a depth of 200 km.

In order to determine whether the contamination of mantle structure is the result of vertical smearing, we increase the depth parameterization by 5 cubic splines in the upper mantle – 2 in the crust. The retrieved model is substantially similar to that obtained previously, indicating that the mantle contamination is a feature of the waveforms, and not imposed by the parameterization.

Confronted with significant artifacts in mantle structure at depths as great as 200 km, we explore ways of compensating for the inadequacies of linear crustal corrections and minimizing the resulting contamination. Inversion for Moho and seafloor topography/bathymetry has been used in the construction of several global models (e.g. *Mégnin and Romanowicz*, 2000). Therefore, we invert for mantle velocity structure and Moho and seafloor topography simultaneously. The resulting model shows no significant contamination in the mantle while explaining the data as well as the model shown in Figure 2.60. However, the retrieved Moho and seafloor perturbations are inherently unphysical, since they result from inadequacies of linear crustal corrections and effects of 3D propagation in a laterally inhomogeneous crust.

2.28.3 Conclusion

Using a synthetic dataset of long period fundamental and high mode waveforms, we have quantified the contamination of mantle structure arising from the use of linear crustal corrections, which are inadequate at modeling the effects of crustal structure on waveforms, especially for the transverse component. Models derived using approximate forward modeling techniques may suffer from

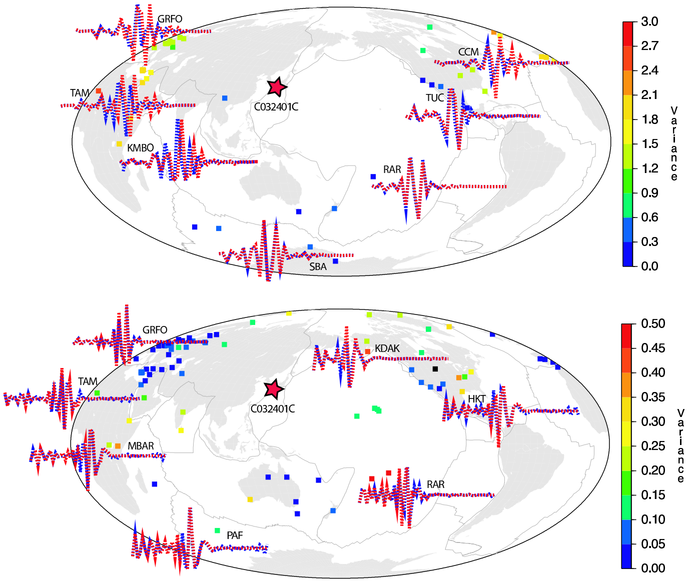

Figure 2.59: SEM (red) and NACT (blue) synthetic seismograms for the transverse (top) and vertical (bottom) component computed in a PREM mantle and a realistic crustal structure. The star denotes the event while stations squares are colored according to variance between the two synthetics.

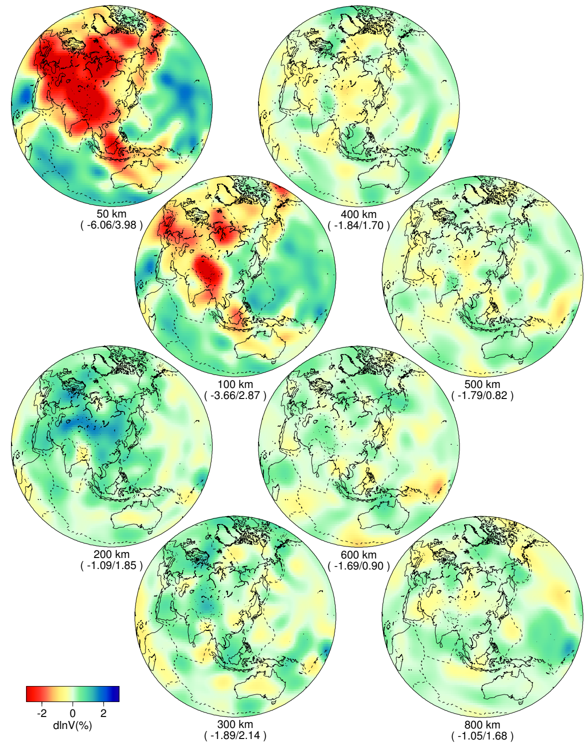

Figure 2.60: Isotropic shear wave speed model derived from synthetic transverse-component long-period fundamental mode surface wave and overtone waveforms. The starting model is a 1D mantle model with 3D crustal structure.Note the depth extent and tectonic nature of the retrieved artificial structure Accounting for perturbations in Moho topography in the inversion removes this contamination.

artifacts at depths of 0 - 100 km. that arise from unmodelled crustal effects. Under Tibet, the contamination may extend to 200 km. These artifacts can be eliminated by inverting for Moho and seafloor topography/bathymetry; however, the retrieved perturbations are unphysical. In this study, we have examined the effects of linear crustal corrections, in which a single set of kernels is used. A much more accurate, though computationally heavy, approach involves non-linear crustal corrections, in which laterally varying structure kernels are considered along each path (e.g *Montagner and Jobert*, 1988).

2.28.4 Acknowledgements

This research was supported by National Science Foundation grant NSF/EAR-0308750 and a National Science Foundation Graduate Fellowship held by VL.

2.28.5 References

Bassin, C., Laske, G. and G. Masters, 2000. The Current Limits of Resolution for Surface Wave Tomography in North America. *EOS Trans AGU 81,* F897.

Capdeville, Y., E. Chaljub, J.P. Vilotte and J.P. Montagner, 2003. Coupling the spectral element method with a modal solution for elastic wave propagation in global Earth models. *Geophys. J. Int., 152,* 34-66.

Dziewonski, A.M. and D.L. Anderson, 1981. Preliminary reference Earth model. *Phys. Earth and Planetary Int., 25,* 297-356.

Li, X.D. and B. Romanowicz, 1995. Comparison of global waveform inversions with and without considering cross-branch modal coupling, *Geophys. J. Int., 121,* 695-709.

Montagner, J.-P. and N. Jobert, 1988. Vectorial tomography, II, Application to the Indian Ocean. *Geophys. J. R. Astron. Soc. 94,* 309-344.

Megnin, C. and B. Romanowicz, 2000. The three-dimensional shear velocity structure of the mantle from the inversion of body, surface and higher-mode waveforms. *Geophys. J. Int., 143,* 709-728.

Woodhouse, J.H. and A.M. Dziewonski, 1984. Mapping the upper mantle: three dimensional modeling of Earth structure by inversion of seismic waveforms. *J. Geophys. Res. 89,* 5953-5986.

2.29. Travel time analysis of Sdiff, SKS and SKKS phases

Akiko To and Barbara Romanowicz

2.29.1 Introduction

Global shear velocity tomographic models show two large-scale low velocity structures, so-called superplumes, in the lower mantle, under Africa and under the mid-Pacific. Sharp lateral velocity changes have been documented for some parts at the borders of the superplumes (e.g. *Wen*, 2001, *To et al.*, 2005, *He et al.*, 2006). We evaluate the distribution and amplitude of the anomalies given by a tomographic model for the D" layer around the Pacific region by measuring travel times of Sdiff, SKS and SKKS phases. We search for sharp lateral velocity changes, which have not been found yet, at the borders and also inside, according to tomographic models, the superplume.

2.29.2 Distribution of the measured Sdiff travel times

We collected 1796 SKS, 1729 SKKS and 3861 Sdiff travel times which sample the Pacific region. In order to measure the travel time anomalies, synthetic waveforms from the 1D model (PREM) are first created for each trace. The anomalies are obtained by taking the cross correlations between PREM synthetic and observed waveforms. The waveforms are bandpass filtered between 100 and 17 second.

Figure 2.61(a) shows a distribution of measured Sdiff travel time anomalies with respect to PREM. Travel time anomalies are plotted at the midpoints of the diffracting portions of the Sdiff phases. The anomaly distribution has a good correlation with the tomographic model in the D" layer. The figure indicates that the S wave structure in the D" layer primarily contributes to the observed Sdiff anomalies.

Figure 2.61 (b) through (d) show the Sdiff travel time anomalies with respect to azimuth or back azimuth for some selected events or stations. Observed travel times of SKS and SKKS phases and synthetic travel times of Sdiff, which are calculated by ray theory, are also plotted. Lack of correlations of the travel time anomalies between Sdiff and other phases indicates that the Sdiff travel time anomalies are due to heterogeneities within the lower mantle. This is because the paths of Sdiff and SKKS are close to each other in the upper mantle but they are different in the lowermost mantle. The paths of SKS and Sdiff are more separated compared to Sdiff and SKKS in the upper mantle; however, the lack of correlation between SKS and Sdiff travel time anomalies can still indicate if the Sdiff anomalies are caused by near source or station structure or the lower mantle structure.

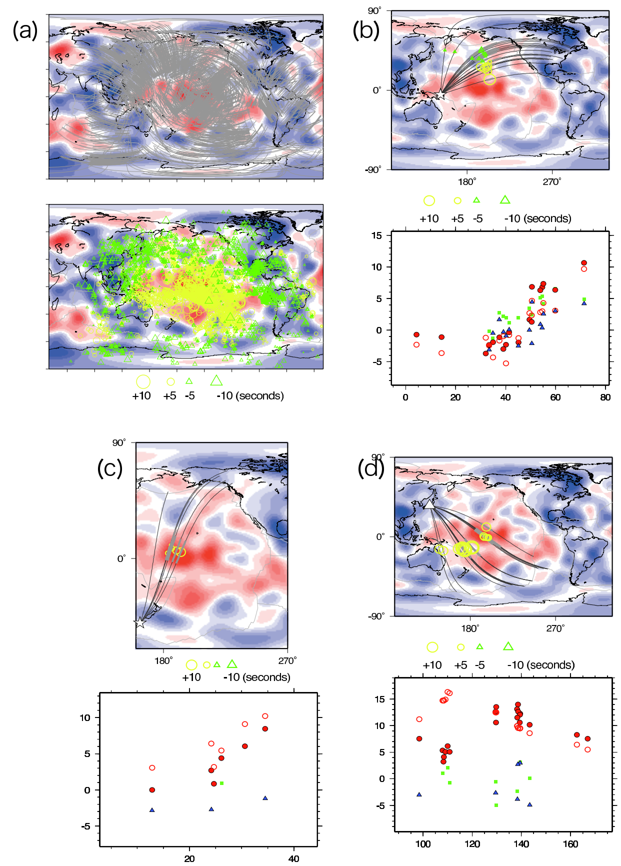

Figure 2.61: (a) Top panel: Distribution of diffracting portion of all the Sdiff paths whose travel time anomalies are measured. The background model is SAW24B16 (*Mégnin and Romanowicz*, 2000) at the depth of 2850km. Bottom panel: Sdiff travel time anomalies with respect to PREM is plotted at the midpoint of the paths. (b) (c) (d) Top panel: Sdiff travel time anomalies are plotted at the midpoint of the path. Diffracting portion of Sdiff waves are shown in thick gray lines. The back ground model is SAW24B16. The event locations are shown by a stars. The station locations are shown by triangles. Bottom panel: Travel time anomalies of Sdiff (solid red circle), SKS (blue triangle) and SKKS (green square) phases with respect to azimuth or back azimuth. Synthetic travel time anomalies obtained by 1D ray theory for SAW24B16 are shown by open red circles.

Figure 2.61 (b) shows that trends of Sdiff travel time anomalies are well predicted in the Northern Pacific. The paths sample the border of the Pacific superplume. We have previously reported that ray theory gives larger positive travel time anomaly estimations compared to a more exact method, such as the spectral element method, because of the lack of the finite frequency effects. With the finite frequency corrections, the positive anomalies of synthetic travel times become a few seconds smaller from what is shown in the figures. Figure 2.61(c) shows the data set with a rather steep change in Sdiff travel time anomalies with respect to azimuth, observed in the central Pacific. The paths sample inside the Pacific superplume. They indicate a possibility that the superplume is a gathering of multiple separated slow regions rather than a single big blob. Figure 2.61(d) shows one of the cases where the model over predicts the travel time anomalies.

2.29.3 Acknowledgements

The data were downloaded from IRIS DMC and CNSN.

2.29.4 References

Mégnin, C. and B. Romanowicz, The three-dimensional shear velocity structure of the mantle from the inversion of body, surface and higher-mode waveforms, *Geophys. J. Int.*,**143**, 709-728, 2000.

He, Y., Wen, L., and Zheng, T., Geographic boundary and shear velocity structure of the "Pacific anomaly" near the core-mantle boundary beneath western Pacific, *Earth Planet. Sci. Lett.*, **244**, 302-314, 2006.

To, A., B. Romanowicz, Y. Capdeville and N. Takeuchi, 3D effects of sharp boundaries at the borders of the African and Pacific Superplumes: observation and modeling, *Earth and Planet. Sci. Lett.*,**233**, 137-153, 2005

Wen, L., Seismic evidence for a rapidly varying compositional anomaly at the base of the Earth's mantle beneath the Indian Ocean, *Earth Planet. Sci. Lett.*, **194**, 83-95. 2001.

2.30. Locating Scatterers in the Mantle Using Array Analysis of PKP Precursors from an Earthquake Doublet

Aimin Cao and Barbara Romanowicz

2.30.1 Introduction

PKP precursors were first observed in the 1930's [*Gutenberg and Richter*, 1934], but it has taken more than sixty years to establish their origin. Array analyses of arrival times, slownesses, and spectra [*Cleary and Haddon*, 1972] have suggested that these precursors are scattered waves from the lower mantle rather than diffracted, reflected, or refracted waves from the core. Global simulations under the single and multiple scattering hypotheses have determined that small-scale, weak ($<\sim 1\%$) heterogeneities distributed throughout the mantle likely contribute to the PKP precursor wave-trains, with perhaps a concentration in the lowermost mantle [*Hedlin et al.*, 1997].

Small-scale heterogeneities have important geodynamic significance in mantle convection. In particular, subducted slabs can survive for billions of years in the lower mantle due to incomplete mixing, and so regional distributions of small-scale heterogeneity in subduction or upwelling zones might help us sketch out local depth ranges of the mantle flow field and understand better the distribution and nature of heterogeneity. Given the fact that current resolution provided by seismic tomography is not high enough to image structures at scales of $\sim 1-10km$, locating and estimating the size and strength of individual scatterers responsible for PKP precursors provides a potential complementary approach.

Recent studies have derived general properties of the PKP precursor field from the analysis of high quality data from the global seismic network or from large aperture seismic arrays. The large aperture of the arrays considered prevented the use of standard array processing techniques such as the construction of vespagrams. Even when considering stacks across small-aperture arrays such as Norsar, these studies have primarily modelled stacks of the envelopes of the precursor train, and only in a statistical sense. In most cases, these authors have invoked the presence of partial melting associated with Ultra Low Velocity zones to interpret the large velocity contrasts ($\sim 10\%$) necessary to explain the observed precursor amplitudes.

However, very few studies have attempted to locate individual scatterers in the mantle, because PKP precursors are usually weak and their arrivals overlap. Doornbos [1988] tried to locate the scattering regions using the NORSAR seismic array, but he pointed out that the uncertainty in the precursor slowness measurements was unknown. The arrival time of the onset of the precursor train has also been used to try and locate the region of observed strong scattering. An added complication comes from the fact that there is ambiguity between source and receiver side scattering. In general, this is resolved indirectly, by comparing paths in different azimuths from the source or receiver side, and proposing an interpretation most compatible with all observations. *Hedlin et al.* showed that the ambiguity can be resolved in many regions of the lowermost mantle by inverting a global dataset of precursor average power estimates, in the framework of Rayleigh-Born scattering theory. Finally, even if the slowness and back-azimuth of a precursor can be precisely estimated using a small-aperture seismic array, it is also necessary to know if the precursor was scattered from PKPbc or PKPab on the receiver side or on the source side, in order to uniquely estimate the latitude, longitude, and depth of the corresponding scatterer. Since the amplitude of PKPbc is generally much larger than that of PKPab, it is often assumed that most of the scattering originates on the bc branch. However, until now, it was not possible to demonstrate that explicitely.

Doublet events, for which hypocenters, moment tensors, and source time history are basically identical, provide a powerful means to estimate repeatability of measurements of precursor slowness and back-azimuth. Fortunately, a very high quality earthquake doublet was reported recently [*Zhang et al.*, 2006]. Highly similar waveforms were recorded at 102 stations with a broad coverage of epicentral distances and azimuths, and the hypocenter separation of the two events was estimated to be less than $1.0km$. Further evidence of the unique quality of this doublet was obtained from the analysis of PP phases, which have identical waveforms in a time interval of at least 70 sec, and well into the PP coda. In this paper, we use this doublet to conduct array analyses of PKP precursors. Taking advantage of an effective stacking technique, we obtain clear and isolated doublet PKP precursors (Figure 1), which, we will argue, originate from individual scatterers in the mantle. The stability of the estimated slowness and back-azimuth enable us to obtain reliable locations of several of these scatterers in the lower mantle.

2.30.2 Data and Results

The high quality short-period Yellowknife Seismograph Array (YK) is a long-term primary array in the International Monitoring System (IMS) seismic network, act-

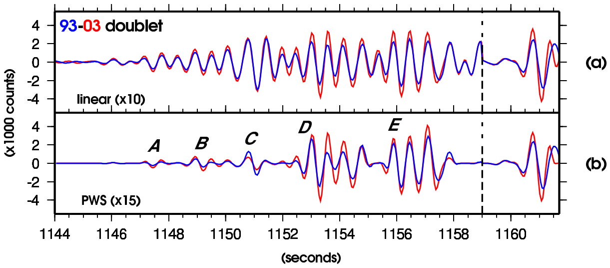

Figure 2.62: Stacked waveforms of 1993 (blue) and 2003 (red) doublet events filtered between 1 and 2 Hz. (a) Linear stack ing. Waveforms before the dashed line are amplified 10 times. PKP precursor train is apparent, but all precursors are mixed together. (b) Phase Weighted Stacking (PWS). Waveforms before the dashed line are amplified 15 times. Individual precursors A, B, and C stand out. Precursors D and E are likely a mixture of scattered energy arriving sequentially from multiple scatterers. The PKIKP phase arrives after the dashed line.

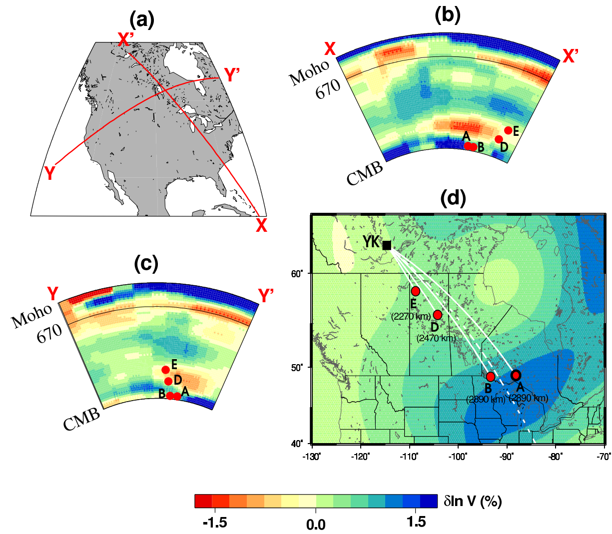

Figure 2.63: Distribution of seismic scatterers in the lower mantle. (a) Map view indicating the location of two vertical profiles in the region of our study. (b) and (c) Vertical cross-sections of the SAW24B16 shear wave tomographic model [*Megnin and Romanowicz*, 2000]. Profile XX' is along the great circle containing source and receivers, and profile YY' is perpendicular to it. Red dots show the projected locations of our constrained mantle scatterers into the cross-sections. (d) Map view of the distribution of seismic scatterers in the lower mantle. Black square denotes the Yellowknife seismic arry (YK). Red dots indicate our located scatterers. Solid white lines are the orizontal projections of the ray paths of precursors. The dashed white line is part of the great circle from the sources in South Sandwich Islands (SSI) to YK. The background tomographic model shows the distribution of shear-wave velocity at a depth of 2800km.

ing as the backbone facility for nuclear explosion monitoring. The epicentral distance from YK to the doublet (1993.12.01.00:59:01.2, $m_b = 5.5$, depth=33 km; 2003.09.06.15:46:59.9, $m_b = 5.6$, depth=33 km in the PDE catalog) at SSI is $\sim 137.8^o$. 18 of all 19 stations at YK recorded very high signal-to-noise PKP precursors for both events. In order to enhance the precursor signals, we filtered the original seismograms in the frequency range of 1 to 2 Hz. Before stacking, we aligned traces with respect to PKIKP phases by means of cross-correlation and performed array-sided travel time corrections to remove the influence of heterogeneities just beneath the seismic array. We applied two different stacking methods: linear stacking (Fig. 1a) and Phase-Weighted Stacking (PWS) (Fig. 1b).

Based on ray tracing and the single-scattering assumption, we are able to locate the scattering regions responsible for the individual PKP precursors, using our precise measurements of slownesses, back-azimuths, and differential arrival times. Comprehensive consideration of the high quality differential arrival times, slowness, and back-azimuth deviations enables us to locate the mantle scatterers for precursors A, B, D, and E (Fig. 2). Precursors A and B are scattered at the CMB, while precursors D and E are scattered at $\sim 420km$ and $\sim 620km$ above the CMB, respectively.

2.30.3 References

Cao, A., and B. Romanowicz, Locating scatterers in the mantle using array analysis of PKP precursors from an earthquake doublet. *Earth Planet. Sci. Lett.*, 255, 22-31, 2007.

Cleary, J.R., and R.A. Haddon, Seismic wave scattering near the core-mantle boundary: a new interpretation of precursors to PKP, *Nature*, 240, 549-551, 1972.

Doornbos, D.J., Multiple scattering by topographic relief with application to the core-mantle boundary, *Geophys. J. Int.*, 92, 465-478, 1988.

Gutenberg, B., and C.F. Richter, On seismic waves: I, *Gerlands Beitr. z. Geophysik.*, 43, 56-133, 1934.

Hedlin, M.A., P.M. Shearer, P.S. Earle, Seismic evidence for small-scale heterogeneity throughout the Earth's mantle, *Nature*, 387, 145-150, 1997.

Megnin, C., and B. Romanowicz, The three-dimensional shear velocity structure of the mantle from the inversion of body, surface and higher-mode waveforms, *Geophys. J. Int.*, 143, 709-728, 2000.

2.31. Test of Innermost Inner Core Anisotropic Models

Aimin Cao and Barbara Romanowicz

2.31.1 Introduction

Since the first evidence for inner core anisotropy was presented [*Morelli et al.*, 1986; *Woodhouse et al.*, 1986], increasingly complex models have been proposed. It has been documented that anisotropy increases with depth in the inner core, and that it is much weaker in the quasi-eastern than in the quasi-western hemisphere. At the top of the inner core ($< \sim 100km$), P-wave velocity may be isotropic and faster in the quasi-eastern hemisphere than in the quasi-western hemisphere.

The above complexity was questioned by several authors [*Bréger et al.*, 2000; *Romanowicz et al.*, 2002; *Ishii et al.*, 2002]. The complex lateral variations in P-wave velocity could be due to mantle, and possibly outer core, heterogeneity [*Bréger et al.*, 2000; *Romanowicz et al.*, 2002]. *Ishii et al.* (2002) suggested that there need not be an isotropic layer at the top of the inner core and that both body wave and normal mode observations can be explained by a model with constant anisotropy in the inner core.

More recently, the existence of an Innermost Inner Core (IMIC), within which the anisotropic characteristics are distinct, was proposed, respectively based on body wave [*Ishii and Dziewonski*, 2002] (hereafter referred to as ID02) and normal mode data [*Beghein and Trampert*, 2003] (hereafter referred to as BT03). However, the structures proposed are inconsistent: not only are the radii of the IMIC different ($\sim 300km$ [ID02] versus $\sim 400km$ [BT03]), but, more importantly, so are the slowest directions of anisotropy: in one model, the slowest direction is $\sim 45^o$ with respect to the earth's spinning axis (ID02); the other is along the spinning axis (BT03). *Cormier and Stroujkova* (2005) tested the IMIC model of ID02 using PKIKP waveform modeling and suggested a much larger radius ($\sim 500km$). Because the existence of the suggested IMIC is thought to be closely related to the early stages of inner core formation, it is important to try and clarify this inconsistency through further study.

The ID02 dataset is derived from the International Seismological Center (ISC) bulletins, and their study relies on the statistical analysis of a large noisy dataset. On the other hand, BT03 used normal mode data, the resolution of which decreases towards the center of the inner core. In this paper, we assemble a new dataset of absolute PKIKP (Fig. 2.64) travel time residuals, which are measured on high quality digital broadband seismograms recorded in global and local seismic networks (e.g., GSN, GEOSCOPE, and PASSCAL), to explore the seismic anisotropy in the central part of the inner core.

2.31.2 Data and Results

We systematically downloaded broadband vertical component seismograms ($M_w > 6.0$, depth>0 km) from the IRIS Data Management Center (DMC) corresponding to the epicentral distance range 150^o to 180^o, and for the time period 1990 to 2003, for which the relocated EHB event catalog is available [*Engdahl et al.*, 1998]. Thousands of seismograms recorded at global and regional networks were collected. Absolute PKIKP travel time residuals were measured with respect to the reference seismic model PREM, using relocated hypocenter and origin time as given in the EHB catalog, and correcting for ellipticity. We also conducted corrections for mantle heterogeneities using a P-wave global tomography model.

In order to test seismic models of ID02 and BT03, we calculate the predicted absolute PKIKP travel time residuals using the parameters of their respective anisotropic models [*Cao and Romanowicz*, 2007].

We divide our observations into four epicentral distance ranges (Fig. 2.65), corresponding to different depths of penetration of PKIKP in the inner core. In the epicentral distance range 173^o to 180^o, which corresponds to rays that sample the very center of the inner core, we confirm the trend observed by ID02, namely that the travel time residuals are maximum at intermediate angles ξ, decreasing both for polar ($\xi \sim 0$) and for equatorial ($\xi \sim 90^o$) paths. This means that the slowest P-wave velocity direction is not along the equatorial plane. This is why ID02 proposed the existence of an IMIC with a radius of $\sim 300km$ and a slowest direction oriented at $\sim 45^o$ with respect to the earth's rotation axis. However, our dataset indicates that the same trend is also present at shorter epicentral distances. More importantly, in the epicentral distance range 165^o to 180^o, neither the ID02 model nor the BT03 model can fit our observations. This fact suggests two possibilities: (1) there is an IMIC, but its anisotropic character is different from that in ID02 and BT03; (2) there is no IMIC.

First, we assume the existence of an IMIC. While keeping the upper layer anisotropic structure fixed, as given in ID02 (bulk constant anisotropy) and in BT03 (depth-dependent), respectively, we correct the observed PKIKP travel time residuals ($\delta t'$) (Fig. 2.65) by subtracting η_0 and δt_{upper} (contributed by the upper layer) and then invert for the anisotropic parameters A and B in the IMIC. It is clear that the constrained anisotropy in the IMIC strongly depends on the anisotropic structure in the upper layer of the inner core. If the upper layer has the bulk

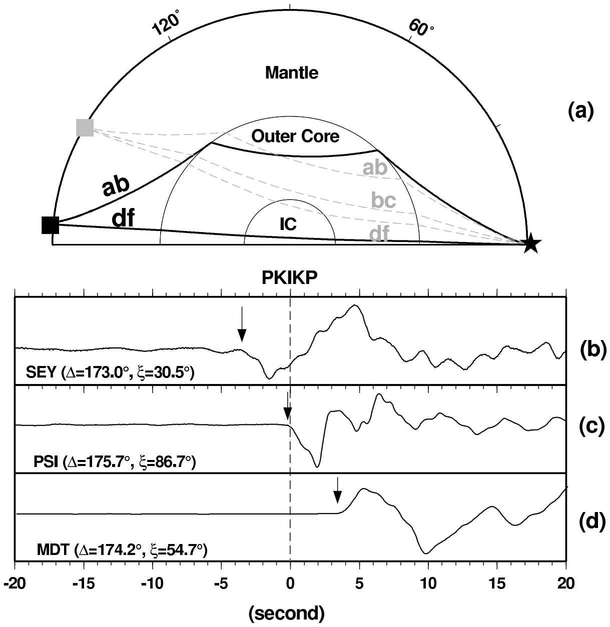

Figure 2.64: (a) Ray paths of PKIKP and PKP phases. The black solid line shows the ray path of PKIKP, which is used in this study. The event and stations are indicated by a star and squares, respectively. (b)-(d) Examples of PKIKP absolute travel time residual measurement.

constant anisotropic structure as used in ID02, the optimal IMIC radius inverted from our dataset is $\sim 480km$, and the corresponding variance reduction is 0.89. In contrast, the IMIC radius (300 km) suggested in ID02 is so small that the corresponding variance reduction is very low ($\sim$ 0.3). If the upper layer has the depth-dependent anisotropic structure as suggested in BT03, the optimal IMIC radius inverted from our dataset is $\sim 530km$, and the corresponding variance reduction is 0.94. Thus an IMIC with a depth-dependent anisotropic upper layer fits our dataset better. In both cases, the constrained IMIC radii are compatible with the radius suggested by *Cormier and Stroujkova* (2005) on the basis of PKIKP waveform modeling. In addition to the radius, the inverted IMIC anisotropic character is also strongly dependent on the upper layer anisotropy. The constrained slowest directions are $\sim 50^o$ and $\sim 55^o$, when considering a ID02 or BT03 upper layer, respectively. And the constrained P-wave velocities along the axis of the earth's rotation are 4.2% and 1.1% faster than that suggested in ID02, respectively.

Second, if there is no IMIC in the inner core, the variance reduction for a one-layer model is small (0.35). A constant anisotropy, one-layer, model can provide good fits to our observations in the epicentral distance range of 165^o to 170^o, but in other ranges, particularly from 173^o to 180^o, it does not (Fig.2.65). Both of the inverted "two-layer" IMIC models fit our observations very well in the epicentral distance ranges of 173^o to 180^o and 170^o to 173^o. In the other two epicentral distance ranges (150^o to 165^o and 165^o to 170^o), however, the model with an upper layer as in BT03-1 fits our dataset better (Fig. 2). This suggests that the anisotropic structure in the upper part of the inner core most likely changes with depth.

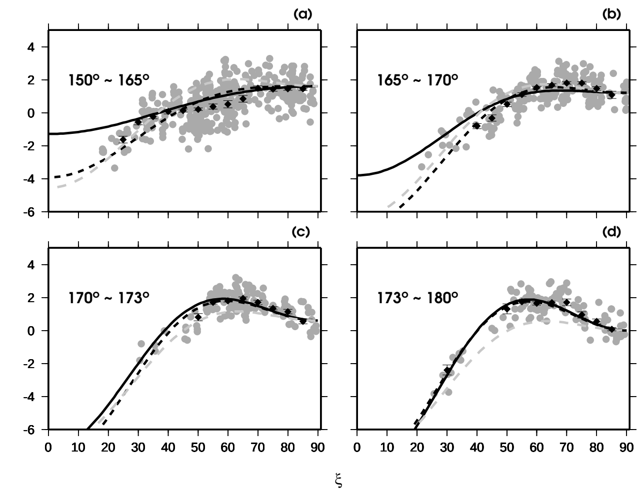

Figure 2.65: Theoretical PKIKP travel time residuals as a function of ξ, which include δt_{IMIC} (contributed by our inverted IMIC), δt_{upper} (contributed by the upper layer), and η_0. The solid and dashed black lines correspond to the best fitting IMIC models with a bulk constant (ID02-1) and a depth-dependent (BT03-1) anisotropic upper layer, respectively. The dashed grey line corresponds to a one-layer (i.e., no IMIC) anisotropic inner core model. The grey dots are data.

2.31.3 References

Beghein, C., and J. Trampert, Robust normal mode constraints on inner core anisotropy from model space search, *Science*, 299, 552-555, 2003.

Cao, A., and B. Romanowicz, Test of the innermost inner core models using broadband PKIKP travel time residuals. *Geophys. Res. Lett*, 34, L08303, 2007.

Ishii, M., and A.M. Dziewonski, The innermost inner core of the earth: evidence for a change in anisotropic behavior at the radius of about 300km, *Proc. Natl. Acad. Sci. U.S.A.*, 22, 14026-14030, 2002.

Romanowicz, B., H. Tkalcic, and L. Bréger, On the origin of complexity in PKP travel time data from broadband records, in Earth's Core: Dynamics, Structure, Rotation, V. Dehant and K. Creager Eds, *AGU Geodynamics Series*, 31, 31-44, 2002.

2.32. GPS exploration of the elastic properties across and within the Northern San Andreas Fault zone and heterogeneous elastic dislocation models

Romain Jolivet (Ecole Normale Superieure de Paris), Roland Bürgmann and Nicolas Houlie

2.32.1 Introduction

The Northern San Francisco Bay Area (hereafter "North Bay") is sliced by three major right-lateral strike-slip faults, the northern San Andreas Fault (SAF), the Rodgers Creek Fault (RCF) and the Green Valley Fault (GVF). The RCF represents the North Bay continuation of the Hayward fault zone and the GVF is the northern extension of the Concord fault. North of the juncture with the San Gregorio fault, geodetic and geologic data suggest a SAF slip rate of 20-25 $mm.yr^{-1}$ (*d'Alessio et al*, 2007, *Lisowski et al.*, 1991). Geodetically determined slip rates range from 20.2 ± 1.4 $mm.yr^{-1}$ (*d'Alessio et al.*, 2007) to 23 ± 3 $mm.yr^{-1}$ (*Freymueller et al.*, 1999). The remainder of the 40 $mm.yr^{-1}$ of Pacific plate to Sierra Nevada Great Valley microplate motion is primarily accomodated by the RCF and the GVF.

Earthquake cycle deformation is commonly modeled assuming lateraly homogeneous elastic properties in the Earth's crust. First-order variations in rock elastic strength both across and within fault zones can, however, strongly impact inferences of fault slip parameters and earthquake rupture characteristics. Near Point Reyes, the SAF separates two different geologic terranes. On the east side of the fault is the Franciscan Complex, made of a mixture of Mesozoic oceanic crustal rocks and sediments, which were accreted onto the North American continent during subduction of the Farallon plate. On the west side of the SAF is the Salinian terrane, which is composed of Cretaceous granitic and metamorphic rocks, overlain by Tertiary sedimentary rocks and Quaternary fluvial terrasses. *Prescott and Yu*, 1986, *Lisowski et al*, 1991 describe an asymmetric pattern along a geodetically measured surface velocity profile across to SAF at Point Reyes, which can be explained by higher rigidities to the SW of the fault. *Le Pichon et al.*, 2005, describes also an asymmetric pattern further north along the SAF, at Point Arena, but not at Point Reyes. *Chen & Freymueller*, 2002, rely on near-fault strain rates determined from trilateration and GPS measurements to infer a 2-*km*-wide near-fault compliant zone (with 50% reduced rigidity) near Bodega Bay and Tomales Bay. Here we use densily spaced GPS velocities across the SAF to evaluate changes in elastic properties and within the SAF zone.

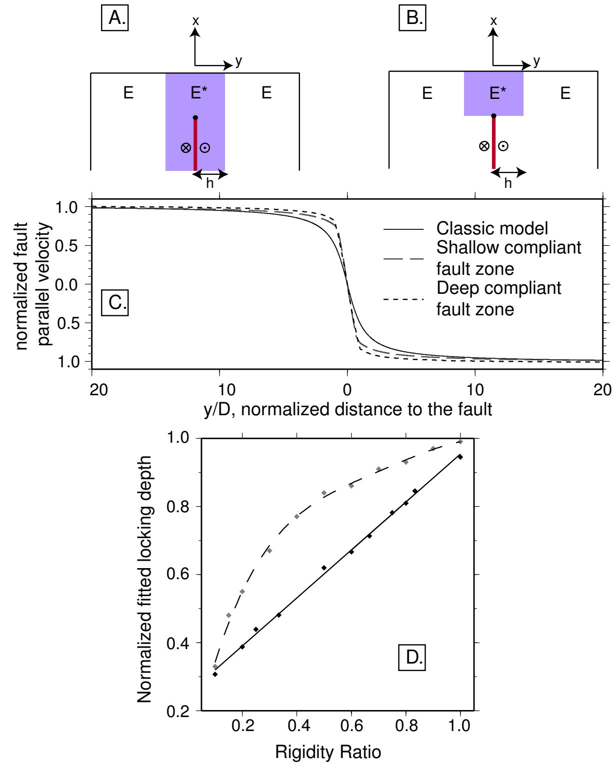

Figure 2.66: Model geometry of A. deep and B. shallow CFZM. The shaded area is the weak fault zone. C. Comparison between a 10 km locking depth classic screw dislocation model (continuous line), a 10 km locking depth Shallow CFZM (long-dashed grey line) and a 10 km locking depth Deep CZFM (dashed black line) with rigidity in the 2-km-wide fault zone being reduced by 80%. D. Locking depth determined by fitting velocity profiles (400 km long with a point spacing of 0.5 km) calculated with the CFZMs with the half-space equation 2.6. The grey dots are the best-fit locking depth for the deep CFZM and the dashed line is the corresponding polynomial fit. The black dots are the fitted locking depth for the shallow CFZM and the continuous line is the corresponding linear fit.

2.32.2 Heterogeneous Elastic Models

The classic way to interpret a GPS-derived velocity profile across a strike-slip fault is, assuming that the movement is only horizontal, to use the screw dislocation model (*Savage and Burford*, 1973):

$$v(y) = \frac{v_{max}}{\pi} atan(\frac{y}{D}) \quad (2.6)$$

Where v is the predicted fault-parallel velocity of a surface point at distance y from the fault and v_{max} is the far field velocity. v_{max} is also the slip rate on the dislocation below the locking depth D. This model assumes an infinite dislocation burried in a semi-infinite elastic medium. Next we consider laterally heterogeneous models that account for variation of elastic properties across and within the fault zone.

We first consider the model developed by *Le Pichon et al.*, 2005, where the fault separates two elastic media, with different Young's modulus E_1 and E_2. They consequently use a rigidity ratio, K, in the following equations:

$$y < 0 \quad \Rightarrow \quad V(y) = KV_{max} + (\frac{2KV_{max}}{\pi}) atan(\frac{y}{D}) \quad (2.7)$$
$$y > 0 \quad \Rightarrow \quad V(y) = KV_{max} + (\frac{2(1-K)V_{max}}{\pi}) atan(\frac{y}{D})$$

Where $V(y)$ is again the velocity at a distance y from the fault, V_{max} is the far field velocity, D the locking depth, and $K = \frac{E_2}{E_1+E_2}$ is the asymmetry ratio.

We also evaluate the deep Compliant Fault Zone Model (CFZM) developed in *Chen & Freymueller*, 2002, following *Rybicki and Kasahara*, 1977. A low rigidity fault zone is introduced between two elastic blocks (Figure 2.66).

This model (A. in Figure 2.66) is based on an infinitely deep weak fault zone. If we consider that the fault zone is weak because of damage caused by repeated earthquakes, this zone should not extend deeper than the locking depth. Therefore, we developed, using Finite Element Modeling (*Chéry et al.*, 2001), a shallow CFZM (B. in Figure 2.66). Both models tend to localize the deformation close to the fault trace, but the shear is more localized in the shallow CFZM.

We tried to fit the computed velocity profiles obtained with both CFZMs with the classic screw dislocation model, to evaluate the trade-off between the rigidity ratio and the obtained best-fit locking depth. For both models, there is an inverse relationship between the rigidity ratio and the fitted locking depth (linear for the deep CZFM and curved for the shallow CZFM). As the difference between the CFZMs and the fitted classic models is smaller than the typical error obtained with geodetic data (typically 1 $mm.yr^{-1}$), we cannot distinguish between a shallow locking depth and a compliant fault zone, relying only on geodetic data. Thus it is important to have independent constraints on the locking depth, for instance from the depth extent of microseismicity.

2.32.3 GPS velocities along the Northern San Andreas Fault

We collected GPS data in Bodega Bay and Tomales Bay, using 1996-2000 GPS measurements from *Chen & Freymueller* (2002) to calculate the velocities. We also used data from the Point Reyes profile, provided by the Bay Area Velocity Unification (BAVU), a compilation of the San Francisco bay area GPS velocities (*d'Alessio et al.*, 2005). The data are processed using the GAMIT/GLOBK GPS analysis software. The site velocities are shown with respect to BARD continuous GPS station LUTZ in Figure 2.

A first analysis with a simple screw dislocation model, based on three parallel faults (SAF, RCF and GVF) provides a 23 ± 1 $mm.yr^{-1}$ slip rate on the SAF, with a 14 ± 2 km locking depth, while the whole system is accomodating 40 $mm.yr^{-1}$ of fault parallel displacement (we find a 8 ± 1 $mm.yr^{-1}$ slip rate on the RCF and 9 ± 1 $mm.yr^{-1}$ on the GVF)(Figure 2.67). *d'Alessio et al.* (2007) show that the velocity of the Farallon islands with respect to the Pacific plate is about 2.9 $mm.yr^{-1}$ consistent with our modelled velocity field. But the half-space model velocity for the Farallon Island station is 4 to 5 $mm.yr^{-1}$ faster than the actual measured velocity. We next consider asymmetric models with a rigidity contrast across the SAF, fitting the data with the equation 2.8. We find that the modeled velocity profile better matches the Farallon Islands velocity with a 0.41 K ratio. Thus, we infer that the Salinian terrane has a rigidity 1.4 times higher than the Franciscan complex to the east of the SAF. Our results suggest an 18 $mm.yr^{-1}$ slip rate on the SAF, with a 10 km locking depth. There is a significant trade-off between the inferred slip rate on the SAF and the rigidity contrast across the fault, with smaller rigidity contrasts leading to higher inferred slip rates.

The two networks across the SAF located further north, one in Tomales Bay and one in Bodega Bay, allow us to consider if the SAF represents a low-rigidity fault zone. Our preferred model for the Tomales Bay profile is a classic dislocation, with a 21 $mm.yr^{-1}$ slip rate on the SAF, with a 12 km locking depth. We did not explore the corresponding trade-off but as our data set doesn't extend far away on both side of the fault, even using the PS-SAR data from *Funning et al.*, 2007, the determined parameters are not well constrained. In Bodega Bay, our preferred model is based on a deep CFZM, with a 28 $mm.yr^{-1}$ slip rate on the SAF, with a 15 km locking depth. The compliant zone is 40% weaker than the surrounding medium. But a classic homogeneous model with a 24 $mm.yr^{-1}$ slip rate and a 7 km locking depth on the SAF satisfies the near-field data as well, as shown by the first-order trade-off between locking depth and the compliant fault zone rigidity contrast we found in the previous section. We prefer a 15 km locking depth and consequently introducing this deep CFZM because of the microseismicity near the Point Reyes profile, assuming that there is no significant changes in the locking depth.

2.32.4 Acknowledgements

This project was funded by the USGS National Earthquake Hazard Reduction Programm (NEHRP). We would like to thank J. Freymueller for his help during the GPS survey.Thanks to R. Bürgmann for having me in his team during 6 months and to all the Berkeley Active Tectonics Group.

2.32.5 References

d'Alessio, M. A., Johanson, I. A., Bürgmann, R., Schmidt, D. A. and Murray, M. H., Slicing up the San Francisco Bay Area: Block kinematics and fault slip rates from GPS-derived surface velocities, *J. Geophys. Res.*, *110*, B0640, 2007.

Chen, Q. and Freymueller, J. T., Geodetic evidence for a near-fault compiant zone along the San Andreas Fault in the San Francisco Bay Area, *J. Geophys. Res.*, *92*, 2002.

Chéry, J., Zoback, M. and Hassani, R., Rheology, strain and stress of the San Andreas Dault in Central and Northern California: A 3-d thermomechanical modeling study, *J. Geophys. Res.*, *106*, , B08406, 2001.

Freymueller, J. T., Murray, M. H., Segall, P. and Castillo, D., Kinematics of the Pacific-North America plate boundary zone, northern california, *J. Geophys. Res.*, *104*, 7419-7442, 1999.

Funning, G. J., Bürgmann, R., Ferretti, A. and Fumagalli, A. Creep on the rodgers creek fault, northern san francisco bay area from 10 year ps-insar dataset. *submitted*, 2007.

Le Pichon, X., Kreemer, C. and Chamot-Rooke, N., Asymmetry in elastic properties and the evolution of large continental strike-slip faults, *J. Geophys. Res.*, *110*, B03405, 2005.

Lisowski, M., Savage, J. C. and Prescott, W. H., The Velocity Field Along the San Andreas Fault in Central and Southern California, *J. Geophys. Res.*, *96*, 8369-8389, 1991.

Prescott, W. H. and Yu, S. B., Geodetic measurement of horizontal deformation in the northern San Francisco Bay region, California, *J. Geophys. Res.*, *91*, 7475-7484, 1986

Savage, J. and Burford, R., Geodetic determination of relative plate motion in central California, *J. Geophys. Res.*, 1973

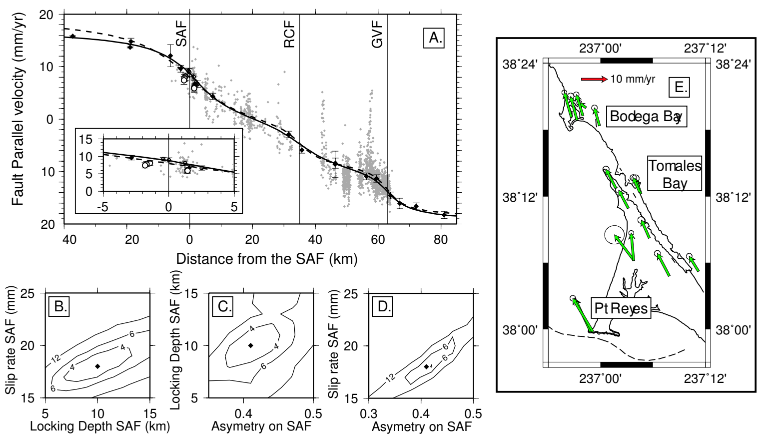

Figure 2.67: A. Best fit dislocation models for the Point Reyes profile. The black dots are the fault-parallel projected GPS velocities with their associated error bars. The grey dots are the PS-SAR data from (*Funning et al.*, 2007). The dashed line is the best classic (elastic half-space) dislocation model. The continuous line is our preferred asymmetric model with a K ratio of 0.41 that better matches the observed velocity of the westernmost GPS site on the Farallon Islands. B. Trade off between the Locking Depth and the Slip Rate on the SAF. Contoured values are the sum of the weighted squared residuals divided by the number of data points C. Trade off between the Asymmetry Ratio and the Locking Depth on the SAF. D. Trade off between the Asymmetry Ratio and the Slip Rate on the SAF.